SEARCH FOR FLAVOR CHANGING NEUTRAL CURRENTS IN TOP QUARK DECAYS USING A TWO-LEPTONS+TRACK SELECTION

BY

ARELY CORTES GONZALEZ

DISSERTATION

Submitted in partial fulfillment of the requirements
for the degree of Doctor of Philosophy in Physics
in the Graduate College of the
University of Illinois at Urbana-Champaign, 2012

Urbana, Illinois

Doctoral Committee:

Professor Kevin Pitts, Chair
Professor Tony Liss, Director of Research
Professor James Eckstein
Professor Scott Willenbrock

Abstract

A search for flavor-changing neutral currents in top quark decays is described. Data collected at a center-of-mass energy of $\sqrt{s} = 7$ TeV during 2011 corresponding to an integrated luminosity of 2.1 fb^{-1} are used. A cut-based analysis is used on top quark pair production events, where one top quark is assumed to follow the dominant Standard Model decay $t \to Wb$, and the other the flavor changing neutral current decay $t \to Zq$. Only the decays of the Z-boson to charged leptons and leptonic W-boson decays are considered signal. The search uses an event selection with two identified leptons (electrons and/or muons) and one lepton selected via inner-detector track requirements only (track lepton). Backgrounds to the search are evaluated using almost entirely data-driven techniques. An orthogonal channel, with three identified leptons is also described, and used in the final result. No significant excess is observed in the signal region. An upper limit on the $t \to qZ$ branching ratio of BR($t \to Zq$) <0.73% is set at the 95% confidence level, compatible with the expected limit.

To my parents and siblings,

to whom my own being is indebted.

Acknowledgments

I first want to thank my advisor, Tony Liss, because he had the strangest work of putting up with my random enthusiasm and desperation. He was by far the best support I could have had. He trusted me and my work, even when I failed to do so myself. Most importantly, I appreciate him keeping things in perspective. Emphasis on 'a work well done' over 'getting done with it' is an important lesson in this particular field of physics. I can only hope one day to have it all figured out as he seems to do. I believe I must thank him for one more thing: giving me the chance to brag about my advisor with fellow grad students at CERN. Mine was, hands down, the nicest one around.

A good deal of gratefulness to the '3ID' group: Antonio, Filipe, Joao and Nuno. They were supportive of our work when times needed it. It was more than a pleasure to collaborate with them. Filipe more than anyone, promptly answering questions that made my work progress a bit faster. Thanks go to our group conveners and editorial board too, for their support, specially in the last stages of the analysis. I want to thank Prof. Mark Neubauer. It was an absolute delight to work with him during my first year in ATLAS. He is a very enthusiastic physicist that makes you want to be as excited about the work as he seems to be. I can be nothing less than thankful to Nektarios. He was not only helpful in my introduction to ATLAS, but also very kind to me along the years. Those first months at CERN passed so rapidly, and I learned so much, and I know it was in great part because he kept pushing me. Thanks to the rest of the UIUC group; James and Austin in particular for their contribution to our work. I truly missed James when he moved back to Urbana, he was a great officemate, always willing to help me out. Special mention to Hovhannes, for the fun memories of the "cross section summer", and the many hours he put up with my idealism and crazy fear of darkness (and for those days when we could have given up physics, yet we did not). Appreciation also goes to some of the people in the Muon group, specially Niels, Ahmimed and Jean-François, who, very likely without knowing it, helped me build not only knowledge but also confidence by always answering my naïve questions with kindness.

To my family goes the best. As said many times before, I owe them everything I am (except for the boring stuff, I managed to accomplish that all by myself). Thank you, because I was never a visitor at home, and for the many times when, intoxicated with insomnia, I would call home, if only to sing to them. El otro día me acordé de cuando vivíamos en Villas, de esa primera Navidad que celebramos solo nosotros, y sigo sin entender porque nunca aprendí a andar en bicicleta. Misterios.

Thanks to my friends at CERN: Nir, Herta, Kathy, Gry and Angela, who provided cake, laughs, and strength (perhaps unknowingly). To the Mexican kids at CERN too. They were a nice component of these European years. To Ly, Lyuda and Tomoki: thanks for the Mika-style (¿por qué no?) fun back in UC. To my friends from Monterrey: Di, Eme, Ichan, Juancho, Tita, Viri, all the not-given hugs. Even without being here, after the many years as undergrads, they were a happy place in my mind where I would hide whenever things were too stressful or disappointing (on pourrait presque...).

Last, but definitely not least: thank you, Kirill. The last year I have been an emotional 'bleh' (a bit), and despite my childish ways you stayed along. I surely like you more than a rabbit.

After all the *disasterology* I got myself into these years, things keep moving on[1]. And that is good. During the last weeks of thesis-writing I have been missing doing physics so much, I can not wait to start again! There can be no better way to let yourself know that you love what you have chosen to do.

(Walks away humming)

[1] [Nils] Runeberg published, in the symbolist sheet Sju insegel, an assiduously descriptive poem, "The Secret Water": the first stanzas narrate the events of one tumultuous day; the last, the finding of a glacial pool; the poet suggests that the eternalness of this silent water checks our useless violence, and in some way allows and absolves it. The poem concludes in this way: *The water of the forest is still and felicitous, And we, we can be vicious and full of pain.* // [Nils] Runeberg publicó, en la hoja simbólica Sju insegel, un asiduo poema descriptivo, El agua secreta; las primeras estrofas narran los hechos de un tumultuoso día; las últimas, el hallazgo de un estanque glacial; el poeta sugiere que la perduración de esa agua silenciosa corrige nuestra inútil violencia y de algún modo la permite y la absuelve. El poema concluye así: *El agua de la selva es feliz; podemos ser malvados y dolorosos* [1].

Table of Contents

List of Tables

List of Figures

Chapter 1

Introduction

The top quark is the heaviest elementary particle known, and it has a small lifetime which does not allow bound-states of the top quark to be formed. Because of its large mass, $m_t = 173.2 \pm 0.9$ GeV [2], the top quark has a strong coupling to the electroweak symmetry breaking sector, becoming an interesting channel to test the Standard Model (SM) of particle physics, providing potentially a window onto physics beyond the SM. If deviations from the SM predictions of the production and decay properties of the top quark are found, they will provide model-independent evidence for physics beyond the Standard Model. According to the SM, the top quark decays almost exclusively through the mode $t \to Wb$. Flavor changing neutral currents (FCNC) are highly suppressed in the SM by the GIM mechanism which yields a branching ratio of the order of 10^{-14}. Several SM extensions predict a higher branching ratio for top quark FCNC decays. In these models, the branching ratio is typically many orders of magnitude larger than the SM branching ratio, and can be as high as $\sim 1 \times 10^{-4}$ in certain quark-singlet models [3]. Previous measurements done at the Tevatron [4] put an experimental limit on the branching ratio of this FCNC top quark decay to be less than 3.2%.

For this thesis, I performed a search for FCNC in 2.1 fb^{-1} of 2011 pp collision data collected by ATLAS. The search is done in $t\bar{t}$ events, where one of the top quarks is assumed to follow the dominant SM decay $t \to Wb$ and the other the FCNC decay $t \to Zq$. Since only leptonic decays of the W-boson and decays of the Z-boson into a pair of charged leptons are used as signal, the final state topology includes three isolated charged leptons, at least two jets, one of them coming from a b-quark, and missing transverse momentum from the undetected neutrino. Events with two identified leptons (electrons and/or muons) and one high-quality inner detector track (track-lepton) are searched for. These events are denoted "2ID+TL events". The track-lepton selection was first introduced in a $t\bar{t}$ cross section measurement done at the Tevatron by the CDF experiment [5]. In ATLAS, it has been used for the $t\bar{t}$ cross section measurement as well, with both 2010 and 2011 data [6, 7]. A FCNC search in an orthogonal channel, where three identified leptons are looked for, is also performed by other members of the collaboration. This selection is denoted "3ID". I will be briefly introduce it here, since the final result to be presented combines them both.

This thesis is organized as follows. In Chapter 2 I present a theoretical background for the topic at hand. This includes not only a brief introduction to the Standard Model, but also a summary of beyond the SM theories that could be of interest in the analysis to be presented. Chapter 3 has a description of the ATLAS detector and its different components, that will be of use when introducing object selection later on. A description of the luminosity measurement is also included in this Chapter. Monte Carlo simulations are introduced in Chapter 4, along with a list of samples used in the analysis and corrections specific to Monte Carlo based estimations. The full object and event selection is described in Chapter 5. In this Chapter I will make a distinction between the 2ID+TL and the 3ID channels. The former will be explained in more detail. Similarly, in Chapter 6 the SM backgrounds for the 2ID+TL channel will be explained fully, and summarized for the 3ID channel. In Chapter 7 I explain the different sources of systematic uncertainties, and how they are evaluated. Chapter 8 presents the details on the limit evaluation. Finally, conclusions are presented in Chapter 9. Further information is presented in the Appendices, which will be introduced when relevant.

The results of this analysis, combining the 2ID+TL and 3ID channels, have been submitted for publication to JHEP [8].

Chapter 2

Top Quark Physics

2.1 Introduction

In 1994 first hints of the top quark were reported by the CDF experiment [9]. Later in 1995 its existence was corroborated by both CDF and D0 experiments [10, 11] at the Tevatron. Its discovery completed the three generation structure of the SM and signaled the start of the new field of top quark physics. Some of its properties, like its rather large mass, make it a very interesting object of study, not only for the understanding of the SM, but also in the search of physics beyond the SM (BSM). This chapter briefly covers the theoretical background relevant for this analysis. In particular, Section 2.3 covers aspects of the top quark, like production and decay, that will be referred to in the following. Section 2.4 reviews FCNCs, not only within the SM, but also in some extensions of the SM.

2.2 The Standard Model

The introduction of the SM [12–15] made one of the recurrent dreams of elementary particle physics possible: a fundamental synthesis between electromagnetism and weak interactions [1]. Strong interactions were later described by introducing quantum chromodynamics, and the existence of quarks confirmed in 1974 with the discovery of J/ψ. The following summary is taken from References [16–20].

At present, the SM of particles and their interactions account for practically all the experimental data from high energy physics experiments. Within this model, all particles are built from a number of fundamental, spin $\frac{1}{2}$, particles called fermions (quarks and leptons), summarized in Table 2.1. For each of these fermions, there exists an antiparticle with the same mass but opposite charge. Neutrinos ν have been recently observed to have non-zero mass, unlike previously assumed. Furthermore, because they are neutral,

[1] Quoting A. Salam from Reference [13].

the question whether each neutrino is its own antiparticle (Majorana particles) or not (Dirac particles) remains unanswered. The SM also comprises the interactions among those particles, which are described in terms of particles of spin 1, bosons, which work as mediators of forces between the fermion constituents. The different interaction mediators are summarized in Table 2.2. Strong interactions are responsible for binding the quarks. This interquark force is mediated by a massless particle, the gluon g, which itself carries the corresponding charge, "color". Also massless, photons γ, mediate the electromagnetic interaction between charged particles. The quanta of weak interaction fields are the charged W-boson and the neutral Z-boson. These last two carry mass, making the weak interaction short-ranged. On the contrary, electromagnetic interaction has infinite range because of the massless mediator. Gluon fields despite being massless are confining, so the strong force is not observed as a long range force. This confinement of quarks means quarks can not exist as free particles. The quarks appear in three families or generations: (u, d), (c, s) and (t, b). Quarks carry color, and they have fractional electrical charge. The leptons also appear in three generations: (e, ν_e), (μ, ν_μ) and (τ, ν_τ). Unlike quarks, they are colorless. Charged leptons are paired with neutral leptons (neutrinos). Because neutrinos are neutral, they only interact weakly. Additionally there exist gravitational interactions which act between all types of particles. However, gravitational forces are, in the scale of particle physics, insignificant (unless there is a TeV scale gravity). In fact, the SM does not take into consideration the gravitational fields, which makes it not a theory of everything.

particle	flavor			$Q/\|e\|$
	generation			
	1^{st}	2^{nd}	3^{rd}	
leptons	e	μ	τ	-1
	ν_e	ν_μ	ν_τ	0
quarks	u	c	t	$+\frac{2}{3}$
	d	s	b	$-\frac{1}{3}$

Table 2.1: The fundamental fermions.

interaction	mediator	spin/parity	coupling strenght $[\alpha]$
strong	gluon, g	1^-	~ 1
electromagnetic	photon, γ	1^-	$\sim 10^{-1}$
weak	$W^\pm$, Z	1^-, 1^+	$\sim 10^{-7}$

Table 2.2: The boson mediators. Note that, the neutral Z-boson is sometimes expressed as Z^0 in different texts.

2.2.1 Quantum Electrodynamics

Quantum electrodynamics (QED) refers to the electromagnetic interactions of leptons and photons. It is characterized by renormalization and gauge invariance. The U(1) gauge invariance is in fact what brings the Lagrangian for a free field to the Lagrangian of QED. The Dirac equation:

$$\mathcal{L} = i\bar{\psi}\gamma^{\mu}\partial_{\mu}\psi - m\bar{\psi}\psi, \tag{2.1}$$

where ψ is the lepton vector field, is not invariant under a local gauge transformation such as:

$$\psi(x) \rightarrow e^{i\alpha(x)}\psi(x), \tag{2.2}$$

where $\alpha(x)$ depends on space and time in an arbitrary way. Because of Noether's Theorem, invariance under a transformation is relevant because it translates into a conservation law. The second term in Equation 2.1 is invariant under the transformation given in Equation 2.2, but the $\partial_{\mu}\psi$ terms breaks the invariance. In order to impose such invariance, an alternative derivative is introduced, D_{μ}, which transforms covariantly under phase transformations, like ψ itself:

$$D_{\mu}\psi \rightarrow e^{i\alpha(x)}D_{\mu}\psi. \tag{2.3}$$

To form this covariant derivative, a vector field A_{μ} must be introduce.

$$D_{\mu} \equiv \partial_{\mu} - ieA_{\mu}, \tag{2.4}$$

where A_{μ} transforms as:

$$A_{\mu} \rightarrow A_{\mu} + \frac{1}{2}\partial_{\mu}\alpha \tag{2.5}$$

By construction, the unwanted term in the transformation of Equation 2.1 is canceled. Thus, the Lagrangian is now:

$$\mathcal{L} = \bar{\psi}\left(i\gamma^{\mu}\partial_{\mu} - m\right)\psi + e\bar{\psi}\gamma^{\mu}\psi A_{\mu} \tag{2.6}$$

By enforcing local gauge invariance, a vector field A_{μ}, a gauge field, is introduced. This gauge field couples to the Dirac particle (with charge $-e$) in the same way as a photon field. If this is indeed the new physical photon field, a term corresponding to its kinetic energy should be added to the Lagrangian. This kinetic term must also be invariant under the transformation given in Equation 2.5, and thus can only involve the

gauge invariant field strength tensor:

$$F_{\mu\nu} = \partial_\mu A_\nu - \partial_\nu A_\mu. \tag{2.7}$$

The final QED Lagrangian is:

$$\mathcal{L}_{\text{QED}} = \bar{\psi}\left(i\gamma^\mu\partial_\mu - m\right)\psi + e\bar{\psi}\gamma^\mu A_\mu\psi - \frac{1}{4}F_{\mu\nu}F^{\mu\nu}. \tag{2.8}$$

From there, it is clear that the addition of a mass term, $\frac{1}{2}m^2 A_\mu A^\mu$ is prohibited by gauge invariance. Thus, the gauge particle for this field, the photon, must be massless.

An important feature derived from renormalization is the fact that coupling 'constants' are not constants but rather depend logarithmically on the energy scale, q^2, of the measurements. This "running" coupling constant, $\alpha(q^2) = e^2(q^2)/4\pi$, is:

$$\alpha(q^2) = \frac{\alpha(\mu^2)}{1 - \frac{\alpha(\mu^2)}{3\pi}\log\left(\frac{q^2}{\mu^2}\right)} \tag{2.9}$$

where μ is the reference or renormalization momentum. $\alpha(q^2)$ describes how the effective charge depends on the separation of the two charged particles, this is a sort of "charge screening". As q^2 increases, the photon sees more charge until $\alpha(q^2)$ becomes infinity, at a very large q^2.

2.2.2 Quantum Chromodynamics

Quantum Chronodynamics (QCD) is the gauge field theory that describes the strong interactions of colored quarks and gluons. It is the SU(3) component of the SU(3)×SU(2)×U(1) SM. In a similar way to the $\mathcal{L}_{\text{QED}}$ derivation, the QCD Lagrangian is inferred from local gauge invariance. In this case the U(1) gauge group is replaced by the SU(3) group of phase transformations on the quark color fields. From there, strong interactions of quark fields ψ_q and gluon fields $\mathcal{A}_\mu$ are described in the SM Lagrangian by the following:

$$\mathcal{L}_{\text{QCD}} = \sum_q \bar{\psi}_{q,a}\left(i\gamma^\mu\partial_\mu\delta_{ab} - g_s\gamma^\mu t^C_{ab}\mathcal{A}^C_\mu - m_q\delta_{ab}\right)\psi_{q,b} - \frac{1}{4}F^A_{\mu\nu}F^{A\mu\nu}, \tag{2.10}$$

where repeated indices are summed over. The γ^μ are the Dirac γ-matrices. $\psi_{q,a}$, are the quark-field spinors for a quark flavor q and mass m_q carry a color index a that runs from $a = 1$ to $N_c = 3$. That is, quarks come in three colors. Quarks are the fundamental representation of the SU(3) group. The index C of the gluon field $\mathcal{A}^C_\mu$ runs from $C = 1$ to $N_c^2 - 1 = 8$, which means that there are eight kinds of gluons. The t^C_{ab}

matrices are the three-dimensional representation of the group generators of SU(3). They encode the fact that a gluon's interaction with a quark rotates the quark's color in SU(3) space. Just as for the photon in QED, local gauge invariance requires the gluons to be massless. The constant g_s is the coupling parameter. The fundamental parameters of QCD are this coupling and the quark masses.

The gauge field strength of the gluon field $\mathcal{A}$ is given by:

$$F^A_{\mu\nu} = \partial_\mu \mathcal{A}^A_\nu - \partial_\nu \mathcal{A}^A_\mu - g_s f_{ABC} \mathcal{A}^{\mathrm{B}}_\mu \mathcal{A}^C_\nu , \tag{2.11}$$

where f_{ABC} are the structure constants of the SU(3) group and satisfy $[t^A, t^B] = i f_{ABC} t^C$.

Since the quark and gluon interactions are proportional to g_s, the strong coupling constant is defined as: $\alpha_s = g_s^2/4\pi$. The behavior of α_s makes QCD a very interesting theory. When virtual corrections due to the gluon field are taken into account, the strong coupling changes with momentum transfer q^2 like:

$$\alpha_s(q^2) = \frac{12\pi}{(33 - 2n_f)\log(q^2/\Lambda^2_{\mathrm{QCD}})} \tag{2.12}$$

where Λ_{QCD} is the QCD energy scale, n_f is the number of quark flavors with mass lower than $\sqrt{q^2}$. So, the value of α_s decreases with increasing q^2. This is the effect known as asymptotic freedom. The opposite behavior is seen with decreasing q^2: the coupling strength increases. This has the consequence that no free colored objects are observed in nature, and quarks are gluons are bound by the principle of color confinement.

The transition from colored quarks and gluons to colorless hadronic particles in the final state of physics reactions is difficult to describe from first principles. In theoretical calculations Monte Carlo models are an effective approach to cover the fragmentation and hadronization phase of physics processes. This will be briefly explained in Chapter 4

2.2.3 Weak and Electroweak Interactions

Weak interactions take place between all quark and lepton constituents, each of them having a "weak charge" assigned. Usually, the weak interaction is completely swamped by the much greater strong and electromagnetic interactions, unless these are forbidden by some conservation rule. Consequently, observable weak interactions might involve neutrinos (no charge, no color) or quarks with a flavor change that is forbidden

for strong interactions. Although $W^{\pm}$ does not change lepton-flavor (it only couples leptons within the same generation), it can change quark flavor (couples same and different generation quarks). Different flavors of leptons have identical couplings to the weak bosons. However, quark couplings to weak bosons do depend on the quark flavor. The weak interactions are called so, because they are mediated by the massive charged and neutral vector bosons, $W^{\pm}$, Z, which are very massive and hence give rise to interactions of very short range. These interactions are called charged-current and neutral-current interactions, respectively.

The discovery of parity violation, observed in β-decays, implied a combination of two types of interaction with opposite parities. According to their transformation properties under spatial reflection, up to five types of operators are allowed, these are: vector (V), axial vector (A), scalar (S), pseudoscalar (P) and tensor (T). The vector field ψ can be decomposed into a left-handed and a right-handed field, $\psi_L = \frac{1}{2}(1-\gamma_5)\psi$ and $\psi_R = \frac{1}{2}(1+\gamma_5)\psi$, respectively. This $(1-\gamma_5)$ is the $V-A$ (vector - axial vector) form of the weak current. This $V-A$ structure means that the weak current differentiates itself from the electromagnetic and strong interactions by only coupling left-handed fermions. Weak interactions are based on the gauge group $\mathrm{SU}(2)_L$. The left handed fermion fields on the i^{th} fermion family transform as doublets:

$$\psi_i \quad = \quad \begin{pmatrix} \nu_i \\ \ell_i^- \end{pmatrix} \quad \text{and} \quad \begin{pmatrix} u_i \\ d_i' \end{pmatrix}, \tag{2.13}$$

where $d_i' \equiv \sum_j V_{ij} d_j$ and V is the Cabibbo-Kobayashi-Maskawa (CKM) mixing matrix (see below).

Spontaneous Symmetry Breaking

The process by which the weak bosons acquire mass, unlike their electromagnetic and strong massless counterparts, is by the mechanism of spontaneous symmetry breaking. This is based on the Goldstone theorem which states that massless scalars occur whenever a continuos symmetry of a physical system is "spontaneously" broken, or more precisely "not apparent in the ground state". As a fist example of spontaneous breaking, the Lagrangian for a complex scalar field, $\phi = (\phi_1 + i\phi_2)/\sqrt{2}$,

$$\mathcal{L} = (\partial_\mu \phi)^* (\partial^\mu \phi) - \mu^2 \phi^* \phi - \lambda (\phi^* \phi)^2 \tag{2.14}$$

is made invariant under a U(1) local gauge transformation: $\phi \rightarrow e^{i\alpha(x)}\phi$. As done in Section 2.2.1, ∂_μ is replaced by the covariant derivative given in Equation 2.4. The gauge invariant Lagrangian is then:

$$\mathcal{L} = (\partial^\mu + ieA^\mu)\phi^*(\partial_\mu - ieA_\mu)\phi - \mu^2\phi^*\phi - \lambda(\phi^*\phi)^2 - \frac{1}{4}F_{\mu\nu}F^{\mu\nu}. \tag{2.15}$$

In this case $\mu^2 < 0$, in order to allow the masses to be generated by the spontaneous symmetry breaking [2]. The field ϕ can be translated to a minimum energy position, without loss of generality. This is done by considering a potential $V(\phi)$ in the ϕ_1, ϕ_2 plane of radius v satisfying:

$$\phi_1^2 + \phi_2^2 = v^2 \quad \text{with} \quad v^2 = -\tfrac{\mu^2}{\lambda}. \tag{2.16}$$

This potential can be seen in Figure 2.1. The minimum energy position gives: $\phi_1 = v$ and $\phi_2 = 0$. ϕ can be expressed in terms of the η and ξ fields:

$$\phi(x) = \sqrt{\frac{1}{2}}\left[v + \eta(x) + i\xi(x)\right]. \tag{2.17}$$

Equation 2.15 becomes:

$$\mathcal{L}' = \frac{1}{2}(\partial_\mu\xi)^2 + \frac{1}{2}(\partial_\mu\eta)^2 + v^2\lambda\eta^2 + \frac{1}{2}e^2v^2A_\mu A^\mu - evA_\mu\partial^\mu\xi - \frac{1}{4}F_{\mu\nu}F^{\mu\nu} + \text{interaction - terms}. \tag{2.18}$$

The particle spectrum of $\mathcal{L}'$ appears to be a massless Goldstone boson ξ, a massive scalar η and a massive vector A_μ. The masses are then: $m_\xi = 0$, $m_\eta = \sqrt{2\lambda v^2}$ and $m_A = ev$. The gauge field has dynamically acquired mass. However, to avoid the presence of a massless Goldstone boson, a gauge transformation is required. This includes a different set of real fields:

$$\begin{aligned} \phi &\rightarrow \sqrt{\tfrac{1}{2}}\left(v + h(x)\right)e^{i\theta(x)/v}, \\ A_\mu &\rightarrow A_\mu + \tfrac{1}{ev}\partial_\mu\theta. \end{aligned} \tag{2.19}$$

In this particular choice of gauge, $\theta(x)$ is chosen such that h is real. The Lagrangian now takes the form:

$$\mathcal{L}'' = \frac{1}{2}(\partial_\mu h)^2 - \lambda v^2h^2 + \frac{1}{2}e^2v^2A_\mu^2 - \lambda vh^3 - \frac{1}{4}\lambda h^4 + \frac{1}{2}e^2A_\mu^2h^2 + ve^2A_\mu^2h - \frac{1}{4}F_{\mu\nu}F^{\mu\nu}. \tag{2.20}$$

Equation 2.20 describes two interacting massive particles, a vector boson A_μ and a massive scalar h, the Higgs particle. The massless Goldstone boson turned into the longitudinal polarization of the massive gauge

[2] if $\mu^2 > 0$ this is just the QED Lagrangian for a charged scalar particle of mass μ.

particles. Because of the introduction of h, this is known as the "Higgs mechanism".

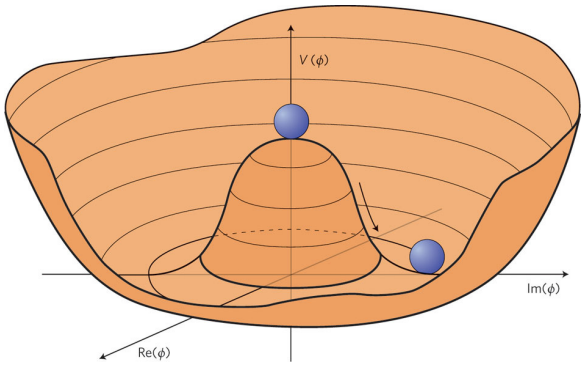

Figure 2.1: The potential $V(\phi)$ for a complex scalar field $\phi = (\phi_1 + i\phi_2)/\sqrt{2}$ for $\mu^2 < 0$ and $\lambda > 0$. The circle of minima has a radius v.

The Higgs mechanism described above corresponds to the spontaneous symmetry breaking of a U(1) gauge symmetry. For the case of weak boson masses, this must be done in SU(2) gauge symmetry. Thus, a similar derivation should be carried out in the Lagrangian:

$$\mathcal{L} = (\partial_\mu \phi)^\dagger (\partial^\mu \phi) - \mu^2 \phi^\dagger \phi - \lambda (\phi^\dagger \phi)^2 \tag{2.21}$$

where ϕ is an SU(2) doublet of complex scalar fields:

$$\phi = \begin{pmatrix} \phi_\alpha \\ \phi_\beta \end{pmatrix} = \sqrt{\frac{1}{2}} \begin{pmatrix} \phi_1 + i\phi_2 \\ \phi_3 + i\phi_4 \end{pmatrix}. \tag{2.22}$$

In this case, ∂_μ is replaced by the covariant derivative:

$$D_\mu = \partial_\mu + ig\frac{\tau_a}{2} W_\mu^a, \tag{2.23}$$

and introducing three gauge fields $W_\mu^a(x)$ with $a = 1, 2, 3$. With the appropriate gauge field transformation, the gauge invariant Lagrangian is:

$$\mathcal{L} = \left(\partial_\mu \phi + ig\frac{1}{2}\tau \cdot W_\mu \phi\right)^\dagger \left(\partial^\mu + ig\frac{1}{2}\tau \cdot W^\mu \phi\right) - V(\phi) - \frac{1}{4} W_{\mu\nu} W^{\mu\nu} \tag{2.24}$$

Then again, by introducing a proper potential $V(\phi)$:

$$V(\phi) = \mu^2 \phi^\dagger \phi + \lambda(\phi^\dagger \phi)^2, \tag{2.25}$$

expanding $\phi(x)$ at a particular minimum,

$$\phi_0 \equiv \sqrt{\frac{1}{2}} \begin{pmatrix} 0 \\ v \end{pmatrix}, \tag{2.26}$$

and parameterizing the fluctuations from the vacuum in terms of four real fields, the Lagrangian from Equation 2.24 becomes locally SU(2) invariant. This gauge invariant Lagrangian describes three massive gauge fields and one massive scalar (h). By comparing it with the typical mass term of a boson, $\frac{1}{2}M^2 B_\mu^2$, it is found that $M = \frac{1}{2}gv$.

The electroweak theory of Glashow, Weinberg and Salam proposed that the coupling of the $W^\pm$ and Z to leptons and quarks should be the same as that of the photon, that is e; the weak and the electromagnetic interactions were thus unified with the same coupling. A renormalized theory of electroweak interactions, incorporating the massive gauge bosons, is achieved by spontaneously breaking a local gauge symmetry as described above.

To incorporate electromagnetic interactions, a $\mathrm{U(1)_Y}$ symmetry is introduced, where the hypercharge operator, Y, is defined as:

$$\mathrm{Q} = \mathrm{T}^3 + \mathrm{Y}. \tag{2.27}$$

Q is the electric charge, and T^3 is the third generator of the $\mathrm{SU(2)_L}$ group, defined in terms of the Pauli matrices, σ: $\mathrm{T}^3 = \frac{1}{2}\sigma^3$. Electroweak interactions are finally based on the gauge group $\mathrm{SU(2)_L \times U(1)_Y}$, with gauge bosons W_μ^i, $i = 1, 2, 3$, and B_μ for the SU(2) and U(1) factors, respectively. The left handed fermion fields on the i^{th} fermion family transform as doublets under SU(2) and the right-handed fields are SU(2) singlets. An SU(2)×U(1) gauge invariant Lagrangian can now be expressed:

$$\mathcal{L} = \left| \left(i\partial_\mu - gT \cdot W_\mu - g' \frac{Y}{2} B_\mu \right) \phi \right|^2 - V(\phi) \tag{2.28}$$

In the minimal model, there are three fermion families and a single complex Higgs doublet, $\phi \equiv \begin{pmatrix} \phi^+ \\ \phi^0 \end{pmatrix}$

which is introduced for mass generation. To generate the boson masses, the Higgs potential of Equation 2.25 is used, along with $\mu^2 > 0$ and $\lambda > 0$. The appropriate vacuum expectation value is the one given in Equation 2.26. This choice of vacuum expectation value ensures that the vacuum remains invariant under $\mathrm{U(1)_{em}}$ transformations, the photon remains massless, and massive gauge bosons are generated along. From Equation 2.28 it can be shown that the masses of the bosons are:

$$M_W = \tfrac{1}{2} v g \quad \text{and} \quad M_Z = \tfrac{1}{2} v \sqrt{g^2 + g'^2}. \tag{2.29}$$

From there, it follows that $\frac{M_W}{M_Z} = \cos\theta_W$, with $\cos\theta_W = \frac{g}{\sqrt{g^2 g'^2}}$. θ_W is the weak mixing angle.

The same Higgs doublet used above is also sufficient to give masses to the leptons and quarks. This is accomplished by adding an interaction term, which involves Yukawa couplings of the scalars to the fermions. This interaction term is symmetric under $\mathrm{SU(2)_L \times U(1)_Y}$ and is a Lorentz scalar. The Higgs field couples the left- and right-handed fermions. The mass of the fermions can be expressed in terms of the corresponding Yukawa coupling, $m_f = \frac{1}{\sqrt{2}} \lambda_f v$, where v is the constant in the vacuum expectation value. In contrast to the boson masses, the fermion masses depend on a free parameter, the Yukawa coupling, not constrained by the model. It is clear, and interesting, that given the current experimental values of the quark masses the top quark Yukawa coupling is much larger than the Yukawa couplings for the rest of the quarks.

Cabibbo Kobayashi Maskawa Mixing Matrix

As mentioned above, the masses and mixing of quarks arise from the Yukawa interactions of the quarks with the Higgs field. When the Higgs acquires a vacuum expectation value, quark mass terms are generated. An important feature is that, as a consequence of the Higgs mechanism, the mass eigenstates of the physical quarks are rotated with respect to the electroweak eigenstates. The mass states are related to the electroweak states by the CKM matrix. As a result, the weak interactions couple to the physical up and down-type quarks with couplings given by the CKM matrix, $V_{\mathrm{CKM}} \equiv V_L^u V_L^{d\dagger}$:

$$V_{\mathrm{CKM}} = \begin{pmatrix} V_{ud} & V_{us} & V_{ub} \\ V_{cd} & V_{cs} & V_{cb} \\ V_{td} & V_{ts} & V_{tb} \end{pmatrix} \tag{2.30}$$

The CKM matrix is a 3×3 unitary matrix, $V_{\rm CKM}^{\dagger} V_{\rm CKM} = 1$, which can be parameterized by three mixing angles and a CP-violating phase. The unitarity of the CKM matrix imposes:

$$\sum_i V_{ij} V_{ik}^* = \delta_{jk} \quad \text{and} \quad \sum_i V_{ij} V_{kj}^* = \delta_{ik} \tag{2.31}$$

The current experimental values of the matrix elements are:

$$\begin{pmatrix} |V_{ud}| & |V_{us}| & |V_{ub}| \\ |V_{cd}| & |V_{cs}| & |V_{cb}| \\ |V_{td}| & |V_{ts}| & |V_{tb}| \end{pmatrix} = \begin{pmatrix} 0.97427 \pm 0.00015 & 0.22534 \pm 0.00065 & 0.00351\ ^{+0.00015}_{-0.00014} \\ 0.22520 \pm 0.00065 & 0.97344 \pm 0.00016 & 0.0412\ ^{+0.0011}_{-0.0005} \\ 0.00867^{+0.00029}_{-0.00031} & 0.0404\ ^{+0.0011}_{-0.0005} & 0.999146^{+0.000021}_{-0.000046} \end{pmatrix} \tag{2.32}$$

The magnitudes of the CKM elements just quoted were extracted from Reference [20]. These are determined by a global fit that uses all available measurements and imposes the SM constraints (three generation unitarity).

W- and Z-bosons Production and Decay Modes

At pp colliders the electroweak gauge bosons are produced as single particles or in pairs through a parton-parton process, for example the Drell-Yan production of W- and Z-bosons, $q\bar{q} \to Z$ and $q\bar{q}' \to W$. The Z-bosons decay into a pair of opposite charge fermions, that can either be two same-flavor leptons (e, μ, τ or ν) or two same-flavor quarks. The latter represents a hadronic final state, and it is the one with largest branching fraction ($\sim 70\%$). The W-boson can decay to a lepton and a neutrino of the same generation, or two quarks of the first or second generation. In this case too, the hadronic final state carries most of the branching fraction ($\sim 68\%$). Figure 2.2 shows the Feynman diagrams for the decays of these two bosons.

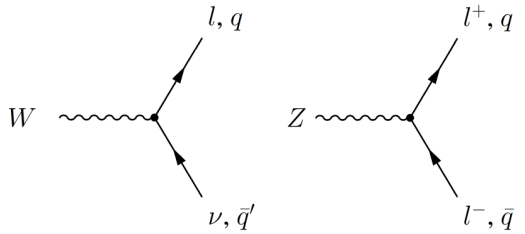

Figure 2.2: Decay modes of the W- and Z-bosons. In the case of the W-boson, the lepton ℓ carry the same charge as the boson.

2.3 Top Quark

The large mass of the top quark makes it a key element in the quest for deviations from the SM predictions. In particular, because of its large mass, it plays a larger role in radiative corrections than do lighter fermions. The large mass might also imply a special role in electroweak symmetry breaking, because the Higgs coupling to fermions is proportional to their mass. Several properties of the top quark have already been measured. So far, all of them in good agreement with the SM expectations. One important measurement is, as expected, the top quark mass. Figure 2.3 summarizes the mass measurements performed by both the ATLAS and the CMS experiments. The current best measurement of the mass is still held by the Tevatron 2011 average, $m_t = 173.2 \pm 0.6(\text{stat.}) \pm 0.8(\text{syst.})$ [2].

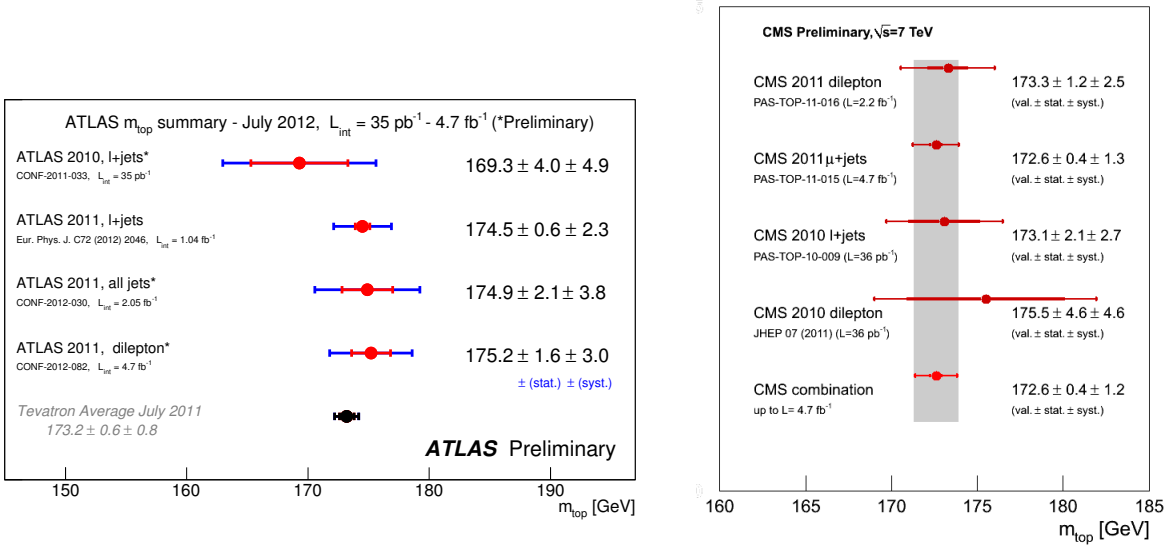

(a) (b)

Figure 2.3: Summary of measurements of the top quark mass by the (a)ATLAS and the (b) CMS experiment. In both cases, 2011 pp collision data at a center of mass energy of $\sqrt{s} = 7$ TeV were used.

2.3.1 $t\bar{t}$ Production and Decay

The LHC has been long advertised as a "top quark factory" due to the abundant production of this quark. More than 150,000 top pairs are expected in 1 fb^{-1} of data at a center-of-mass energy of 7 TeV.[3] Unlike the Tevatron, at the LHC these top quark pairs are produced mainly through gluon fusion diagrams $gg \to t\bar{t}$ ($\sim$ 90% of the time in the LHC), and secondly through quark annihilation $q\bar{q} \to t\bar{t}$ ($\sim$ 85% of the time in

[3]More than 200,000 top pairs at a center-of-mass energy of 8 TeV with the same integrated luminosity.

the Tevatron). Figure 2.4 shows the Feynman diagram for these processes.

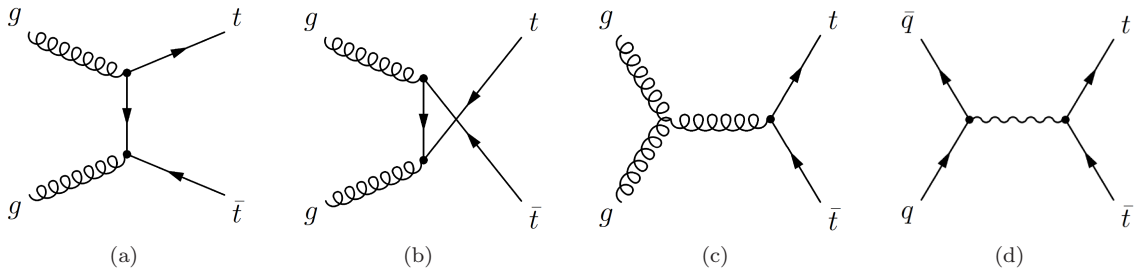

Figure 2.4: Feynman diagrams for top production processes at lowest level: (a), (b), and (c) gluon-gluon scattering diagrams, (d) quark-antiquark diagram.

The $t\bar{t}$ production cross section depends on the exact value of the top quark mass, m_t, and the collision energy. Figure 2.5 summarizes the results of the $t\bar{t}$ cross-section measurement by both ATLAS and CMS experiments, in different decay channels. These were done with 2011 collision data, at $\sqrt{s} = 7$ TeV. The combinations of the different channels yields $\sigma_{t\bar{t}} = 177 \pm 3(\text{stat.})^{+8}_{-7}(\text{syst.}) \pm 7(\text{lumi.})$ pb for ATLAS [21] and $\sigma_{t\bar{t}} = 166 \pm 2(\text{stat.}) \pm 11(\text{syst.}) \pm 8(\text{lumi.})$ pb for CMS [22]. Measurements for the 2012 collision energy, $\sqrt{s} = 8$ TeV, are on-going. Additionally, top quarks are produced via single-top quark production mechanisms. These, however have smaller production rates compared to the top pairs. Three subprocesses contribute to single-top quark pair production: the exchange of a virtual W-boson in the t-channel, or in the s-channel, and the associated production of a top quark and an on-shell W-boson. The t-channel mode is the process with highest cross section at the Tevatron and at the LHC.

The top quarks decay almost exclusively to $t \to Wb$ since the CKM matrix element V_{tb} is close to unity. The Feynman diagram for this decay is depicted in Figure 2.6(a). This means that the final state topology of processes involving top quarks is determined by the decay mode of the W-boson. As mentioned in Section 2.2.3 the hadronic final states have larger branching fractions, but in an environment with copious multijet production, such as the LHC, the leptonic modes provide cleaner signatures.

In addition to the SM favored decay, there are other decay channels, predicted to be smaller by several orders of magnitude in the SM. The second most likely decays are the CKM non-diagonal decays $t \to Ws$ and $t \to Wd$. The branching ratios (BR) are in the order of $\text{BR}(t \to Ws) \sim 1.6 \times 10^{-3}$ and $\text{BR}(t \to Wd) \sim$

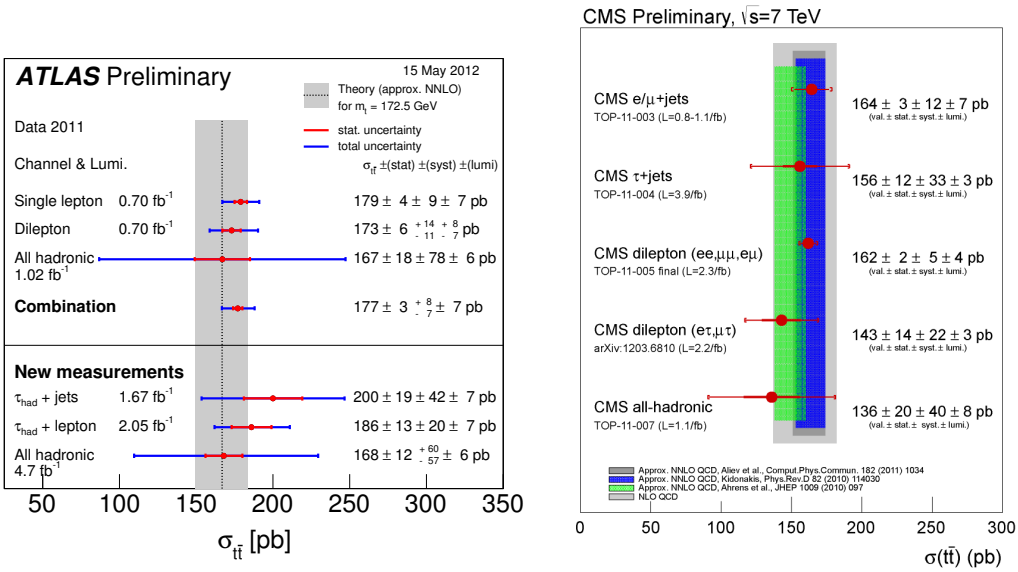

(a) (b)

Figure 2.5: Summary of measurements of the $t\bar{t}$ cross section by the (a)ATLAS and the (b) CMS experiment. In both cases, 2011 pp collision data at a center of mass energy of $\sqrt{s} = 7$ TeV were used. The combination of the different channels is $\sigma_{t\bar{t}} = 177 \pm 3(\text{stat.})^{+8}_{-7}(\text{syst.}) \pm 7(\text{lumi.})$ pb for ATLAS [21] and $\sigma_{t\bar{t}} = 166 \pm 2(\text{stat.}) \pm 11(\text{syst.}) \pm 8(\text{lumi.})$ pb for CMS [22].

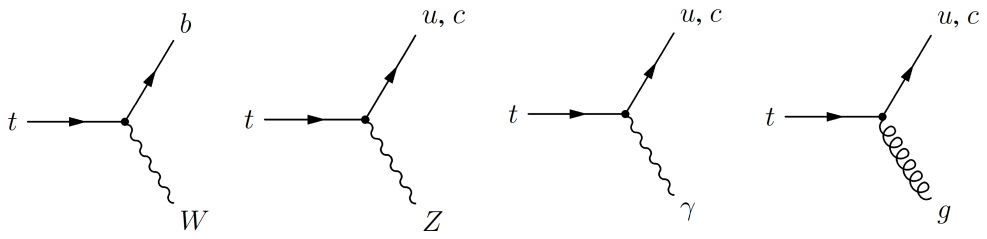

(a) SM decay, $t \to Wb$. (b) FCNC decay, $t \to Zq$. (c) FCNC decay, $t \to \gamma q$. (d) FCNC decay, $t \to gq$.

Figure 2.6: Feynman diagrams of Top quark decays. The FCNC deays in the SM are not present at tree level, thus the diagrams presented here are just for illustration.

1×10^{-4}, respectively. In what follows, for a generic decay channel X, the BR is defined as:

$$\text{BR}(t \to X) = \frac{\Gamma(t \to X)}{\Gamma(t \to Wb)_{\text{SM}}}. \tag{2.33}$$

Other rare decays include those that occur via flavor changing neutral currents. The last three diagrams in Figure 2.6 show such decays: $t \to Zq$, $t \to \gamma q$ and $t \to gq$. In the SM they occur at one loop level, and are highly suppressed by the Glashow-Iliopoulos-Maiani (GIM) mechanism [23], as explained below.

2.4 Flavor Changing Neutral Currents

Retaking the electroweak interactions discussion from Section 2.2.3, the $SU(2)_L \times U(1)_Y$ theory is based upon fermion doublets. The hadronic sector is built upon a single left-handed weak isospin doublets. The theory was self-consitent except for the hadronic charge description. In particular, the weak neutral current interaction contained a flavor-changing (strangeness-changing, as first studied) term. This is phenomenologically incorrect, because of many experimental limits placed on the rates of decays mediated by strangeness-changing neutral currents processes (like $K^+ \to \pi^+ \nu\bar{\nu}$, interpreted in terms of the elementary transition $\bar{s} \to \bar{d}\nu\bar{\nu}$). An elegant solution, to guard against this flavor changing neutral currents interactions, is that of the GIM mechanism. The key observation is that by introducing a new "charmed" quark, c, the weak isospin partner of s, the offending terms cancel.

The electroweak Lagrangian describing the interactions between quarks and bosons can be separated in three components: one related to the electromagnetic boson, one to the weak charged boson, and one to the weak neutral current. From there, the leading order interactions can be extracted. For the case of weak bosons these are: charged current interactions between the down-type and (anti-)up-type quarks (i.e. it is a flavor-changing interaction) and neutral current interactions containing only interactions of up-type quarks with anti-up-type quarks, and down-type quarks with anti-down-type quarks (i.e. neutral currents do not change flavors of quarks).

There are, however, higher order electroweak interactions that allow FCNC. These come from loop diagrams, like the ones shown in Figure 2.7, and box diagrams. However, the GIM mechanism is such, that the FCNC contribution vanishes if the masses of the quarks involved in the three contributing loop diagrams are identical. This is possible because the contribution from these diagrams can be factorized such that the unitarity constraint from the CKM matrix plays a role. In the case of the diagram presented in Figure 2.7, for the $t \to Zc$ decay, the contribution:

$$\propto f(m_d^2/m_W^2) \cdot V_{cd}V_{td}^* + f(m_s^2/m_W^2) \cdot V_{cs}V_{ts}^* + f(m_b^2/m_W^2) \cdot V_{cb}V_{tb}^*, \tag{2.34}$$

where $f(x)$ denotes a linear combination of Inami-Lin functions, is suppressed by the CKM matrix unitarity constraint from Equation 2.31:

$$V_{cd}V_{td}^* + V_{cs}V_{ts}^* + V_{cb}V_{tb}^* = 0. \tag{2.35}$$

as the masses of the quarks involved approach one another. If the masses of d, s and b quarks were identical, the expression in Equation 2.34 would be exactly zero. Since the masses are so close to each other [4], it is only highly suppressed. This also explains why the FCNC branching fractions for the top quark are more suppressed than for the bottom quark (e.g. $b \to sZ$ decay). In the case of the FCNC decays of the top quark, the quarks contributing to the loop diagrams, down-type quarks, have masses more similar than those contributing to the FCNC decays of the b quark, up-type quarks.

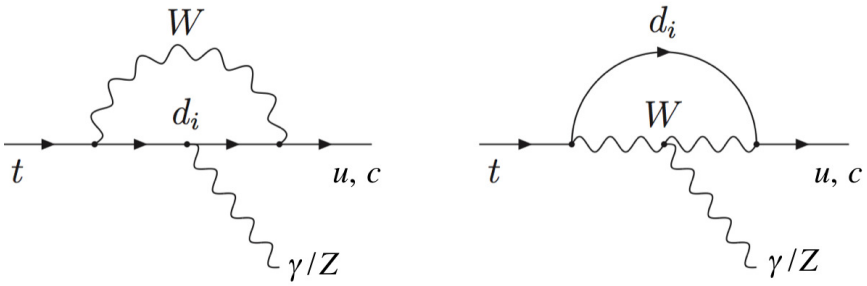

Figure 2.7: Example of a higher order loop diagram allowed in the SM. In these diagrams d_i can be either of the three down-type quarks. Thus, in each case there are possible three diagrams.

2.4.1 Flavor Changing Neutral Currents in Top Quark Decays

So according to the SM, FCNC are forbidden at tree level and are highly suppressed at one loop level compared to the dominant decay mode. In particular, the predicted BR for the $t \to Zq$ decay are in the order of $\sim 10^{-16}$ and $\sim 10^{-14}$ for $q = u$ and $q = c$, respectively, as shown in Table 2.3. There are, however, several SM extensions that predict higher BR for the top quark FCNC decays. Examples of such decays are the quark-singlet model (QS) [3, 24, 25], the two-Higgs doublet model with (FC 2HDM) or without (2HDM) flavor-conservation [26–31], the minimal supersymmetric model (MSSM) [32–38], supersymmetry (SUSY) with R-parity violation ($\not{R}$ SUSY) [39], the Topcolor-assisted Technicolor model (TC2) [40], or models with warped extra dimensions (RS) [41, 42]. Table 2.3 summarizes these predicted BR values for these models, along with those predicted by the SM.

In models with new extra quarks the 3×3 CKM matrix is no longer unitary and the GIM mechanism suppressing the SM amplitudes no longer provides full cancellation of the FCNC terms. In the QS model, where the new quark is an $SU(2)_L$ singlet with charge $Q = 2/3$, tree-level FCNC scalar interactions that enhance the BR($t \to Zq$) to up to $\sim 1.1 \times 10^{-4}$ are predicted. The decay rates of $t \to \gamma q$ and $t \to gq$ are

[4] in the scale of m_W, the difference between m_b and $m_{d,s}$ can be taken as to be small.

Process	SM	QS	2HDM	FC 2HDM	MSSM	$\not{R}$ SUSY	TC2	RS
$t \to u\gamma$	3.7×10^{-16}	7.5×10^{-9}	—	—	2×10^{-6}	1×10^{-6}	—	$\sim 10^{-11}$
$t \to uZ$	8×10^{-17}	1.1×10^{-4}	—	—	2×10^{-6}	3×10^{-5}	—	$\sim 10^{-9}$
$t \to ug$	3.7×10^{-14}	1.5×10^{-7}	—	—	8×10^{-5}	2×10^{-4}	—	$\sim 10^{-11}$
$t \to c\gamma$	4.6×10^{-14}	7.5×10^{-9}	$\sim 10^{-6}$	$\sim 10^{-9}$	2×10^{-6}	1×10^{-6}	$\sim 10^{-6}$	$\sim 10^{-9}$
$t \to cZ$	1×10^{-14}	1.1×10^{-4}	$\sim 10^{-7}$	$\sim 10^{-10}$	2×10^{-6}	3×10^{-5}	$\sim 10^{-4}$	$\sim 10^{-5}$
$t \to cg$	4.6×10^{-12}	1.5×10^{-7}	$\sim 10^{-4}$	$\sim 10^{-8}$	8×10^{-5}	2×10^{-4}	$\sim 10^{-4}$	$\sim 10^{-9}$

Table 2.3: The theoretical values for the branching fractions of FCNC top quark decays predicted by the SM and exotic extensions (see text for references).

also enhanced due to the partial breaking of the 3×3 CKM unitarity and the presence of extra Feynman diagrams at the one-loop level. In 2HDM models, where FCNC interactions with scalars are also present at the tree-level, the prediction for the FCNC decays is also altered. The new scalar fields give radiative contributions to the Ztq, γtq and gtq vertices. The resulting BR can be up to $\mathrm{BR}(t \to cZ) \sim 10^{-7}$ with smaller values for decays to an up quark. The BR for the γq and gq channels is shown in Table 2.3. If a discrete symmetry is imposed, the FCNC interactions can be forbidden at tree-level. In this case (FC 2HDM) the rate for top FCNC decays are still increased significantly with respect to the SM. SUSY could affect the top quark decays in different ways. In the MSSM with universal soft breaking, by relaxing the universality with a large flavor mixing between the 2^{nd} and 3^{rd} family, the BRs can reach values such as those presented in Table 2.3. The introduction of baryon number violating couplings in $\not{R}$ SUSY could give even larger enhancements, on the order of $\sim 10^{-4}$ for the $t \to Zc$ decay [43, 44].

Experimental searches for FCNC decays of the top quark

The present experimental limits on the branching fractions of the FCNC top quark decay channels established by experiments at the LEP, HERA and Tevatron colliders are shown in Table 2.4. These decays can be studied directly by searching for final states with the corresponding decay particles. However the $t \to gq$ mode (q denotes either an up quark or charm quark), is almost impossible to separate from generic multijet processes, and a much better sensitivity is achieved in the search for anomalous single top-quark production [56].

Previous to the LHC searches, the best experimental limit on the FCNC decay $t \to Zq$, was held by the D0 Collaboration [4]. Using 4.1 fb^{-1} of $\sqrt{s} = 1.96$ TeV collision data from the Tevatron, a search for FCNC was performed in $t\bar{t}$ events, where either one or both of the top quarks decay via $t \to Zq$. Any other top quark not decaying via FCNC is assumed to decay via $t \to Wb$. Only channels where the W- and Z-bosons decay leptonically are used. Figure 2.8(a) shows the reconstructed invariant mass distribution of the top

	LEP	HERA	Tevatron	LHC
BR($t \to q\gamma$)	2.4% [45–49]	0.64% ($tu\gamma$) [50]	3.2% [54]	—
BR($t \to qZ$)	7.8% [45–49]	49% (tuZ) [51]	3.2% [4]	0.73% [8]
BR($t \to qg$)	17% [44]	13% [51–53]	2.0×10^{-4} (tug) 3.9×10^{-3} (tcg) [55]	5.7×10^{-5} (tug) 2.7×10^{-4} (tcg) [56]

Table 2.4: Present experimental 95% CL upper limits on the branching fractions of the FCNC top quark decay channels.

quarks decaying via FCNC for events with at least one jet. The limit in the branching ratio, however, was extracted for events without any restriction on the number of jets. In the absence of signal, a limit on branching ratio for this decay was observed at BR($t \to Zq$) < 3.2% at the 95% confidence level. This was, in fact, the first search for FCNC in $t\bar{t}$ events in trilepton final states. The CDF Collaboration previously reported a search for FCNC $t \to Zq$ decays in $t\bar{t}$ events [57]. In this case, 1.9 fb^{-1} of $\sqrt{s} = 1.96$ TeV collision data from the Tevatron were used. Events with two leptons and four jets in the final states were used. This final state topology occurs when one of the top quarks decays via FCNC to Zq, followed by the Z-boson decaying into a pair of leptons, and the other top quark decaying to Wb followed by the hadronic decay of the W-boson. This result excludes branching ratios of BR($t \to Zq$) > 3.7% at the 95% confidence level. Figure 2.8(b) shows the χ^2 distribution for events in different regions. In this case, χ^2 is defined in terms of the reconstructed masses of the two top quarks and the W-boson. For further details see Reference [57].

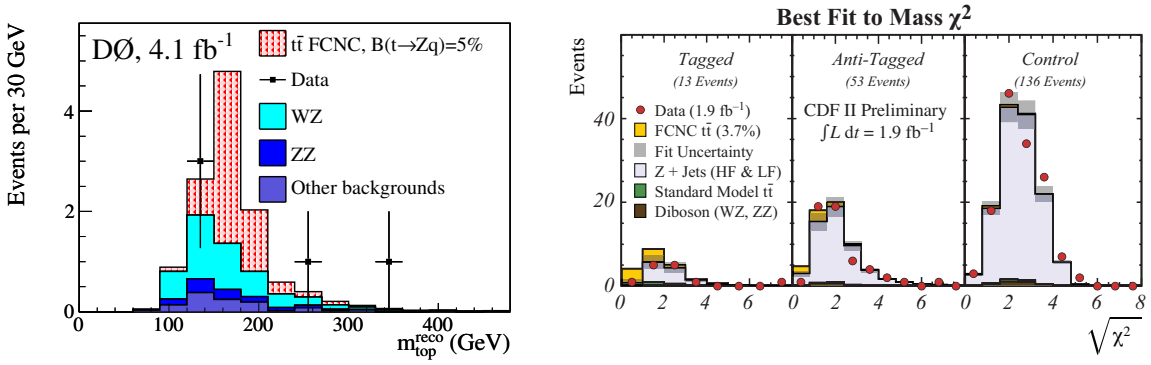

(a) (b)

Figure 2.8: (a) Reconstructed top quark mass distribution, m_t^{reco}, of data, FCNC $t\bar{t}$ signal, and expected background for events with $n_{\text{jet}} \geq 1$ from the FCNC search performed by D0 experiment [4]. (b) Mass χ^2 distribution for signal regions with (b-tagged) and without (anti-tagged) an identified b-jet and the control region from the CDF search of FCNC in top quark decays [57].

2.5 Top Quark Physics Beyond the Standard Model

As mentioned at the beginning of this chapter, the SM has proven rather successful in the description of experimental results. Figure 2.9 shows a summary of the SM production cross-section for different processes measured by the ATLAS experiment and compared to the theoretical expectations. Similar measurements can be found for the CMS experiment. There are, however, a number of shortcomings with the SM. For instance, the SM does not account for the existence of dark matter and dark energy, the baryon asymmetry of the universe, non-zero mass of the neutrinos, and furthermore it does not solve the hierarchy problem. Another question, directly related to the top quark, can be raised: why are the masses of the charged leptons as they are? Some of these questions might actually be answered, or hints given, at the LHC as more data is being collected. However, as of now, divergences from the SM are yet to be found. Several extensions to the SM have been formulated, in an attempt to answer some of those questions. One of the most common examples of those theories is SUSY, which postulates a fermion-boson symmetry, and provides a solution to the hierarchy problem.

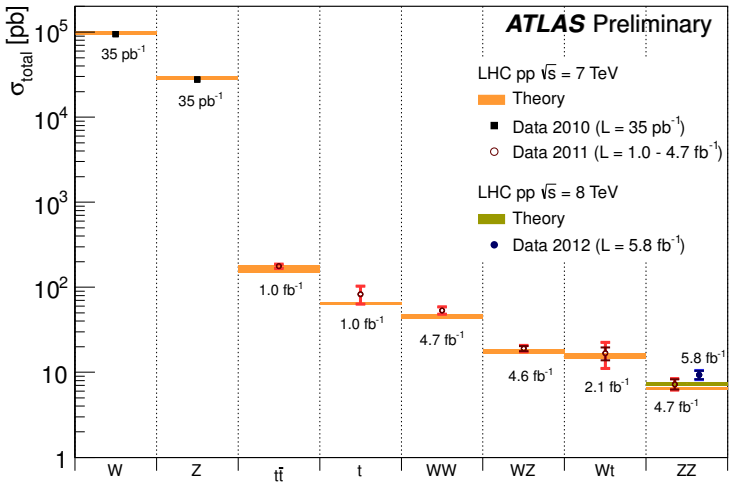

Figure 2.9: Summary of several Standard Model total production cross section measurements performed by the ATLAS experiment compared to the corresponding theoretical expectations. The error bars include the full uncertainty, both statistical and systematic. All theoretical expectations were calculated at NLO or higher.

Top quark physics, because of its recent discovery, is a rather new field. Several analyses currently on-going, will provide more precision to known quantities, and possibly hints of new physics will be found. Some of those analysis specifically aim for physics BSM. Examples of these are analyses are: studies related

to Wtb couplings, where limits on anomalous couplings are being computed, searches for 4^{th} generation quarks b' in Wt and searches for $t\bar{t}$ resonances. The FCNC search presented in this thesis is also part of this classification. More specifically, many of the theories listed in Section 2.4.1 could be probed at the LHC once more data is collected. In the scenario of no evidence for new physics found at the LHC, a future linear collider might be able to improve on the LHC bounds on the BRs, depending on the energy and especially on the luminosity of such collider [58].

The understanding of particle physics is rapidly evolving, the successful operation of the LHC not only allows experiments to increase the precision of measurements and confirm predictions of never-before measured quantities, but it also opens the door for testing of physics BSM. In particular, the just announced 5 σ significance finding of a new boson [59] in agreement with the SM Higgs boson, by both the ATLAS and the CMS experiments, has brought hope to the scientific community. This observation could be either further confirmation of the SM, or a hint to new physics. The rest of the 2012 data might bring light into this question. In the context of Higgs searches, the top quark plays a key role. Not only because some top quark processes are important backgrounds to some of those Higgs searches, but also because the top quark can be part of the production or decay of the Higgs boson itself. Examples of this are the top quark decay $t \to Hb$ (for a non-SM charged Higgs) and the $t\bar{t}H$ Higgs production.

Chapter 3

The LHC and the ATLAS Detector

3.1 Introduction

The Large Hadron Collider (LHC) at CERN near Geneva is the world's largest and most energetic particle accelerator. It has been designed to collide proton beams with a center-of-mass energy of up to 14 TeV, and a nominal luminosity of 10^{34} cm^{-2}s^{-1}. The high energy and luminosity of the LHC allows the study of a large range of physics, from the precise measurements of known quantities to the exploration of physics beyond the SM. Within this motivation, the ATLAS detector (A Toroidal LHC ApparatuS) has been designed as a general purpose detector to probe proton-proton collisions and accommodate a very large spectrum of physics foreseen at the TeV scale.

3.2 The LHC

The LHC is a two-ring, superconducting, hadron accelerator and collider installed in the tunnel 27 km in circumference initially built for LEP. Unlike how it is done in the Tevatron, the high beam intensities required by the high luminosity exclude the use of anti-proton beams, and hence exclude the particle-anti-particle collider configuration of a common vacuum and magnet system for both circulating beams. Therefore the LHC is designed as a proton-proton collider with separate magnet dipole fields and vacuum chambers in the main arcs and with common sections only at the insertion regions where the experimental detectors are located [60, 61].

One figure of merit in colliders such as the LHC is the luminosity:

$$\mathcal{L} = \frac{N_b^2 n_b f_{\text{rev}} \gamma_r}{4\pi \varepsilon_n \beta^*} F \tag{3.1}$$

where N_b is the number of particles per bunch, n_b the number of bunches per beam, f_{rev} the revolution frequency, γ_r the relativistic gamma factor, ε_n the normalized transverse beam emittance, β^* the beta func-

tion at the collision point, and F the geometric luminosity reduction factor due to the crossing angle at the interaction point. A simplified list of designed LHC beam parameters at the peak luminosity is given in Table 3.1

	injection	collision
Proton energy [GeV]	450	7000
Relativistic gamma	479.6	7461
Number of particles per bunch	1.15×10^{11}	
Number of bunches	2808	
Bunch spacing [ns]	24.95	
Longitudinal emittance (4σ) [eVs]	1.0	2.5
Transverse normalized emittance [μm rad]	3.5	3.75
Circulating beam current [A]	0.584	
Stored energy per beam [MJ]	23.3	362
Geometric luminosity reduction factor	-	0.836

Table 3.1: LHC beam parameters relevant to the peak luminosity of 10^{34} cm^{-2}s^{-1}. The quoted geometric reduction factor assumes a total crossing angle of 285 μrad at the interaction point [61].

The LHC is supplied with protons from the injector chain: Linac2 - Proton Synchrotron Booster (PSB) - Proton Synchrotron (PS) - Super Proton Synchrotron (SPS), as shown in Figure 3.1. Each of these components accelerate protons (stripping off electrons from hydrogen atoms) to 50 MeV, 1.4 GeV, 26 GeV, and 450 GeV, respectively, before injecting them into the following component, or the LHC in the case of the SPS. These accelerators have been upgraded to meet the new challenging needs of the LHC: many high intensity proton bunches with small transverse and well defined longitudinal emittances. The "end-point" beam requirements are summarized by Equation 3.1, but they also imply several conditions to be satisfied. Example of these conditions are: the space-charge limit in the injector, which scales with N_b/ε_n and the total intensity $N_b \cdot n_b$ which is limited by the thermal energy produced by the synchrotron radiation which must be absorbed by the cryogenic system [60, 62, 63].

The LHC has two high luminosity detectors, ATLAS and CMS, aiming to operate at the peak luminosity of 10^{34} cm^{-2}s^{-1} in the LHC proton operation. In addition to these high luminosity experiments, the LHC has two low luminosity experiments: LHCb for B-physics, aiming at a peak luminosity of 10^{32} cm^{-2}s^{-1} and TOTEM for the detection of protons from elastic scattering at small angles aiming at a peak luminosity of 2×10^{29} cm^{-2}s^{-1} with 156 bunches. In addition to the proton beams the LHC will also be operated with ion beams. The LHC has one dedicated ion experiment: ALICE, aiming at a peak luminosity of 10^{27} cm^{-2}s^{-1}

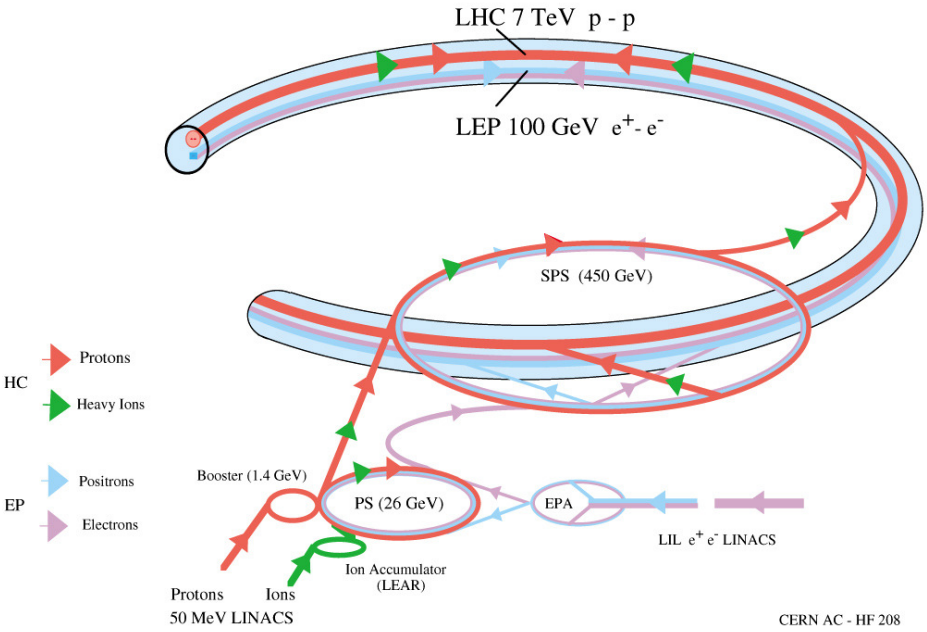

Figure 3.1: The LHC injection complex.

for nominal Pb-Pb ion operation.

3.3 The ATLAS Detector

Due to the experimental conditions at the LHC, the detectors require fast electronics and sensor elements. High detector granularity, good charged particle momentum resolution, particle identification and large geometrical coverage are needed as well. To satisfy such requirements, the ATLAS detector comprises several technologies, each of which has been developed to pursue specific goals. The inner detector is a combination of high-resolution semiconductor pixel (Pixel) and strip (SCT) detectors in its inner part, and transition radiation tracking (TRT) detectors in its outer part. The high granularity lead/liquid-argon (LAr) electromagnetic (EM) sampling calorimeters have excellent performance in terms of energy and angular resolution, along with electron/photon identification. The hadronic calorimetry is done by an iron/scintillating-tile calorimeter, which provides a good jet and missing energy performance. The calorimeter is surrounded by the muon spectrometer, instrumented with separate trigger and high-precision tracking chambers [64].

The ATLAS detector covers nearly the entire solid angle around the collision point. Its geometry is defined by the direction of the beam, with the z-axis parallel to it, and the x-y plane transverse to it.

The positive x-direction is defined as pointing from the interaction point to the center of the LHC ring and the positive y-axis is defined as pointing upwards. The azimuthal angle, ϕ, is measured around the beam axis, and the polar angle θ is the angle from the beam axis. The pseudorapidity is defined as $\eta \equiv -\ln\tan(\theta/2)$. The distance between objects 1 and 2 in the pseudorapidity-azimuthal angle space, is defined as $\Delta R \equiv \sqrt{(\phi_1 - \phi_2)^2 + (\eta_1 - \eta_2)^2}$. The transverse momentum, p_T, is defined as $p\sin\theta$, where p is the momentum. The transverse energy, E_T, is defined as $E\sin\theta$, where E is the energy measured in the calorimeter, and θ is the polar angle of the energy deposition.

Figure 3.2 shows a cut-away view of the detector, where the layout of the different components can be appreciated. Figure 3.3 displays these components separately. Table 3.2 provides a summary of expected energy-momentum resolution of each component, along with their coverage in η.

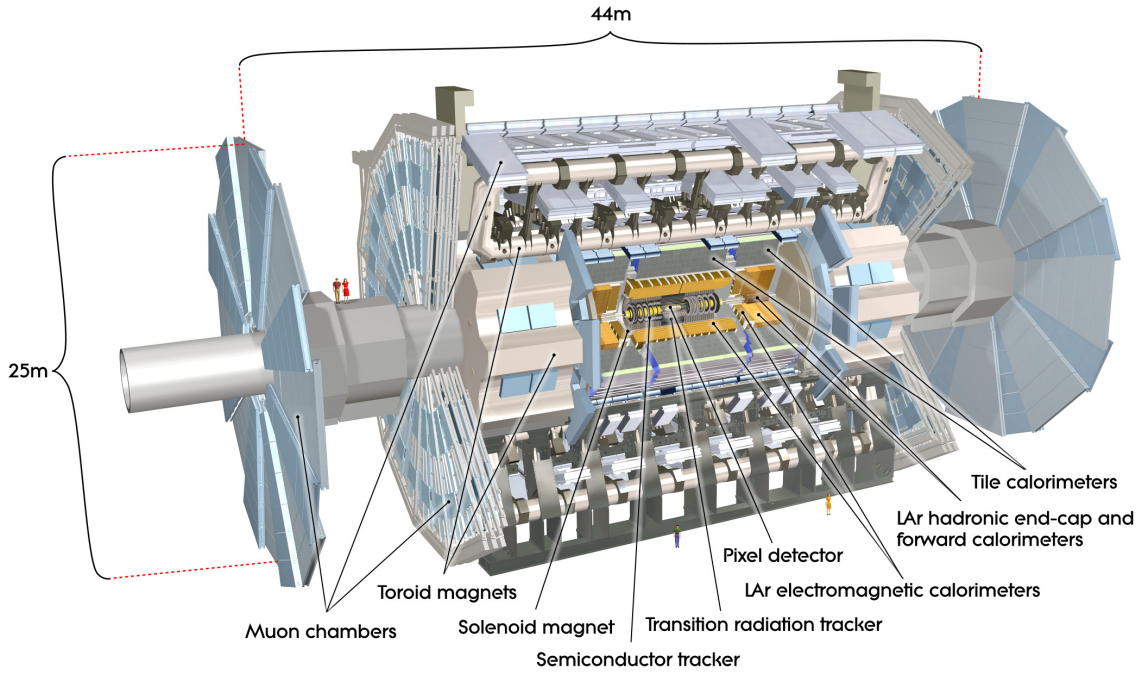

Figure 3.2: Cut-away view from the ATLAS detector [64].

3.3.1 Magnet System

The ATLAS superconducting magnet system can be seen in Figure 3.3(a). It consists of a thin central solenoid (CS), providing the inner detector with a 2 T axial magnetic field, surrounded by a system of three

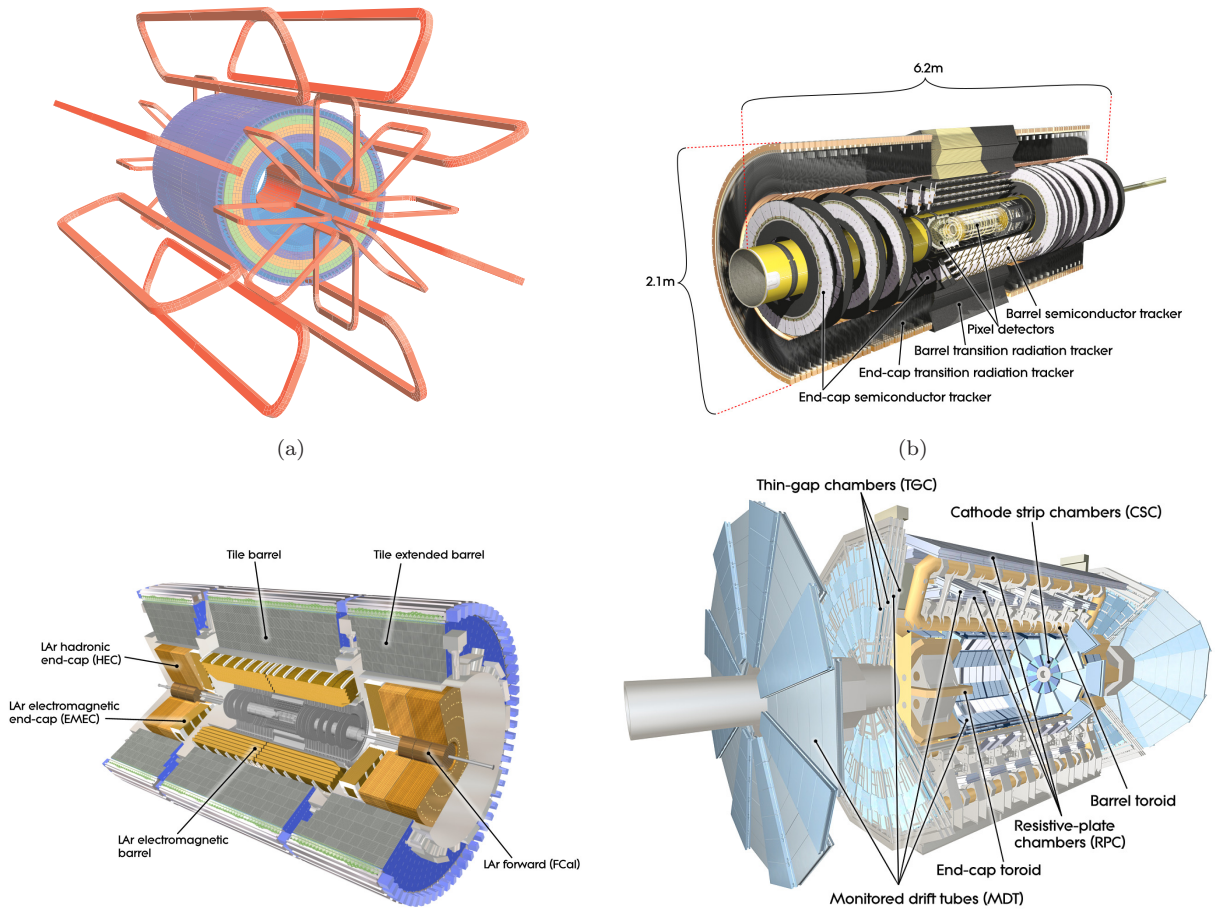

(a) (b) (c) (d)

Figure 3.3: ATLAS Detector components overview: (a) Magnet system, (b) Inner detector, (c) EM and hadronic calorimeters, and (d) Muons spectrometer [64]. In (a) the eight barrel toroid coils, with the end-cap coils interleaved are visible. The solenoid winding lies inside the calorimeter volume.

large air-core toroids (one barrel and two end-caps) generating the magnetic field for the muon spectrometer. The peak magnetic field on the superconductors in the barrel and end-cap toroids are 3.9 and 4.1 T respectively. The two end-cap toroids (ECT) are inserted in the barrel toroid (BT) at each end and line up with the CS. Each of the three toroids consists of eight coils assembled radially and symmetrically around the beam axis. The ECT coil system is rotated by 22.5° with respect to the BT system in order to provide radial overlap and to optimize the bending power in the interface regions of both coil systems. The bending power between the inner and outer radius of the toroids is between 1.5 and 5.5 Tm for the BT, and between 1 to 7.5 Tm in the region $1.6 < |\eta| < 2.7$ for the ECT. The bending power is lower in the transition regions where the two magnets overlap ($1.4 < |\eta| < 1.6$) [64–66].

3.3.2 Tracking

The inner detector tracking system is mainly designed to reconstruct tracks and vertices with high efficiency, perform precise measurements of leptons, and have good identification of individual particles in dense jets. Charged particles trajectories are reconstructed and their momenta measured due to the 2 T magnetic field generated by the central solenoid. Figure 3.3(b) shows the Inner Detector layout. It combines high-resolution detectors at inner radii with continuos tracking elements at outer radii. The former is achieved with semiconductor detectors, whereas the latter one is provided by the TRT.

The pixel and SCT precision tracking detectors cover the region of $|\eta| < 2.5$, with about 80.4 and 6.3 million readout channels respectively. The Pixel detector is a high-granularity tracking detector designed to provide a set of measurements as close to the interaction point as possible. The system consists of three concentric barrels at average radii of $\sim$ 4 cm, 11 cm, and 14 cm from the beam axis, and four disks on

Detector Component	Required resolution	η coverage	
		Measurement	Trigger
Tracking	$\sigma_{p_T}/p_T = 0.05\%\ p_T \oplus 1\%$	± 2.5	
EM calorimetry	$\sigma_E/E = 10\%/\sqrt{E} \oplus 0.7\%$	± 3.2	± 2.5
Hadronic calorimetry (jets)			
barrel and end-cap	$\sigma_E/E = 50\%/\sqrt{E} \oplus 3\%$	± 3.2	± 3.2
forward	$\sigma_E/E = 100\%/\sqrt{E} \oplus 10\%$	$3.1 < \|\eta\| < 4.9$	$3.1 < \|\eta\| < 4.9$
Muon spectrometer	$\sigma_{p_T}/p_T = 10\%$ at $p_T = 1$ TeV	± 2.7	± 2.4

Table 3.2: General performance goals of the ATLAS detector. The units for E and p_T are in GeV. For high-p_T muons the muon spectrometer performance is independent of the inner-detector system.

each end-cap, between radii of 11 and 20 cm perpendicular to it, which complete the angular coverage segmented in $R-\phi$ and z. All pixel sensors are identical, with a minimum pixel size of 50×400 μm^2, and a two-dimensional segmentation, giving space points without any of the ambiguities associated with projective geometries. In the barrel, the intrinsic accuracies are 10 μm ($R-\phi$) and 115 μm (z), and in the disks are 10 μm ($R-\phi$) and 115 μm (R). The impact parameter resolution, an important parameter that influences the efficiency of the inner detector for finding short-lived particles, such as b-quarks and τ-leptons is determined by the precision of the pixel system. The innermost layer of pixels, at a radius of about 5 cm from the beam line, enhances the secondary vertex measurement performance.

The SCT is made of semiconductor strips, arranged in eight layers, which can give information of four spatial points for each track. In the barrel uses small-angle (40 mrad) stereo strips to measure both coordinates with an intrinsic accuracy of 17 μm ($R-\phi$) and 580 μm (z). In the end-cap region, the disks have a set of strips running radially and a set of stereo strips at an angle of 40 mrad, with intrinsic accuracies of 17 μm ($R-\phi$) and 580 μm (R).

The outermost system in the inner detector is the TRT, providing track reconstruction up to $|\eta| = 2.0$. Its 4 mm diameter straw tubes only provide $R-\phi$ information, typically 36 hits per track, with an accuracy of 130 μm per straw. In the barrel region, the straws are 144 cm long, parallel to the beam axis, and in the end-cap region, the 37 cm long straws are arranged radially in wheels. it has approximately 351,000 read-out channels. Due to the detection of transition-radiation photons in the TRT, the electron identification capabilities are enhanced.

The parameters for the different systems are summarized in Table 3.3. At least eight strip layers (four space points) and three pixel layers are crossed by each track in this design. In addition, the large number of tracking points given by the TRT, provides the possibility of continuos track reconstruction with much less material per point at a lower cost than the Pixels. The combination of the two techniques gives high precision in both ϕ and z coordinates. The TRT hits contribute to the momentum measurement, with lower precision per point (compared to the silicon) but compensated by the large number of measurements. The relative precisions of the different measurements are well matched, so that no single measurement dominates the momentum resolution [64, 65, 67].

3.3.3 Calorimetry

The calorimetry is done by an EM calorimeter covering the region $|\eta| < 3.2$, a barrel hadronic calorimeter covering $|\eta| < 1.7$, hadronic end-cap calorimeters covering $1.5 < |\eta| < 3.2$, and forward calorimeters covering $3.1 < |\eta| < 4.9$. In the η regions where matching information from the inner detector is available, the fine granularity of the EM calorimeter provides high-precision measurements of electrons and photons. The rest of the calorimeter, despite its coarser granularity, still ensures good resolution for jet reconstruction and measurement of missing energy. Together with the large η coverage, the calorimeter depth has been optimized to provide good containment for electromagnetic and hadronic showers, limiting punch-through into the muon system [64, 65, 68]. The layout of the different calorimeters is presented in Figure 3.3(c). The rapidity coverage, granularity and longitudinal segmentation of the ATLAS calorimetry are summarized in Table 3.4.

Electromagnetic calorimeter

An accordion geometry has been chosen for the absorbers and the electrodes of the barrel and end-cap EM calorimeters. Such geometry provides full coverage in ϕ without any azimuthal cracks. The thickness of the absorber, made of lead plates, has been chosen as a function of η, so as to optimize the calorimeter performance in terms of energy resolution. It is divided into a barrel ($|\eta| < 1.475$) and two end-cap ($1.374 < |\eta| < 3.2$) components, which are housed in two separate cryostats. In the barrel, the accordion waves are axial and run in ϕ, and the folding angles of the waves vary with radius to keep the LAr gap constant. In the end-caps, the waves are parallel to the radial direction and run axially. In the region

System	position	area [m^2]	resolution σ [μm]	channels (10^6)	η coverage
Pixels	1 removable barrel layer	0.2	$R\phi = 10$, $z = 115$	16	± 2.5
	2 barrel layers	1.4	$R\phi = 10$, $z = 115$	81	± 1.7
	4 end-cap disks on each side	0.7	$R\phi = 10$, $R = 115$	43	$1.7 - 2.5$
SCT	4 barrel layers	34.4	$R\phi = 17$, $z = 580$	3.2	± 1.4
	9 end-cap wheels on each side	26.7	$R\phi = 17$, $R = 580$	3.0	$1.4 - 2.5$
TRT	axial barrel straws		130 (per straw)	0.10	± 0.7
	radial end-cap straws 36 straws per track		130 (per straw)	0.32	$0.7 - 2.5$

Table 3.3: Main parameters of the inner detector. The quoted resolutions are typical values. The actual resolution in each detector is η-dependent [67].

$|\eta| < 1.8$, a presampler detector is used to correct for the energy lost by electrons and photons upstream of the calorimeter. In the transition region between the barrel and the end-cap calorimeters, $|\eta| \sim 1.45$, the detector response is deteriorated with respect to the rest of the acceptance. This "crack region" is not used for photon identification nor for precision measurements for electrons. The resolution goal of the EM calorimeter, as quoted in Table 3.2, is $\sigma_E/E = 10\%/\sqrt{E} \oplus 0.7\%$. This is needed to achieve a mass resolution

EM calorimeter	barrel	end-cap	
coverage	$\|\eta\| < 1.465$	$1.375 < \|\eta\| < 3.2$	
longitudinal segmentation	3 samplings	3 sampling	$1.5 < \|\eta\| < 2.5$
		2 sampling	$1.375 < \|\eta\| < 1.5$
			$2.5 < \|\eta\| < 3.2$
granularity ($\Delta\eta \times \Delta\phi$)			
sampling 1	0.003×0.1	0.025×0.1	$1.375 < \|\eta\| < 1.5$
		0.003×0.1	$1.5 < \|\eta\| < 1.8$
		0.003×0.1	$1.8 < \|\eta\| < 2.0$
		0.003×0.1	$2.0 < \|\eta\| < 2.5$
		0.1×0.1	$2.5 < \|\eta\| < 3.2$
sampling 2	0.025×0.025	0.025×0.025	$1.375 < \|\eta\| < 2.5$
		0.1×0.1	$2.5 < \|\eta\| < 3.2$
sampling 3	0.050×0.025	0.05×0.025	$1.5 < \|\eta\| < 2.5$
Presampler	barrel	end-cap	
coverage	$\|\eta\| < 1.52$	$1.5 < \|\eta\| < 1.8$	
longitudinal segmentation	1 sampling	1 sampling	
granularity ($\Delta\eta \times \Delta\phi$)	0.025×0.1	0.025×0.1	
Hadronic tile	barrel	end-cap	
coverage	$\|\eta\| < 1.0$	$0.8 < \|\eta\| < 1.7$	
longitudinal segmentation	3 sampling	3 sampling	
granularity ($\Delta\eta \times \Delta\phi$)			
samplings 1 and 2	0.1×0.1	0.1×0.1	
samplings 3	0.2×0.1	0.2×0.1	
Hadronic LAr		end-cap	
coverage		$1.5 < \|\eta\| < 3.2$	
longitudinal segmentation		3 samplings	
granularity ($\Delta\eta \times \Delta\phi$)		0.1×0.1	$1.5 < \|\eta\| < 2.5$
		0.2×0.2	$2.5 < \|\eta\| < 3.2$
Forward calorimeter		end-cap	
coverage		$3.1 < \|\eta\| < 4.9$	
longitudinal segmentation		3 samplings	
granularity ($\Delta\eta \times \Delta\phi$)		$\sim 0.2 \times 0.2$	

Table 3.4: Main parameters of the ATLAS calorimeters [68].

of $\sim 1\%$ for the $H \to \gamma\gamma$ and $H \to 4e$ channels in the mass region 90-180 GeV.

Hadronic calorimeter

The hadronic calorimeter can be divided in three components: the tile calorimeter in the central barrel and two extended barrels, the LAr hadronic end-cap (HEC) calorimeter and the LAr forward calorimeter (FCal), covering the range $|\eta| < 4.9$.

The tile calorimeter uses 3 mm thick plastic scintillator plates (tiles) as active material, embedded in a steel absorber. The orientation of the scintillator tiles radially and normal to the beam line allows for consistent azimuthal calorimeter coverage. Both sides of the scintillating tiles are readout by wavelength shifting fibbers and two separate photomultipliers (PMT). The 5.8 m long central barrel calorimeter covers the region $|\eta| < 1.0$, and the two 2.6 m long extended barrels cover $0.8 < |\eta| < 1.7$. Radially the calorimeter extends from an inner radius of 2.28 m to an outer radius of 4.23 m, segmented in three layers. Azimuthally, the barrel and extended barrels are divided into 64 modules. The resulting granularity of the calorimeter is $\Delta\eta \times \Delta\phi = 0.1 \times 0.1$ (0.2×0.1 on the last layer). The total active calorimeter (EM + tile) thickness is 9.2 interaction lengths at $\eta = 0$. The amount of material in front of the muon system, including the support structure of the tile calorimeter, is 11 interaction lengths at $\eta = 0$.

The hadronic LAr calorimetry covers the end-cap and forward region for $1.5 < |\eta| < 4.9$. The HEC is a copper/LAr sampling calorimeter with a flat-plate design, covering the end-cap region $1.5 < |\eta| < 3.2$. Each hadronic end-cap consists of two, equal diameter, independent wheels, located directly behind the end-cap EM calorimeter and sharing the same LAr cryostats. Each wheel is built from 32 identical wedge-shaped modules and divided into two longitudinal segments, for a total of four layers per end-cap. The first wheel, closest to the interaction point, is built out of 25 mm copper plates, while the second one uses 50 mm plates; in both wheels the LAr gap between consecutive copper plates is 8.5 mm, providing the active medium for this sampling calorimeter. Also integrated in the end-cap cryostat is the FCal, with the front face at ~ 5 m from the interaction point. It provides coverage over $3.1 < |\eta| < 4.9$. Due to the high level of radiation in the forward region, this is a very challenging detector, however the close vicinity and couplings between these systems result in a quite hermetic design, which minimizes energy losses in cracks and dead spaces in the transition region around $\eta = 3.1$. FCal is a high density detector consisting of three longitudinal sections: the first one made of copper, is optimized for EM measurements, while the other two, made of tungsten,

measure predominantly the energy of hadrons. In each of them the calorimeter consists of a metal matrix with regularly spaced longitudinal channels filled with the electrode structure (concentric rods and tubes) parallel to beam axis. The sensitive medium is LAr and fills the gap between the rods and tubes and the matrix.

3.3.4 Muon Detectors

The muon spectrometer is the outer most ATLAS sub-detector. It is designed to detect charged particles exiting the barrel and end-cap calorimeters. Due to the deflection of muon tracks in the presence of the toroidal magnetic field, muon tracks are identified and reconstructed, and their momenta is measured in the $|\eta| < 2.7$ range. Information from both the muon spectrometer and the inner detector can be matched to give combined muon tracks. The spectrometer is also designed to trigger on those particles in the region $\eta < 2.4$. The performance goal is a stand-alone p_T resolution of $\sim 10\%$ for 1 TeV tracks. Muon momenta down to a few GeV (~ 3 GeV, due to energy loss in the calorimeters) can be measured by the spectrometer alone [64].

In the barrel region, muon chambers are arranged in three cylindrical layers ('stations') around the beam axis; in the transition and end-cap regions, the chambers are installed vertically, also in three stations. Over most of the η range, Monitored Drift Tubes (MDTs) provide a precision measurement of the track coordinates in the principal bending direction of the magnetic field. At large η, and close to the interaction point, Cathode Strip Chambers (CSCs), with finer granularity, are used to cope with the demanding rate and background conditions, due to their higher rate capability and time resolution. The MDTs chambers consist of three to eight layers of drift tubes, operated at an absolute pressure of 3 bar. The mechanical isolation in the drift tubes of each sense wire from its neighbors guarantees a robust operation. The CSCs are multiwire proportional chambers with cathodes segmented into strips in orthogonal directions. This allows both coordinates to be measured from the induced-charge distribution. The resolution of a chamber is 40 μm in the $R - z$ plane and ~ 5 mm in the $R - \phi$ plane [64, 65, 69].

The precision-tracking chambers are complemented by a system of fast trigger chambers, covering a range of $|\eta| < 2.4$. Resistive Plate Chambers (RPCs) are used in the barrel, $|\eta| < 1.05$, and Thin Gap Chambers (TGCs) in the end-cap region, $1.05 < |\eta| < 2.4$. Both types of trigger chambers also provide a 'second coordinate' measurement of track coordinates orthogonal to the precision measurement, in approximately the phi direction. The trigger chambers provide not only well-defined p_T threshold, but also bunch-crossing (BC) identification. The RPC is a gaseous parallel electrode-plate detector providing a typical space-time

resolution of 1 cm×1 ns with digital readout. Each chamber is made from two detector layers, each one read out by two orthogonal strip panels. The 'η strips' are parallel to the MDT wires and provide the bending view of the trigger detector and the 'ϕ strips', orthogonal to the MDT wires, provide the second coordinate measurement. The TGCs are designed in a way similar to multiwire proportional chambers, with the difference that the wire-to-cathode distance is smaller than the wire-to-wire distance. Signals from the wires, arranged parallel to the MDT wires, provide the trigger information together with readout strips, arranged orthogonal to the wires. The readout strips also serve to measure the second coordinate [64, 65, 69].

Figure 3.3(d) shows the layout of the spectrometer and Table 3.5 lists the main parameters of the muon chambers.

Monitored drift tubes (MDT)	
coverage	$\|\eta\| < 2.7$ (inner most layer: $\|\eta\| < 2.9$)
number of chambers	1150
number of channels	354k
chamber resolution	35 μm (z)
function	precision tracking
Cathode strip chambers (CSC)	
coverage	$2.0 < \|\eta\| < 2.7$
number of chambers	32
number of channels	31k
chamber resolution	40 μm (R), 5 mm (ϕ), 7 ns (time)
function	precision tracking
Resistive Plate Chambers (RPC)	
coverage	$\|\eta\| < 1.05$
number of chambers	606
number of channels	373k
chamber resolution	10 mm (z), 10 mm (ϕ), 1.5 ns (time)
function	triggering, second coordinate
Thin gap chambers (TGC)	
coverage	$1.05 < \|\eta\| < 2.7$ (2.4 for triggering)
number of chambers	3588
number of channels	318k
chamber resolution	2-6 mm (R), 3-7 mm (ϕ), 4 ns (time)
function	triggering, second coordinate

Table 3.5: Main parameters of the muon spectrometer.

3.3.5 Luminosity Detectors

A set of smaller detectors are used to provide good coverage in the very forward region. In order of decreasing distance from the interaction point, the first system is a Cerenkov detector named LUCID (LUminosity measurement using Cerenkov Integrating Detector). Located at ± 17 m from the interaction point, it is specifically designed to measure the luminosity in ATLAS. It consists of sixteen optically reflecting aluminum tubes filled with C_4F_{10} gas surrounding the beampipe on each side of the interaction point. It detects inelastic *pp* scattering in the forward direction, in order to measure the integrated luminosity and to provide online monitoring of the instantaneous luminosity and beam conditions. The second system is the Zero-Degree Calorimeter (ZDC), located at a distance of ± 140 m from the interaction point. Its primary purpose is to detect forward neutrons and photons with $|\eta| > 8.3$ in both *pp* and heavy-ions collisions. It consists of two arms, each one with one EM and three hadronic calorimeter modules. A third detector, the Beam Conditions Monitor (BCM), consists of two arms of diamond sensors located at ± 184 cm and $r = 5.5$ cm to record the single-sided and coincidence rates as a function of Bunch Crossing Identifier (BCID). The detector's value as a luminosity monitors is further enhanced by its excellent timing (0.7 ns) which allows rejection of backgrounds from beam-halo, and also issues a beam-abort request in case beam losses start to risk damage to the ATLAS detectors. The ALFA (Absolute Luminosity For ATLAS) detector, consisting of scintillating-fiber trackers located inside Roman pots at approximately ± 240 m from the interaction point, can provide an absolute luminosity calibration at ATLAS through the measurement of elastic *pp* scattering at small angles. Lastly, the Minimum Bias Trigger Scintillators (MBTS), located at ± 365 cm from the collision point, are segmented scintillator counters, providing a trigger on minimum collision activity during a *pp* BC [64, 65, 70].

The main function of the LUCID and ALFA systems is to determine the luminosity delivered to ATLAS, whereas the ZDC plays a key role in determining the centrality of heavy-ion collisions. The ALFA detector uses the optical theorem, which connects the elastic scattering amplitude in the forward direction to the total cross-section, and can thus be used to extract luminosity. On the other hand, LUCID is based on the principle that the number of particles detected is proportional to the number of interactions in a BC. The number of interactions per beam-crossing is needed to determine the luminosity.

Luminosity measurement

Accurate determination of the luminosity is an essential ingredient for many different measurements performed by the LHC experiments. The luminosity of a *pp* collider can be expressed in terms of the rate of inelastic collisions, R_{inel}, and the *pp* inelastic cross-section, σ_{inel}:

$$\mathcal{L} = \frac{R_{\text{inel}}}{\sigma_{\text{inel}}} \tag{3.2}$$

which can be rewritten as:

$$\mathcal{L} = \frac{\mu n_b f_{\text{rev}}}{\sigma_{\text{inel}}} \tag{3.3}$$

with f_{rev} and n_b previously defined for Equation 3.1, and μ is the average number of inelastic interactions per BC. Thus, by measuring the ratio μ/σ_{inel}, the instantaneous luminosity can be determined. In order to asses and control systematic uncertainties in the measurement of the luminosity, not only several detectors are used, but also multiple algorithms or counting techniques. Each algorithm having different acceptance, response to pile-up and beam-induce backgrounds.

From Equation 3.3 it follows:

$$\mathcal{L} = \frac{\mu n_b f_{\text{rev}}}{\sigma_{\text{inel}}} = \frac{\mu_{\text{vis}} n_b f_{\text{rev}}}{\varepsilon \sigma_{\text{inel}}} = \frac{\mu_{\text{vis}} n_b f_{\text{rev}}}{\sigma_{\text{vis}}}, \tag{3.4}$$

where ε is the event-selection efficiency for one inelastic *pp* collision, and $\mu_{\text{vis}} \equiv \varepsilon\mu$ is the average number of *visible* inelastic interactions per BC (minimum number of *pp* collisions per BC passing the event selection). The visible cross section $\sigma_{\text{vis}} \equiv \varepsilon\sigma_{\text{inel}}$ is the calibration constant relating the experimentally observable quatity μ_{vis} to the luminosity $\mathcal{L}$. It is then possible to obtain the absolute luminosity calibration, from measured accelerator parameters, both for online monitoring and for offline analysis. The delivered luminosity can be written as:

$$\mathcal{L} = \frac{n_b f_{\text{rev}} n_1 n_2}{2\pi \Sigma_x \Sigma_y} \tag{3.5}$$

where n_1 and n_2 are the numbers of particles in the two colliding bunches and Σ_x and Σ_y characterize the widths of the horizontal and vertical beam profiles. The widths of the beam profile are measured using van der Meer (*vdM*) scans [71]. In this technique, the observed event rate is recorded while scanning the two beams across each other (first horizontally, then vertically), yielding two bell-shaped curves, with the maximum rate at zero separation, from which one extracts the values of Σ_x and Σ_y. Combining with an external

measurement of the bunch charge product $n_1 n_2$, the luminosity can be extracted from Equation 3.5. The σ_{vis} can be accordingly determined by comparing this peak luminosity to the peak interaction rate, $\mu_{\text{vis}}^{\text{MAX}}$, observed during the *vdM* scan when the beams are unseparated:

$$\sigma_{\text{vis}} = \mu_{\text{vis}}^{\text{MAX}} \frac{2\pi \Sigma_x \Sigma_y}{n_1 n_2}, \tag{3.6}$$

In the limit $\mu_{\text{vis}} \ll 1$, μ_{vis} is a linear function of the event rate, as μ_{vis} increases it must be calculated taking into account Poisson statistics, and in some cases, instrumental and pile-up effects.

Three different types of luminosity determination techniques can be listed:

Event counting: determining the fraction of BC where an "event" (for a given selection requirement) was registered by the detector.

Hit counting: counting number of hits per BC in a given detector.

Particle counting: assessing the distribution of the number of particles per beam crossing inferred from any observable that reflects the instantaneous particle flux transversing the detector.

For event counting algorithms there are two main types being used in ATLAS: inclusive (EventOR) and coincidence (EventAND) counting. More specifically ATLAS currently uses the following detectors and algorithms:

- LUCID_EventAND
- LUCID_EventOR
- BCM_EventOR
- MBTS_Timing (EventAND algorithm with a timing constraint)
- PrimVtx (number of events with a primary vertex containing at least four tracks with $p_T > 150$ MeV).

The last two are offline algorithms relying in the MBTS detector, and the vertexing capabilities of the inner detector, respectively.

In both inclusive and coincide counting types it is assumed that the efficiency to detect an inelastic pp interaction is constant, in the sense that it does not change when several interactions occur in the same BC. The relevant efficiencies for these two types are: ε^{A} and ε^{C}, for observing an event with, respectively, at

least one hit on the A-side, at least one hit on the C-side, and $\varepsilon^{\mathrm{OR}}$ and $\varepsilon^{\mathrm{AND}}$, for observing at least one hit on both sides simultaneously, at least one hit on either side, respectively. These efficiencies are related by $\varepsilon^{\mathrm{OR}} = \varepsilon^{\mathrm{A}} + \varepsilon^{\mathrm{C}} - \varepsilon^{\mathrm{AND}}$.

In an EventOR algorithm, a BC is counted if the sum of all hits on both the forward (A) and backward (C) arms of the detector being used is at least one. Since the Poisson probability of observing zero events in a given bunch is $P_0\left(\mu_{\mathrm{vis}}^{\mathrm{OR}}\right) = e^{-\mu\varepsilon^{\mathrm{OR}}} = e^{-\mu_{\mathrm{vis}}^{\mathrm{OR}}}$, then, the probability of observing an inclusive event can be computed as:

$$P_{\mathrm{Event\_OR}}\left(\mu_{\mathrm{vis}}^{\mathrm{OR}}\right) = 1 - e^{-\mu_{\mathrm{vis}}^{\mathrm{OR}}} = \frac{N_{\mathrm{OR}}}{N_{\mathrm{BC}}}. \tag{3.7}$$

Here N_{OR} is the number of BCs, in a given time interval, in which at least one pp interaction satisfies the event selection of the OR algorithm, and N_{BC} is the total number of BCs in the same interval. From Equation 3.7 $\mu_{\mathrm{vis}}^{\mathrm{OR}}$ can be solved in terms of the event counting rate:

$$\mu_{\mathrm{vis}}^{\mathrm{OR}} = -\ln\left(1 - \frac{N_{\mathrm{OR}}}{N_{\mathrm{BC}}}\right). \tag{3.8}$$

For the EventAND algorithm, a BC is counted if there is at least one hit in both sides of the detector. So, the probability of observing a coincidence event will be one minus the probability of there being no hit on at least one side. This being the probability that there be no hit on at least side A $\left(e^{-\mu\varepsilon^{\mathrm{A}}}\right)$, plus the probability that there be no hit on at least side C $\left(e^{-\mu\varepsilon^{\mathrm{C}}}\right)$, minus the probability that there be no hit on either side $\left(e^{-\mu\varepsilon^{\mathrm{OR}}}\right)$:

$$P_{\mathrm{Event\_AND}}\left(\mu_{\mathrm{vis}}^{\mathrm{AND}}\right) = 1 - \left(e^{\mu\varepsilon^{\mathrm{A}}} + e^{\mu\varepsilon^{\mathrm{C}}} - e^{\mu\varepsilon^{\mathrm{OR}}}\right) = 1 - \left(e^{\mu\varepsilon^{\mathrm{A}}} + e^{\mu\varepsilon^{\mathrm{C}}} - e^{\mu\left(\varepsilon^{\mathrm{A}}+\varepsilon^{\mathrm{C}}-\varepsilon^{\mathrm{AND}}\right)}\right) = \frac{N_{\mathrm{AND}}}{N_{\mathrm{BC}}} \tag{3.9}$$

For using such a coincidence algorithm in detectors like LUCID and BCM, the fact that $\varepsilon^{\mathrm{AND}} \ll \varepsilon^{\mathrm{A,C}}$ can be used, along with the assumption that $\varepsilon^{\mathrm{A}} \approx \varepsilon^{\mathrm{C}}$, to simplify Equation 3.9:

$$\begin{aligned} P_{\mathrm{Event\_AND}}\left(\mu_{\mathrm{vis}}^{\mathrm{AND}}\right) &= \frac{N_{\mathrm{AND}}}{N_{\mathrm{BC}}} \\ &= 1 - 2e^{-\mu\left(\varepsilon^{\mathrm{AND}}+\varepsilon^{\mathrm{OR}}\right)/2} + e^{\mu\varepsilon^{\mathrm{OR}}} \\ &= 1 - 2e^{-\left(1+\sigma_{\mathrm{vis}}^{\mathrm{OR}}/\sigma_{\mathrm{vis}}^{\mathrm{AND}}\right)\mu_{\mathrm{vis}}^{\mathrm{AND}}/2} + e^{-\left(\sigma_{\mathrm{vis}}^{\mathrm{OR}}/\sigma_{\mathrm{vis}}^{\mathrm{AND}}\right)\mu_{\mathrm{vis}}^{\mathrm{AND}}} \end{aligned} \tag{3.10}$$

where $\varepsilon^{\mathrm{OR}} = \frac{\sigma_{\mathrm{vis}}^{\mathrm{OR}}}{\sigma_{\mathrm{vis}}^{\mathrm{AND}}}\varepsilon^{\mathrm{AND}}$ has been used. This expression can not be inverted analytically to determine $\mu_{\mathrm{vis}}^{\mathrm{AND}}$. It can, however, be solved numerically. If the efficiency is high and $\varepsilon^{\mathrm{AND}} \approx \varepsilon^{\mathrm{A}} \approx \varepsilon^{\mathrm{C}}$ as in the case of coincide

average σ_{vis} [mb]						$\bar{\sigma}_{\text{vis}}$
Scan Number	I	II	III	IV	V	combined
LUCID_EventAND	11.92 ± 0.14	12.65 ± 0.10	12.83 ± 0.10	13.09 ± 0.01	13.06 ± 0.01	$13.04 \pm 0.01 \pm 0.44$
LUCID_EventOR	38.86 ± 0.32	41.03 ± 0.13	41.10 ± 0.14	41.84 ± 0.03	41.71 ± 0.02	$41.67 \pm 0.02 \pm 1.40$
BCM_EventOR	—	—	—	4.599 ± 0.007	4.590 ± 0.007	$4.594 \pm 0.005 \pm 0.147$
MBTS_Timing	48.32 ± 0.31	50.22 ± 0.20	49.92 ± 0.20	51.29 ± 0.24	51.23 ± 0.21	$51.13 \pm 0.15 \pm 1.71$
PrimVtx	46.63 ± 0.27	48.24 ± 0.21	48.36 ± 0.21	49.45 ± 0.23	49.37 ± 0.21	$49.28 \pm 0.14 \pm 1.65$

Table 3.6: BCID-averaged σ_{vis} for all algorithms used in ATLAS per *vdM* scans, and the best estimate for each algorithm from the combined data, $\bar{\sigma}_{\text{vis}}$. Errors on σ_{vis} per scan are statistical only, whereas errors on $\bar{\sigma}_{\text{vis}}$ are both statistical and systematic.

algorithms in the MBTS detector, Equation 3.9 can be approximated by assuming:

$$\mu_{\text{vis}}^{\text{AND}} \approx -\ln\left(1 - \frac{N_{\text{AND}}}{N_{\text{BC}}}\right) \tag{3.11}$$

Table 3.6 presents the measurement of BCID-averaged σ_{vis} and the best estimate of the visible cross section, $\bar{\sigma}_{\text{vis}}$, for each luminosiy method used in ATLAS. Due to the requirement of a trigger and the restrictions on the available trigger bandwidth, the relative uncertainty of the offline algorithms are worse than the LUCID or BCM data [70, 72].

For the LUCID_EventOR algorithm which is the preferred algorithm for ATLAS physics results the calibration of the visible cross section is found to be $\sigma_{\text{via}} = 41.67 \pm 1.40$ mb. The dominant systematic uncertainty on that number is due to the determination of the bunch charge product ($n_1 n_2$), which is conservatively estimated to have a systematic uncertainty of 10%. Other sources of systematic uncertainties include transverse correlations (correlation in the profile of the luminous region between the horizontal and vertical axes), emittance growth and μ dependance.

3.3.6 Trigger

Given the data storage and readout limitations, it is necessary to go from the initial BC rate of 40 MHz down to $\sim$ 300 Hz for permanent storage. The ATLAS trigger (organized in three levels) and data-acquisition system has been designed to accomplish this task with high efficiency.

The first-level (LVL1) trigger is implemented in hardware and uses a subset of the detector information to reduce the rate to at most 75 kHz. The LVL1 trigger makes an initial selection using reduced granularity information from a subset of detectors, and based on combinations of objects required in coincidence or veto. Hight p_T muons are identified using the trigger chambers, RPCs in the barrel, and TGCs in the end-

caps. The calorimeter selections are based on reduced granularity information from the ATLAS calorimeters. Information is available for a number of sets of p_T thresholds. The inputs to the calorimeter trigger system are analogue signals from trigger towers with a typical granularity of $\Delta\eta \times \Delta\phi = 0.1 \times 0.1$. Digital signal processing is applied to extract the E_T for calorimeter pulses and to assign it to the correct BC. In the subsequent processing a search for high p_T electrons/photons and hadrons/taus, and high E_T jets, using full granularity trigger-tower information, is performed. Each of the eight sets of thresholds available for the electron/photon trigger, can be programmed independently and consists of a threshold on the E_T of the cluster, an isolation threshold on the surrounding E_T in the EM calorimeter, and a "hadron-veto" threshold on the E_T in the associated hadron-calorimeter towers. For the jet trigger there are eight thresholds that can be programmed independently and to which the E_T in 'jet-windows' is compared. The jet-window size is also programmable. The muon triggers receives as input the pattern of hit strips in the RPC chambers, and wire groups in the case of the TGC detectors. The timing resolution is sufficiently good that the trigger can, with very high probability, identify the BC that contained the muon. The trigger searches for patterns of hits consistent with high p_T muons originating from the interaction region. The logic provides six independently programmable p_T thresholds. The muon trigger system is subdivided into a part specific of the RPC detectors, a part specific of the TGC detectors, and a part that combines information from the full system [73].

The LVL1 trigger is followed by two software-based trigger levels that together reduce the event rate to $\sim$ 300 Hz. The level-2 (LVL2) trigger makes use of "region of interest" information provided by the LVL1 trigger. This includes information on the position and p_T range of candidate objects, and energy sums. Unlike the LVL1 trigger, the LVL2 trigger has access to all of the event data, if necessary with the full precision and granularity. In the case of muon triggers, rejection power at LVL2 comes from sharpening the p_T threshold (using information from the precision chambers), and from applying isolation requirements (using calorimeter information). For isolated electrons, rejection power at LVL2 comes from using the full granularity calorimeter information and the inner detector. A localized, isolated (hadronic) calorimeter cluster with a matching high p_T track is required. For the jets, being the dominant high p_T process at the LHC, much less rejection power is possible. At the third trigger level, the event filter (EF), the full event data are used together with the latest available calibration and alignment information to make the final selection of events to be recorded for offline analysis [74].

Chapter 4

Monte Carlo Simulation Samples

4.1 Introduction

Event generation consists of the production of a set of particles which is passed to detector simulation. Each generated event contains the particles from a single interaction with a vertex located at the geometrical origin. Several modifications, to account for the beam properties, are applied to the event before it is passed to simulation. Particles with a life time $c\tau > 10$ mm are considered stable by the generator, since they can propagate far enough to interact with the detector material before decaying. Their decays are then handled by the simulation. Generators produce complete events starting from proton-proton, proton-nucleus or nucleus-nucleus initial states [75].

Several physics aspects must be considered by an event generator in the description of a typical high-energy process. In colliders, like the LHC, two beams particles come in towards each other. Each particle can be characterized by a set of parton distributions, defining the partonic substructure in terms of flavor composition and energy sharing. The initial-state shower is built up by one parton from each beam, which initiates one shower starting off a sequence of branchings (such as $q \rightarrow qg$). Then, one incoming parton from each of the two showers enters the hard process. Here, a number of outgoing partons are produced. The nature of the hard process determines the main characteristics of the event. The hard process may produce a set of short-lived resonances (like W/Z-bosons) whose decay into normal partons has to be considered in close association with the hard process itself. The outgoing partons may radiate or decay building up final-state showers. Further semi-hard interactions can occur between the other partons of the two incoming hadrons. Many of the produced hadrons are unstable and decay. When a shower-initiator parton is taken out of a beam, a beam remnant is left behind. This beam remnant may have an internal structure and a net color charge that relates it to the rest of the final state, forming part of the same fragmentation system. These additional hard or soft scattering processes comprise the underlying event. It must also be taken into account that QCD confinement mechanism ensures that the outgoing quarks and gluons are not observable,

but instead fragment to color neutral hadrons [76].

Hard Processes

There are many different possible hard processes. They can be classified according to the number of final-state objects. The more particles in the final-state, the more complicated phase space. Similarly, they can be classified according to the physics scenario:

- Hard QCD processes (e.g. $qg \to qg$).
- Soft QCD processes (e.g. diffractive and elastic scattering).
- Heavy flavor production (e.g. $gg \to t\bar{t}$).
- Prompt-photon production (e.g. $qg \to q\gamma$) and photon-induced processes (e.g. $\gamma g \to q\bar{q}$).
- Vector boson production (e.g. $q\bar{q} \to W^+W^-$).
- SM Higgs production (if Higgs is reasonably light and narrow, it can still be considered a resonance).
- Some BSM scenarios (e.g. SUSY, production of new gauge bosons, non standard Higgs production, leptonquark production).

The list above is not exhaustive.

Parton Distributions

The cross section for a processes $ij \to k$ is given by:

$$\sigma_{ij\to k} = \int \mathrm{d}x_1 \int \mathrm{d}x_2 f_i^1(x_1) f_j^2(x_2) \hat{\sigma}_{ij\to k}. \tag{4.1}$$

Here $\hat{\sigma}_{ij\to k}$ is the cross section for the hard partonic process. $f_i^a(x)$ are the parton-distribution functions (PDF), which describe the probability to find a parton i inside beam particle a, with parton i carrying a fraction x of the total a momentum. Parton distributions also depend on some momentum scale, q^2, that characterizes the hard process. Since a derivation of hadron PDFs from first principles does not yet exist, it is necessary to rely on parameterizations, where experimental data are used in conjunction with the

evolution equations for the q^2 dependance. The composite structure of hadrons allow for multiple parton-parton scatterings to occur, in which case correlated parton distributions should be used to describe the multi-parton structure of the incoming beam.

Initial- and Final-State Radiation

In every process that contains colored and/or charged objects in the initial or final state, gluon and/or photon radiation may give large corrections to the overall topology of events. As the collision energy increases, hard emission of this kind becomes more important, relative to fragmentation, in determining the event structure. Two approaches are used to model the perturbative corrections. One is the matrix-element method, in which Feynman diagrams are calculated, order by order. This is, in principle, the correct approach, since it takes into account exact kinematics, and the full interference and helicity structure. However, these calculations are increasingly difficult in higher orders, in particular for loop graphs. The second possible approach is the parton-shower one. Here an arbitrary number of branchings of one parton into two, or more, may be combined, to yield a description of multijet events, with no explicit upper limit on the number of partons involved. Approximations derived by simplifying the kinematics, and the interference and helicity structure, are used.

Hadronization

QCD perturbation theory, formulated in terms of quarks and gluons, is valid at short distance. At long distances, QCD becomes increasingly interactive, breaking down perturbation theory. In this confinement regime, the colored partons are transformed into colorless hadrons, a process called hadronization or fragmentation. The tight cone of particles created by the hadronization of a single quark is called a jet. The hadronization process can not be derived from first principles, therefore different phenomenological models are used to implement it in the MC. All current models are of a probabilistic and iterative nature. For the description of soft scattering, parton shower modeling provides a relatively good description of collision physics, but not as good for hard scattering events. In such case, higher-order perturbative calculations of the hard scattering matrix element are needed. There are two main approaches for this: CKKM scheme and the MLM scheme [89]. In both cases different jet multiplicities from matrix elements are combined, without double counting with the parton shower emission.

Decays

A large fraction of the particles produced by fragmentation are unstable and they subsequently decay into the observable stable ones. Generators must then include all particles with their proper mean mass, width and decay properties. Normally it may be assumed that the decay products are distributed according to phase space. However in some cases additional requirements are necessary. For instance, particles may also be produced polarized and impart a non-isotropic distribution to their decay products.

Simulated Monte Carlo (MC) samples required for the analysis of data collected during 2011 were generated to model both FCNC signal events and certain backgrounds. Alternative MC samples were also generated to evaluate various systematic uncertainties. All MC samples are processed with the `GEANT4` [77] simulation of the ATLAS detector [75] and are reconstructed with the same algorithms used for the data.

4.2 Signal

MC simulation samples of top quark pair production, with one of the top quarks decaying through FCNC to Zq while the other decays according to the SM preferred mode, Wb, were generated with `TopRex` [78]. The FCNC top quark decay is expressed in terms of the anomalous couplings to the Z-boson through the expression [44]:

$$\Gamma(t \to qZ)_\gamma = \left(|v_{tq}^Z|^2 + |a_{tq}^Z|^2\right) \alpha m_t^3 \frac{1}{4m_Z^2 \sin^2 2\theta_W} \cdot \left(1 - \frac{m_Z^2}{m_t^2}\right)^2 \left(1 + 2\frac{m_Z^2}{m_t^2}\right) \text{ and} \tag{4.2}$$

$$\Gamma(t \to qZ)_\sigma = \left(\frac{\kappa_{tq}^Z}{\Lambda}\right)^2 \alpha\, m_t^3 \frac{1}{\sin^2 2\theta_W} \cdot \left(1 - \frac{m_Z^2}{m_t^2}\right)^2 \left(2 + \frac{m_Z^2}{m_t^2}\right), \tag{4.3}$$

where Λ is an energy scale [1]. The anomalous couplings were set to $\kappa_{tq}^Z = 0.1$, with $\Lambda = 1$ TeV. Only decays of the W- and Z-bosons involving charged leptons were generated ($Z \to ee, \mu\mu, \tau\tau$ and $W \to e\nu, \mu\nu, \tau\nu$). It was checked at parton level that changing the coupling values did not significantly change the signal kinematics [2]. This is important because it implies that the sensitivity of this analysis does not depend on the coupling values, given that in a counting experiment, such as this one, the results depends only the final signal acceptance. Table 4.1 shows the FCNC widths and BR obtained for several coupling values as

[1] The couplings are constants corresponding to the first expansion in momenta. The Γ_γ width is related to the γ_μ couplings that vanish at tree level by the GIM mechanism, and the Γ_σ width is related to the non-renormalizable $\sigma_{\mu\nu}$ terms that do not appear in the SM Lagrangian.

[2] This holds even when large values of κ are used. In the case of large κ, the only visible effect is on the top quark width, simply because larger κ translates into larger branching rations, therefore larger partial widths.

κ	f	FCNC partial width (GeV)	FCNC BR	total width (GeV)
0.6	0.71	9.8×10^{-1}	3.98×10^{-1}	2.46
0.3	0.71	2.5×10^{-1}	1.42×10^{-1}	1.72
0.1	0.71	2.7×10^{-2}	1.81×10^{-2}	1.50
0.1	0	2.7×10^{-2}	1.81×10^{-2}	1.50
0.1	1	2.7×10^{-2}	1.81×10^{-2}	1.50
0.01	0.71	2.7×10^{-4}	1.84×10^{-4}	1.48
0.001	0.71	2.7×10^{-6}	1.84×10^{-6}	1.48

Table 4.1: FCNC widths and BR obtained for several coupling values as reported by `TopReX` for $t\bar{t} \to bWqZ$.

reported by `TopRex`. Relevant kinematical distributions obtained with these coupling values are shown in Figure 4.1.

The `MRST2007 LO*` [79] PDF set was used with the `TopRex` generator. All signal events were hadronized with `PYTHIA 6.421` [76]. The masses of the top quark, W-boson and Z-boson were set to 172.5 GeV, 80.4 GeV and 91.2 GeV, respectively.

To study the effect of the uncertainty due to the uncertainty on the top quark mass, samples with top quark masses of 170 GeV and 175 GeV were also generated. The uncertainty due to initial- and final-state radiation (ISR/FSR) was evaluated using the `AcerMC` generator [80] interfaced with `PYTHIA`, and by varying parameters controlling ISR and FSR in a range consistent with those used in the Perugia Hard/Soft tune variations [81] and with experimental data [82].

4.3 Background

MC simulation samples were also generated for those SM processes with final-state topologies similar to the signal. As it will be explained in Chapter 6 these processes include events with three final state charged leptons, events with two final state charged leptons and at least one jet being misidentified as a lepton and events with four leptons in which one is not reconstructed.

Diboson events (WW, WZ and ZZ) were produced using `ALPGEN 2.13` [83]. The `CTEQ6L1` [84] PDF was used, and up to three additional partons from the matrix element were simulated. The parton shower and the underlying event were added using `HERWIG v6.510` [85, 86] and the `JIMMY` [87] underlying event model with the `AUET1` tune [88] to the ATLAS data.

The ALGPEN program with HERWIG showering and the JIMMY underlying event model with the AUET1 tune was also used to generate single vector boson + jets. MLM matching [89] was applied inclusively for the W+five partons production and exclusively for the lower multiplicities sub-samples [3]. The additional partons produced in the matrix element part of the event generation can be either light partons (W+jets and Z/γ+jets) or heavy quarks (W+c+jets, W+$c\bar{c}$+jets, W+$b\bar{b}$+jets, Z+$c\bar{c}$+jets and Z+$b\bar{b}$+jets). The inclusive W and Z/γ production samples were obtained from the full set of the parton multiplicity sub-samples belonging to the same production process including both extra jets and the heavy quark plus jets processes.

The $t\bar{t}$ and single-top events were generated using the MC@NLO generator v3.41 [90–92] with the CTEQ6.6 [93] PDFs. The parton shower and the underlying event were added using HERWIG v6.510 and JIMMY generators as described above. The $t\bar{t}$ production cross section was normalized to the approximate next-to-next-to-leading-order (NNLO) prediction of 164.6 pb, obtained using the HATHOR tool [94]. The cross sections for single-top production were normalized to the approximate NNLO predictions of 64.6 pb [95], 4.6 pb [96] and 15.7 pb [97] for t-channel, s-channel and associate Wt production, respectively.

Events with $t\bar{t}$+W and $t\bar{t}$+Z production, including those with extra jets in the final state, were generated using MADGRAPH 4.4.62 [98]. Parton showering was added using PYTHIA.

All decay modes of the W- and Z-bosons to charged leptons were considered in the generation and simulation of the background samples used.

4.4 Pile-up Correction

The MC samples used in the analysis include the simulation of additional pp interactions in the same BC as the event in hand. This effect, in-time pile-up, is simulated by adding minimum bias events to the main simulated process. Out-of-time pile-up, the effect of collisions in neighboring BCs, is also considered. A single pile-up configuration corresponding to the LHC running with 50 ns bunch separation is used. For the case of in-time pileup, PYTHIA6 minimum bias events are used and variable pile-up rates are assumed. The number of minimum bias events added to each simulated event is chosen according to a Poisson distribution with average of number of interactions, $\langle\mu\rangle$. In MC $\langle\mu\rangle$ is varied from 0 o 18 to describe the various conditions

[3] Inclusively in this case means that all the resulting samples from $n = 0, \ldots, N$ partons are combined.

of LHC luminosity. In the collision data, $\langle\mu\rangle$ is estimated for each luminosity block:

$$\langle\mu\rangle = \frac{\mathcal{L}_{\text{inst}} \times \sigma_{\text{total}}}{n_{\text{bunches}} \times f_{\text{rev}}}, \tag{4.4}$$

where $\mathcal{L}_{\text{inst}}$ is the instantaneous luminosity measured in the luminosity block, n_{bunches} is the number of colliding bunches, f_{rev} is the revolution frequency and $\sigma_{\text{total}} = 71.5$ mb^{-1} is the total inelastic cross section. The $\langle\mu\rangle$ distribution for the 2.1 fb^{-1} of data and MC is shown in Figure 4.2. The simulated events are weighted such that $\langle\mu\rangle$ for MC matches the distribution in the data.

4.5 Scale Factors

Data-to-MC scale factors, $\varepsilon_{\text{data}}/\varepsilon_{\text{MC}}$, are applied to the MC samples to account for small differences in efficiencies between data and MC simulation. The efficiencies considered are: trigger, identification, reconstruction and heavy-flavor tagging. Similarly, the energy scale and resolution for the different reconstructed objects, in the kinematic range of interest for top events, are derived from data. This will be explained in more detail in Section 5.3.

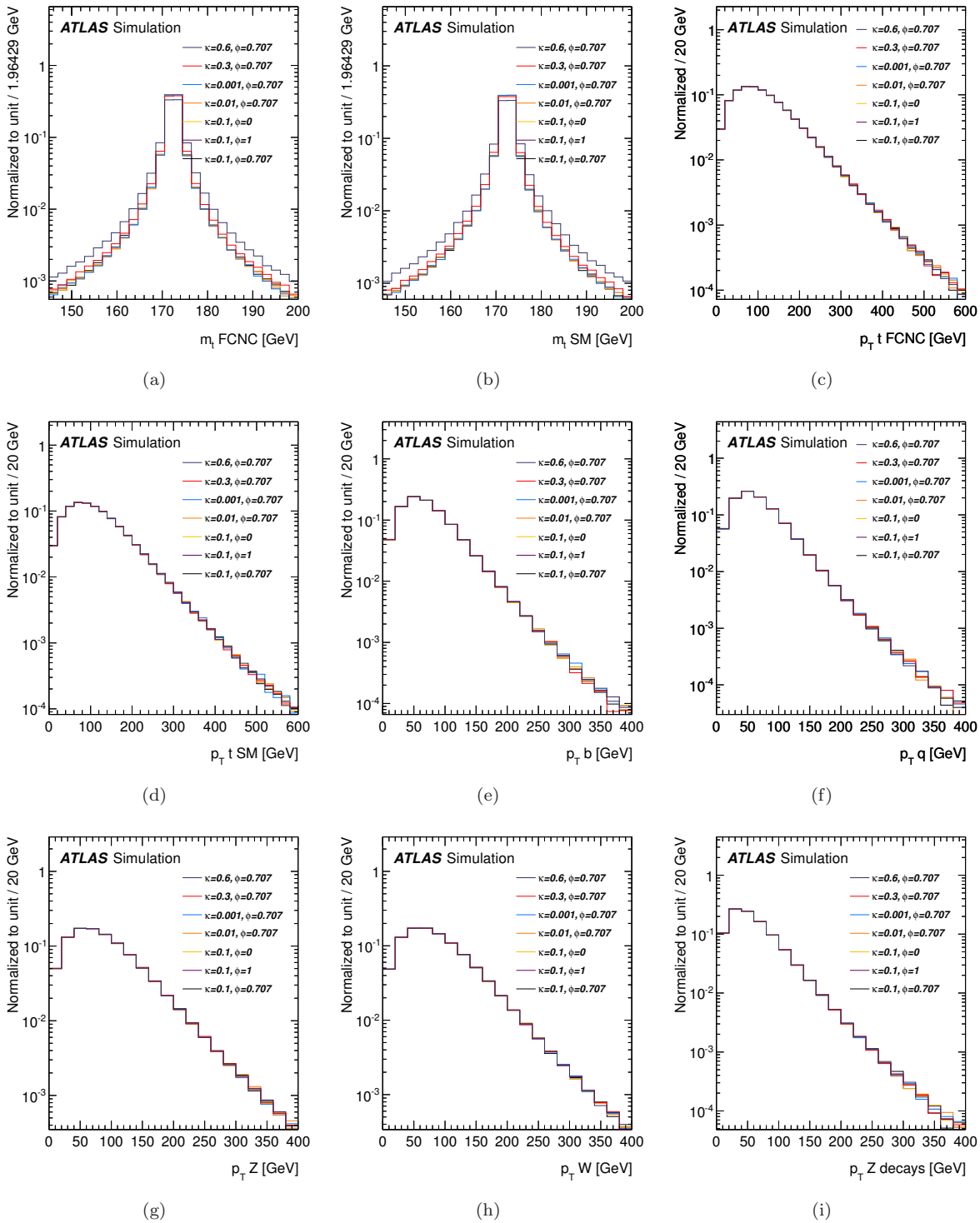

Figure 4.1: Some relevant kinematic quantities for different TopRex coupling values for the $t \rightarrow qZ$ channel: mass of the top quark (a) with FCNC decay and (b) with SM decay; transverse momenta distributions of (c) the FCNC decaying top quark, (d) the SM decaying top quark, (e) the b-quark from SM decaying top quark, (f) the quark and the (g) Z from the FCNC decaying top quark, (h) the W boson from the SM decaying top quark and i) the decay products of the Z boson.

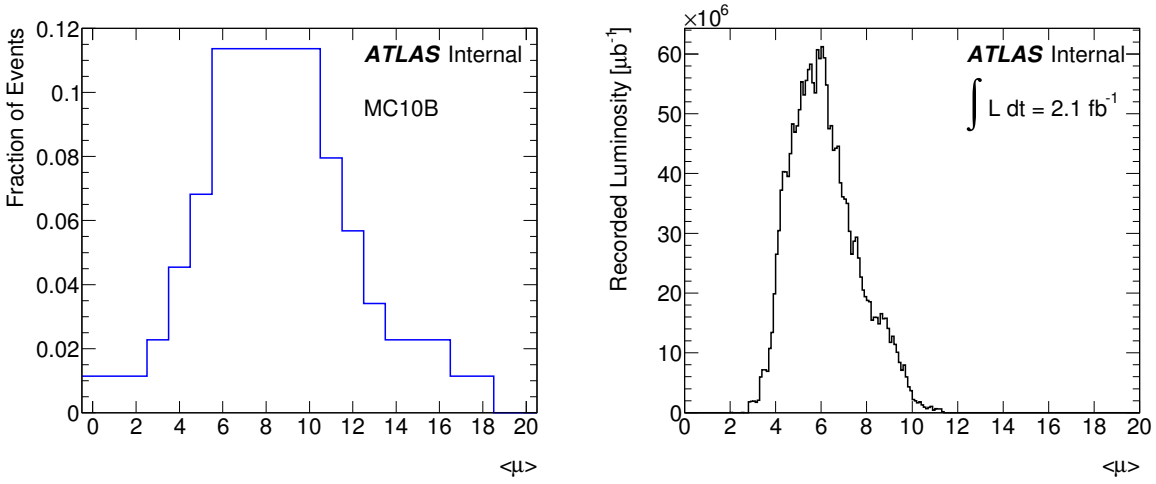

(a) (b)

Figure 4.2: Average number of interactions per bunch crossing distributions in (a) MC and in (b) data. The MC is weighted to match this $\langle\mu\rangle$ distribution between data and MC. The average number of interactions assumed when the MC was generated is larger than the number seen in the collision data.

Chapter 5

Event Selection

5.1 Introduction

The search for FCNC in top quark decays is done in $t\bar{t}$ pairs, with one top quark decaying through FCNC ($t \to Zq$) and the other through the SM dominant mode ($t \to Wb$). The final state topology is then defined by the decay of the W- and Z-bosons. Even though hadronic decays have larger branching fractions, hadronic final states are rather difficult to isolate from background due to large multijet background in hadron colliders. Hence, this analysis is limited to the decay channels in which the Z-boson decays into a pair of opposite charge leptons, and the W-boson decays to one lepton and its corresponding neutrino, namely: $Z \to l_i^+ l_i^-$, and $W^\pm \to l_j^\pm \nu$, where i and j can be any of the lepton types, and are not necessarily different. Thus the final state is characterized by three isolated leptons, two of them reconstructing the Z-boson, large missing transverse energy, E_T^{miss} (from the undetectable neutrino from the W-boson decay), and at least two jets (one of them a b-jet). The final state topology is illustrated in Figure 5.1.

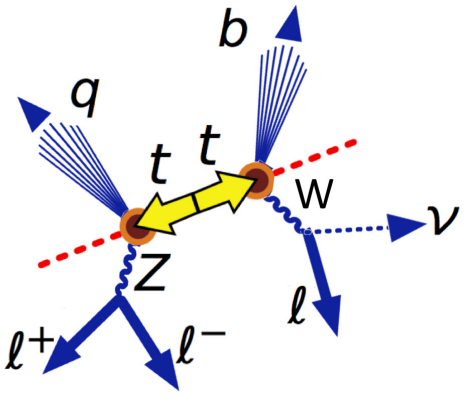

Figure 5.1: Final state signature.

5.2 Trigger

This analysis requires collision data selected by inclusive single electron and muon triggers, with p_T thresholds of 18 GeV for muons and 20 or 22 GeV for electrons, depending on the data taking period. Specifically, the lowest unprescaled trigger chains are used. To ensure that the event is triggered by the lepton candidates selected by the analysis (see Section 5.3), one of the leptons and the trigger object are required to match within $\Delta R < 0.15$.

5.3 Object Definition

After the offline reconstruction, additional requirements are applied to the reconstructed objects. Moreover, to increase the acceptance of the analysis, leptons are also selected based purely on the inner detector track information. Thus, leptons are selected either using the full ATLAS detector, including the inner detector, calorimeter and muons spectrometer ('identified leptons' or 'ID leptons'), or using only a high quality inner detector track ('track leptons' or 'TLs'). These TLs recover areas of inefficiency in the standard lepton identification algorithms and also have sensitivity to hadronic tau decays.

5.3.1 Muons

Muons are detected and measured in the muon spectrometer, which is instrumented with separate trigger and high-precision tracking chambers. Muon momentum is measured via the curvature of the trajectory in the toroidal magnetic field on the spectrometer and the solenoidal field of the inner detector. In the case of muon, tracks from both the muon spectrometer and the inner detector are matched to give combined tracks. Only muons passing tight track quality requirements are considered. Muon candidates are required to have a transverse momenta larger than 20 GeV. Due to the geometrical constraints of the inner detector fiducial region, muons must have $|\eta| < 2.5$. Both calorimeter- and track-based isolation requirements are applied to the muons, to select candidates consistent with originating from W- and Z-bosons decay. The track-based isolation, defined as the sum of transverse momenta of tracks with $p_T > 1$ GeV, inside a cone of size $\Delta R = 0.3$ around the muon, must be less than 4 GeV. Similarly, the energy deposited in the calorimeter inside a cone of size $\Delta R = 0.3$ around the muon (ignoring the energy of the muon), i.e. calorimeter isolation, must be less than 4 GeV. Additionally, to further reject muons from heavy flavor decays, muon candidates must have a distance $\Delta R > 0.4$ from any jet with $p_T > 20$ GeV. Muons arising from cosmic

Variable	Cut
p_T	>20 GeV
Type	MuID tight
Calorimeter Isolation, $\Delta R < 0.3$	<4 GeV
Track Isolation, $\Delta R < 0.3$	<4 GeV
Fiducial	$\|\eta\| < 2.5$
$\|d_0\|$	<0.5 mm
Hit requirements	b-layer hits ≥ 0
	pixel hits ≥ 2
	SCT hits ≥ 6
	if $\|\eta\| < 1.9$, TRT hits ≥ 6

Table 5.1: Muon selection requirements.

rays are rejected by removing candidate pairs that are back-to-back in the $r - \phi$ plane and with transverse impact parameters relative to the beam axis $|d_0| > 0.5$ mm. Finally, a standard set of hit requirements are imposed: at least one hit in the inner most pixel layer (b-layer), except in regions where no b-layer is present, at least two pixel hits, at least 6 SCT hits, and an η-dependent TRT hits requirement (to take into account the limited TRT coverage). Due to an issue related to the trigger simulation in MC samples, events with a muon with $p_T > 150$ GeV are not considered in the analysis. The muon selection is summarized in Table 5.1.

Scale Factors

Muon reconstruction scale factor are measured as a function of muon η to correct the efficiency in the MC to that in the data. They are consistent with unity throughout the η range. Both trigger and identification efficiencies for the selection given above are measured for already formed combined muon tracks. The trigger efficiency is measured for the trigger chain used in this analysis, with threshold at 18 GeV, in $Z \rightarrow \mu\mu$ events selected in data and MC, as a function of η, ϕ and p_T. The technique used to measure this single object trigger efficiency is denoted "tag&probe". Here, the tag-muon is an ID muon, whereas the probe-muon is selected with a subset of the ID muon criteria ('loose muon'). Events with a tag&probe pair with invariant mass inside a window around the $m_Z = 91.2$ GeV are selected. This sample makes the denominator of the efficiency. The numerator consists of those loose muons passing the ID muon selection too. The data and MC efficiencies are shown in Figure 5.2 as a function of those variables. As seen there, a dependence of the scale factor on the muon p_T is observed in the barrel, but not in the end-caps. This, however, is only consequence of an extrapolation error affecting combined muon triggers in this region. This error was not present in data, and it affects mostly high p_T muons. Given that the p_T range of muons from Z-boson

decays is limited due to limited number of MC events available, the behavior of the simulated efficiency after $\approx$ 150 GeV can not be studied. Because of this, events with muons with $p_T > 150$ GeV are vetoed. The trigger efficiencies are provided as a function of η and ϕ, and separated into three p_T bins, [20-60 GeV], [60-120 GeV], and $>$ 120 GeV.

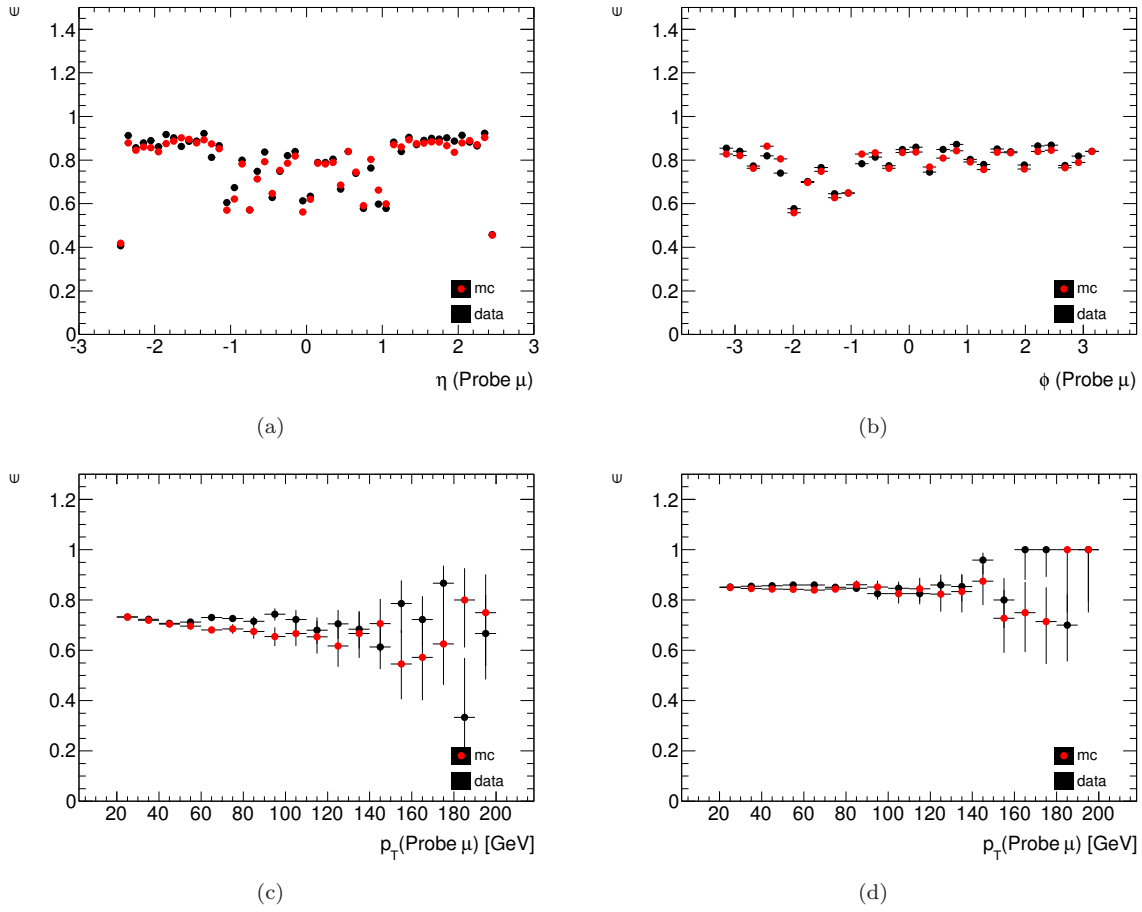

Figure 5.2: Comparison of trigger efficiency for data (black) and MC (red) as a function of (a)η, (b)ϕ and p_T of muons in the (c) barrel and (d) end-caps.

The muon identification efficiency is also extracted from a fit to the invariant mass of $Z \rightarrow \mu\mu$ events. No dependence is observed on the isolation cuts. These scale factors are constant for all muons and measured in two periods of data taking. The muon identification efficiency measured in the first 0.7 fb^{-1} of data are shown in Figure 5.3.

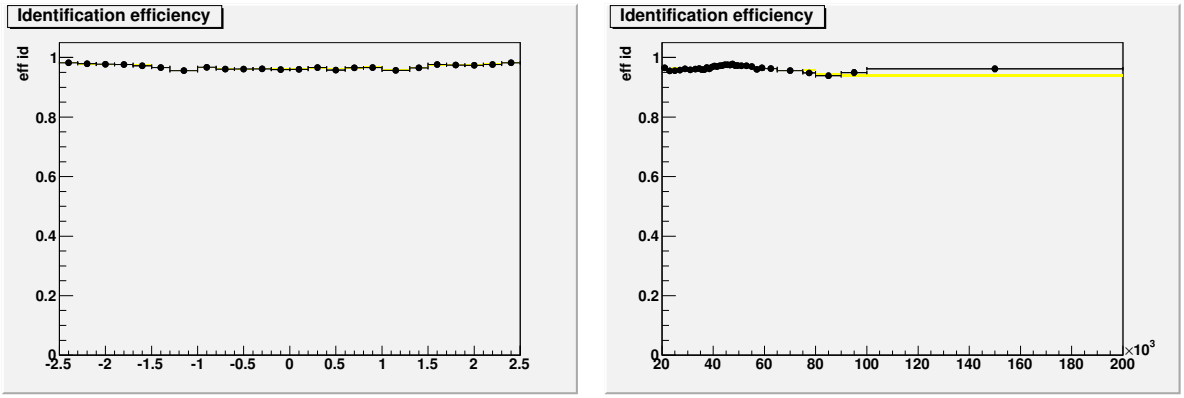

(a) (b)

Figure 5.3: Muon identification efficiency for data (black dots) and MC (yellow rectangles), as a function of (a) $\eta(\mu)$ and (b) $p_T(\mu)$. The data uses 0.7 fb^{-1} of 2011 collision data. The MC includes all background contributions.

Momentum Scale and Resolution

At the same time, the scale and resolution of the muon momentum distributions are corrected on MC, to match those observed in data. This is done for the inner detector and the muon spectrometer tracks used in the muon combined track separately. This correction is done before the selection of muons.

5.3.2 Electrons

Electron candidates are found as clusters in the EM calorimeter, with a matching track in the inner detector. Additional cuts on shower shapes (lateral and longitudinal shower profiles) and on information from the reconstructed track are applied to further reject fake electrons (e.g. photons). Stringent quality requirements on conditions of the EM calorimeter at the time of the data taking are applied to ensure a well measured energy. A *tight* selection using calorimeter, tracking and combined variables is used to provide good separation between signal electrons and background. As for muons, electrons are required to have high transverse momentum and be isolated in order to suppress backgrounds from misidentified jets. Electron candidates are required to have $E_T > 20$ GeV where E_T is constructed as $E_T = E_{\text{cluster}}/\cosh(\eta_{\text{track}})$, meaning from the calorimeter cluster energy E_{cluster} and the direction of the electron track, η_{track}. The isolation requirement is calorimeter-based only: the transverse energy deposited in the calorimeter not associated to the electron is summed in a cone of radius $\Delta R = 0.2$ around the electron and is required to be less than 3.5 GeV[1]. To

[1] the calorimeter isolation of electrons is corrected for additional energy deposit from pile-up events and energy leakage into the isolation cone.

Variable	Cut
E_T	>20 GeV
Type	Electron tight
Calorimeter Isolation, $\Delta R < 0.2$	<3.5 GeV
Fiducial	$\lvert\eta\rvert < 2.47$
	$1.37 < \lvert\eta\rvert < 1.52$ excluded

Table 5.2: Electron selection requirements.

avoid regions of low efficiency in the EM calorimeter, only candidates with $|\eta_{\text{cluster}}| < 2.47$, excluding the crack region $1.37 < |\eta_{\text{cluster}}| < 1.52$, are selected. The electron selection is summarized in Table 5.2. Note that, to ensure events are triggered with high efficiency, in the data periods with higher electron trigger thresholds, trigger objects that are electrons are required to have $E_T > 25$ GeV.

Scale Factors

For those electrons passing the selection given above, the trigger efficiency is measured in both data and MC. Then, a scale factor to account for any difference between data and MC efficiencies in trigger matching is used. The efficiency of the trigger ($\varepsilon_{\text{trig}}$) and the data-to-MC efficiency ratio is measured using the tag&probe method in $Z \to ee$ events. This is, using the probe leg in $Z \to ee$ events in 18 bins of $|\eta|$ (cluster position) and is found to be in the plateau for ($E_T > 25$ GeV), with $\varepsilon_{\text{trig}} \simeq 98\%$ and $\text{SF}_{\text{trig}}(\eta) = \varepsilon_{\text{trig}}^{\text{data}}/\varepsilon_{\text{trig}}^{\text{MC}}$ within 2% from unity for all but the very forward ($|\eta| > 2$) regions. $W \to e\nu$ events were also used in this efficiency study.

In the case of electron identification and reconstruction, the MC is generally seen to model the data well, with a few exceptions mainly regarding the lateral development of showers and the TRT in the end-caps. Scale factors are derived to parameterize the different efficiency between data and MC. The electron reconstruction efficiency, including track quality cuts, is measured in three $|\eta|$ regions and the scale factor is found to be consistent with unity, except for $|\eta| > 2.37$, where it is $\simeq 0.97$. The electron identification efficiencies and scale factors are measured in 18 η bins (plus two for the calorimeter gap) and six E_T bins. When measuring versus one variable the SF is integrated over the other, so that η and E_T are treated as uncorrelated. Figure 5.4 shows the identification scale factors as a function of the electron η and E_T.

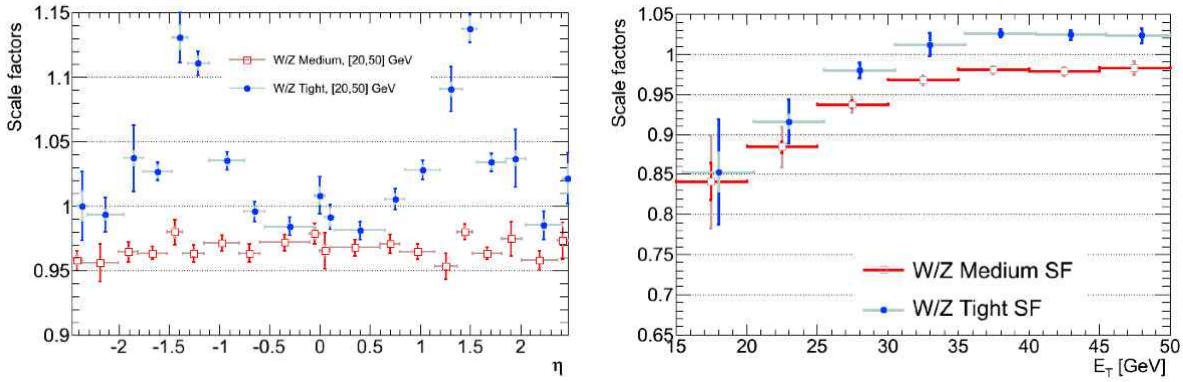

(a) (b)

Figure 5.4: Electron identification scale factors (a) versus η (with E_T between 20 and 50 GeV) and (b) versus E_T (for all η). The blue points, corresponding to the 'tight' selection are the relevant for this analysis.

Energy Scale and Resolution

Measurements of the electron energy scale and resolution, in a kinematic range comparable to that of electrons from top decays, are derived using a Z-boson mass of 91.19 GeV. The energy scale is corrected in data as a function of the electron η_{cluster}, ϕ_{cluster} and E_T. Similarly, energy smearing is applied to the electrons in MC to match the energy resolution in data. This correction is done before the selection of electrons.

5.3.3 Track-Leptons

Charged particles tracks are reconstructed, and their momenta measured, in the inner detector and the solenoid field. TL candidate selection comprises a series of cuts optimized for high efficiency and low fake rate. The transverse momenta of these tracks is required to be larger than 25 GeV. The higher p_T threshold partially compensates for the larger fake rate of TLs with respect to ID leptons. The candidates must also have at least six pixel + SCT hits and at least one hit in the b-layer. As for muons, this requirement is imposed only in regions where a b-layer hit is expected. They also must have $|d_0| < 0.2$ mm and the uncertainty on the q/p measurement must be less than 20%. The isolation requirement for TL candidates is track-based only: the sum of p_T of tracks inside a cone of $\Delta R = 0.3$ must be less than 2 GeV. In this case only tracks with $p_T > 1$ GeV and at least one pixel or SCT hit are used. The TL selection is summarized in Table 5.3. In order to ensure full orthogonality between TL candidates and ID lepton candidates, TLs within $\Delta R < 0.05$ of any ID lepton candidates are removed. TLs surviving this overlap removal are referred to as 'exclusive TLs'.

Variable	Cut
p_T	>25 GeV
Track Isolation, $\Delta R < 0.3$	<2 GeV
Number of pixel+SCT hits	>6
Number of b-layer hits	>0
$\lvert d_0 \rvert$	<0.2 mm
$\sigma(q/p)/(q/p)$	<0.2
Track comes from PV with $\geq$5 tracks	

Table 5.3: TL selection requirements.

Scale Factors

As it is done for electrons and muons, data-to-MC identification and reconstruction scale factors are measured for TLs in $Z \to ee$ and $Z \to \mu\mu$. In this case an ID lepton, electron or muon, is used as the tag leg, while the other is defined using either only calorimeter information, in the case of $Z \to ee$, or only muon spectrometer information, in the case of $Z \to \mu\mu$. The positive or negative leg is randomly chosen. The efficiency was measured in 0.7 fb^{-1} of data, a subset of the full data set used in the analysis. The efficiency measurement in data and MC for $Z \to \mu\mu$ events is shown in Figure 5.5 as a function of p_T, number of good primary vertices, η and ϕ. Where a 'good primary vertex' is one with more than four tracks ($p_T > 400$ MeV) associated to it. The integrated scale factor is found to be 0.997 ± 0.002. Figure 5.6 shows the same plots for $Z \to ee$ events. In this case, the integrated scale factor is measured to be 1.047 ± 0.005. The decrease of efficiency with increasing number of primary vertices, observed both in data and MC, is due to the failure of the isolation requirement in events with large number of tracks from pile-up interactions. Because it is well modeled in MC, the scale factors have little or no dependence on the number of primary vertices. In the case where the TL in MC is a hadron (rather than an electron or a muon), the scale factor derived from $Z \to \mu\mu$ events is used, because the main difference in the inner detector is the amount of bremsstrahlung radiation vs. ionization, and in this respect hadrons in the inner detector behave more similarly to muons.

5.3.4 Jets

The very high lateral granularity and the several samplings in depth of the ATLAS calorimeters allow efficient jet reconstruction over $|\eta| < 3.2$. Additionally, the forward calorimeters cover a region of $3.2 < |\eta| < 4.9$ and have sufficient granularity so that jets with small polar angles can be reconstructed with reasonable accuracy.

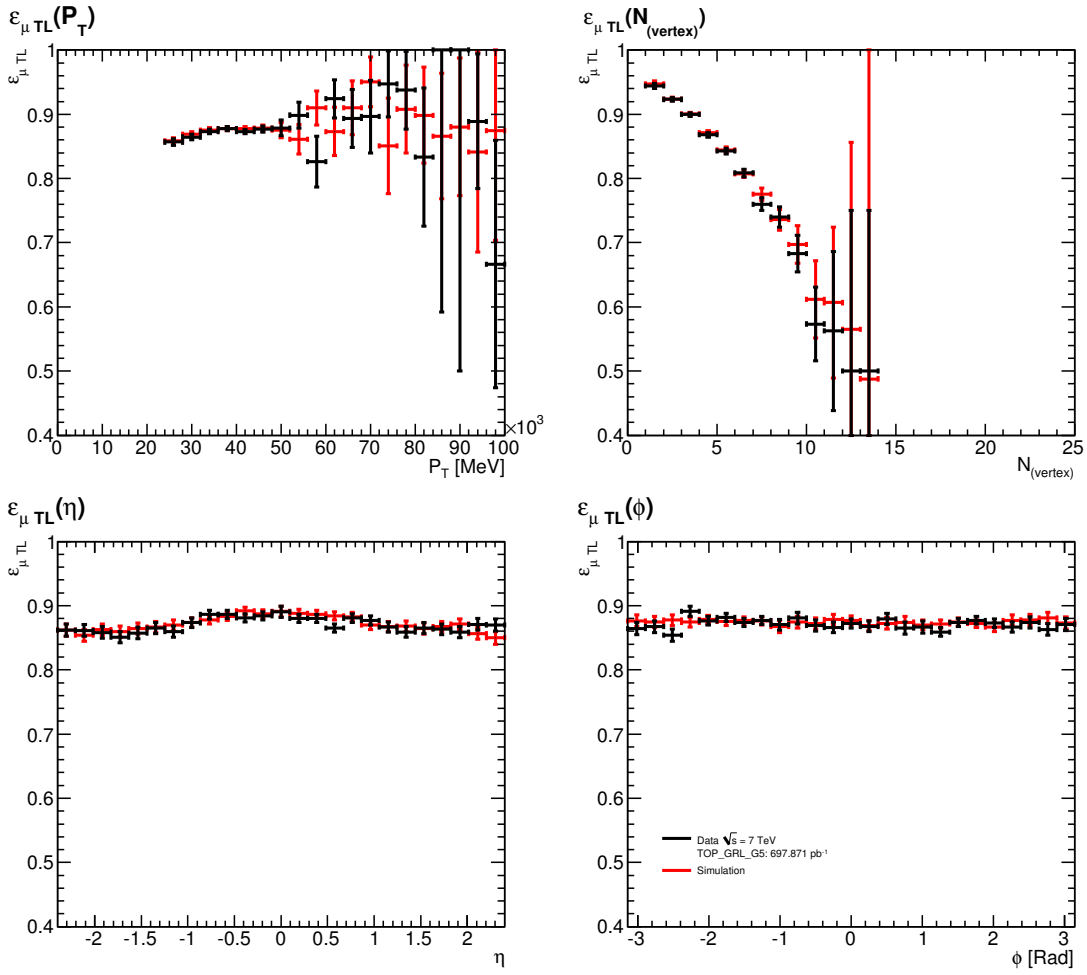

Figure 5.5: TL efficiency measured from $Z \to \mu\mu$ events in data (black) and MC (red).

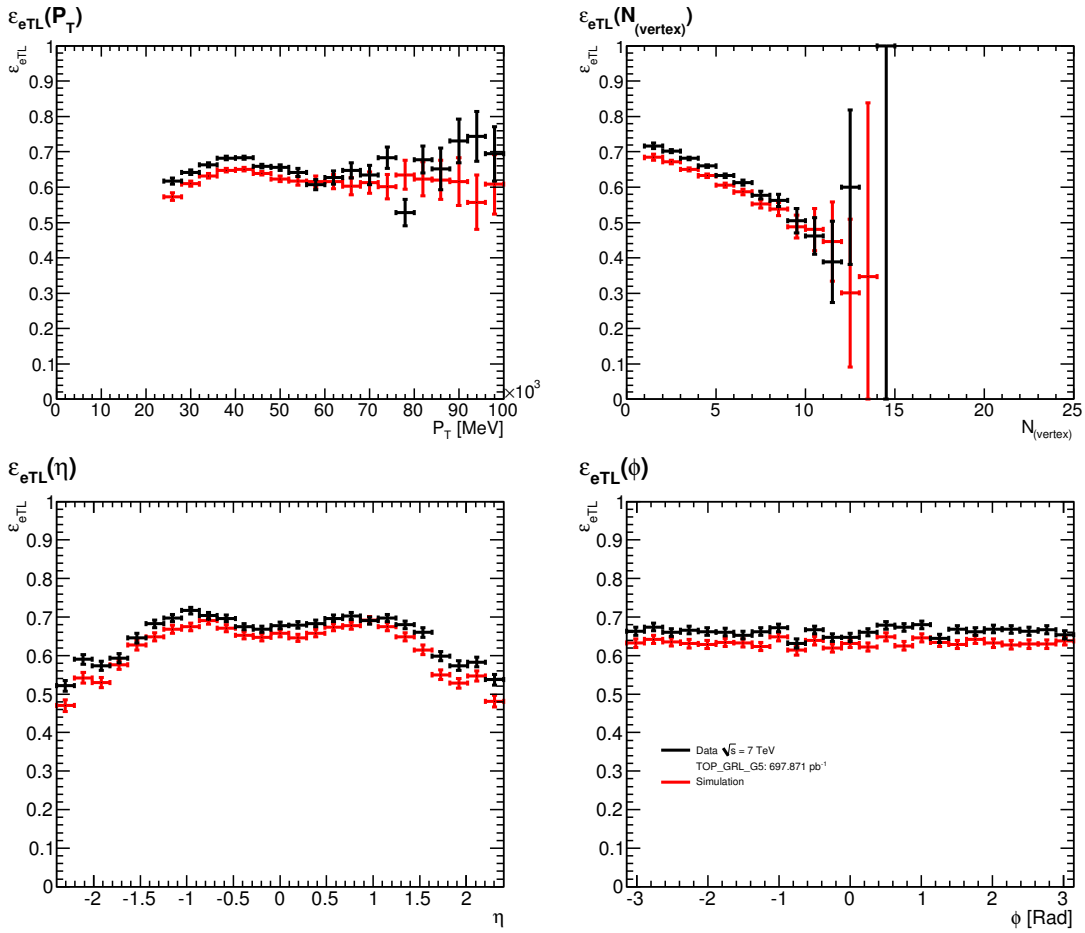

Figure 5.6: TL efficiency measured from $Z \rightarrow ee$ events in data (black) and MC (red).

Jets in this analysis are reconstructed with the anti-k_t algorithm with a radius parameter $R = 0.4$ [99], starting from energy clusters in the calorimeter reconstructed using the scale established for electromagnetic objects. Jets are then calibrated with MC simulation-based p_T- and η-dependent correction factors to restore them to the full hadronic energy scale [100]. Jet quality criteria are applied to reject jets that could not be associated to in-time real energy deposits in the calorimeters. These faulty jets could arise from various sources ranging from temporary hardware issues in the calorimeter, the LHC beam conditions and the showers induced by cosmic-ray muons. Jets are removed if they are within $\Delta R = 0.2$ of a well-identified electron candidate, or within $\Delta R = 0.4$ of a TL candidate. Finally, jets are required to have $p_T > 25$ GeV and $|\eta| < 2.5$ (in the following referred to as 'ID jets').

Momentum Resolution

For the case of jets in the MC, a correction on the energy resolution is also applied to match that of the data. This smearing is done before the jet selection.

5.3.5 Missing Transverse Energy

A good measurement of E_T^{miss} is an important requirement for the successful identification and reconstruction of $t\bar{t}$ events. Mismeasured E_T^{miss} can significantly enhance backgrounds, like multijets or Drell-Yan, where no real E_T^{miss} is present. The E_T^{miss} for this analysis is formed from the negative vector sum of transverse momenta of all jets with $p_T > 20$ GeV and $|\eta| < 2.5$. The contribution from cells associated with electron candidates is replaced by the candidates' calibrated transverse energy. The contribution from all ID muons and other calorimeter clusters, including those not belonging to a reconstructed object, is also included. To suppress backgrounds from Drell-Yan decaying into a pair of muons, where one muon is a TL that is not accounted for in the E_T^{miss} reconstruction, the E_T^{miss} is corrected in events with a TL and an opposite-sign ID muon, with the p_T of the TL if the $\Delta\phi$ between the E_T^{miss} and the TL direction is less than 0.15 and there is no ID lepton within $\Delta R < 0.05$ of the TL (in which case the correction already has been taken care of by the E_T^{miss} algorithm). The correction is as follows:

$$\begin{aligned} E_x^{\text{miss}} &\rightarrow E_x^{\text{miss}} - p_x^{\text{TL}}, \\ E_y^{\text{miss}} &\rightarrow E_y^{\text{miss}} - p_y^{\text{TL}}. \end{aligned} \tag{5.1}$$

Figure 5.7 shows the E_T^{miss} distribution for Drell-Yan events selected in data, where the effect of this correction can be fully appreciated. In the majority of cases of the 2ID+TL events selected in the data, the

Z-boson candidate is formed by two ID leptons, and thus the correction is rarely used there. On April 30th 2011, six of the front end boards (FEBs) were lost due to a problem with a controller board. This problem was fixed on July 13th, 2011. The dead electronics were not originally modelled in the MC samples used. The effect to be considered is the impact of the jets mis-measured due to the dead FEBs, and the electrons mis-measured or missing due to the dead FEBs. A correction on MC is implemented by removing events with the jets with $p_T > 20$ GeV directed at the dead region (with a distance $\Delta R < 0.1$). $E_T^{\text{miss}} > 20$ GeV is required, after all corrections.

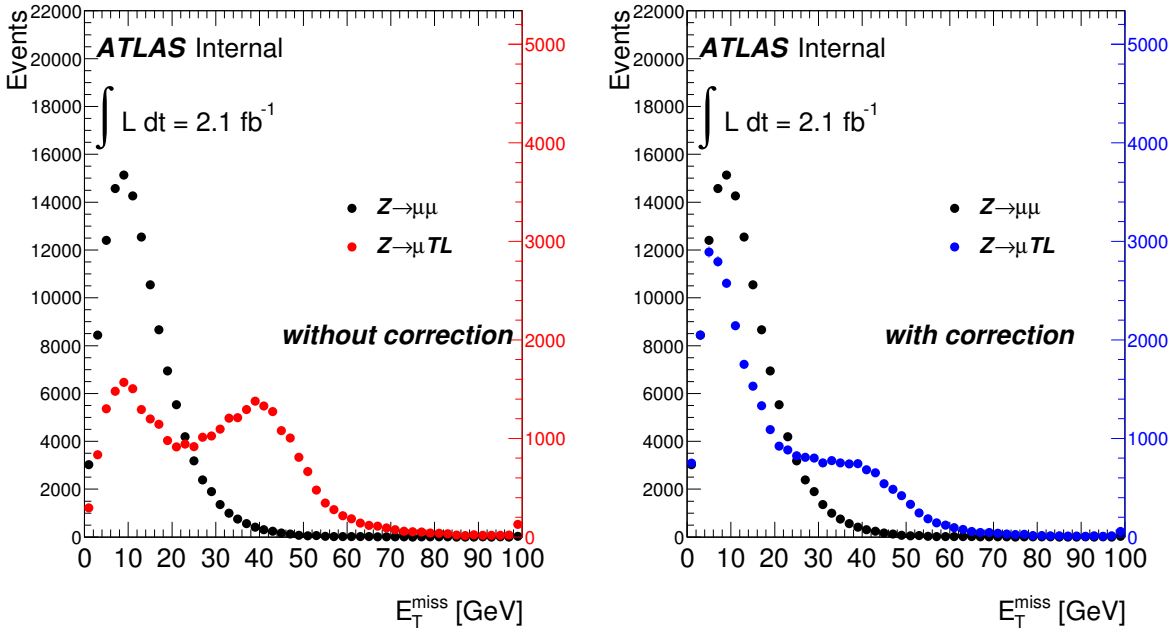

(a) (b)

Figure 5.7: E_T^{miss} distribution for events in the data with two opposite charge leptons with invariant mass within 15 GeV of $m_Z = 91.2$ GeV. In black events with two ID muons, in which case the E_T^{miss} has been properly corrected for. In red events with one muon and one exclusive TL without the correction described by Equation 5.1, and in blue, those events after that correction.

5.4 Heavy Flavor Tagging

To suppress the relatively high backgrounds in which TLs do not come from W- or Z-boson decay, b-tagging is employed. Events are required to have at least one jet consistent with originating from a b-quark. Jets are identified as b-quark candidates ('b-tagged') by an algorithm (IP3D+SV1 tagger) [101] that forms a likelihood ratio of b- and light-quark jet hypotheses using a variety of kinematic variables such as the signed

impact parameter significance of well measured tracks associated with a given jet, the decay length significance associated with a reconstructed secondary vertex and the invariant mass of all tracks associated to the secondary vertex. The cut on the combined likelihood ratio has been chosen for this analysis such that a b-tagging efficiency of $\approx 80\%$ per b-jet in $t\bar{t}$ candidate events is achieved. Other values of interest, such as purity and rejection factors (RF), are shown in Table 5.4.

IP3D+SV1 Tagger				
b-jet efficiency	purity	light-quark RF	c-quark RF	τ RF
0.80	0.76	11	3	4

Table 5.4: Parameters of the b-tagger at the chosen working point, measured in $t\bar{t}$ candidate events in a MC sample.

Scale Factors

The performance estimates of the b-jet tagger are derived on data samples. Ideally, the performance of any b-tagging algorithm depends only on the jet properties and is independent of any other characteristics of the event. Even though this is unlikely to be satisfied, it is hoped that such dependencies are properly described in simulated samples. Data-to-MC tagging and mis-tagging efficiency scale factors relate efficiencies measured in data to their counterparts in MC. These scale factors are applied to MC samples used in the 2ID+TL analysis, where b-tagging is used.

5.5 Data Sample

This search for FCNC top quark decays is done in $\sqrt{s} = 7$ TeV pp collisions data taken by ATLAS between March and August 2011. Only the periods in which all relevant detector components were operating properly are used, resulting in a data sample with a total integrated luminosity of 2.1 fb^{-1}. The uncertainty on this integrated luminosity is 3.7% [72]. Figure 5.8 shows the cumulative luminosity per day (for the data periods used in this analysis) before the good run selection. The mean number of interactions per bunch-crossing (pile-up) varies between 5.7 and 7.1 for the different data-taking periods as was shown in Figure 4.2(b).

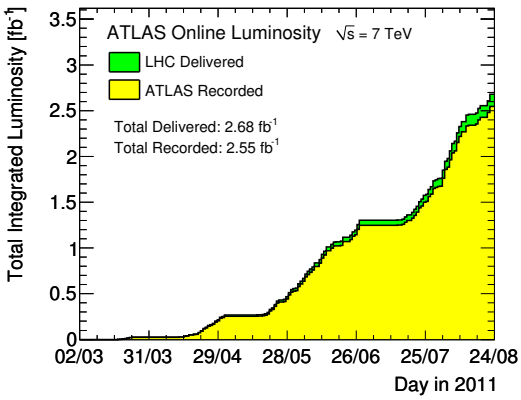

Figure 5.8: Cumulative luminosity versus day delivered to (green), and recorded by ATLAS (yellow) during stable beams and for pp collisions at 7 TeV center-of-mass energy in 2011.

5.6 $t\bar{t}$ Signal

As mentioned above, in order to reduce contribution from multijet background, only leptonic decays of the W- and the Z-boson are considered signal. Therefore, for the event selection, three high p_T leptons, at least two jets and relatively high E_T^{miss} are required. The event selection is finalized with the reconstruction of the two top quarks, and corresponding constrainst on their masses. There are two base-line analyses for this search. The first one, '2ID +TL' selects two isolated, fully reconstructed ID leptons, and one TL, whereas the second one, '3ID', selects three ID leptons. Given that the selected TL in the 2ID+TL analysis is required to be exclusive of any electron or muon selected by the 3ID analysis, these two channels are orthogonal. The 2ID+TL channel increases the acceptance with respect to the 3ID channel alone by 22%. This thesis fully describes the 2ID+TL analysis, however, a brief description of the 3ID analysis is presented in Section 5.6.2 for completeness, given that the final result arises from a combination of both channels.

5.6.1 2ID + TL Analysis

Event Preselection

At the preselection level, events are required to pass one of the single-lepton triggers, as described in Section 5.2, with the corresponding matching lepton candidate. To reject events from non-collision background, events are also required to have at least one good primary vertex. Events are discarded if any jet with $p_T > 20$ GeV fails quality cuts designed to reject jets arising from calorimeter noise or activity inconsistent with the bunch-crossing time [100, 102]. If an electron candidate and a muon candidate share a track, the

event is also discarded. Events with noise bursts in the LAr calorimeter are removed. Events with exactly three leptons, two ID leptons and one exclusive TL, are selected. The three leptons have to be matched to the same good primary vertex, which suppresses events from pile-up and secondary interactions. The TL is required to have $p_T > 25$ GeV, whereas the ID leptons are required to have $p_T > 20$ GeV. At least two ID jets and $E_T^{\text{miss}} > 20$ Gev are required. At least one of the ID jets in the event must be b-tagged. The preselection is completed by requiring at least two leptons of the same flavor and opposite charge, to account for the Z-boson from the FCNC decay of one of the top quarks. For this requirement, the TL (of unknown flavor) it is assigned the flavor of the lepton with which it is paired. In 2.05 fb^{-1} there are a total of 28 events passing the preselection criteria and an expected background of 26.5 ± 4.9. The details of the background evaluation are given in Chapter 6. Distributions of relevant variables obtained after these cuts are shown in Figure 5.9.

Event Reconstruction

To complete the event selection the mass of the two top quarks can be reconstructed from the corresponding decay particles, taking advantage of the energy-momentum conservation. Background events are expected to fit less well with the $t\bar{t}$ hypothesis, this provides an opportunity for furher signal and background separation. Given that the neutrino from the SM single lepton decay of the top quark ($t \to Wb \to b\ell\nu$) goes undetected, its four-momentum needs to be evaluated. This can be done by assuming the E_T^{miss} to be the neutrino transverse momentum, p_T^{ν}. The longitudinal component of the neutrino momentum (p_z^{ν}) is then determined together with the choice for the jet and lepton combination by minimizing the following expression:

$$\chi^2 = \frac{\left(m^{\text{reco}}_{j_a\ell_a\ell_b} - m_t\right)^2}{\sigma_t^2} + \frac{\left(m^{\text{reco}}_{j_b\ell_c\nu} - m_t\right)^2}{\sigma_t^2} + \frac{\left(m^{\text{reco}}_{\ell_c\nu} - m_W\right)^2}{\sigma_W^2} + \frac{\left(m^{\text{reco}}_{\ell_a\ell_b} - m_Z\right)^2}{\sigma_Z^2}, \tag{5.2}$$

where $m^{\text{reco}}_{j_a\ell_a\ell_b}$, $m^{\text{reco}}_{j_b\ell_c\nu}$, $m^{\text{reco}}_{\ell_c\nu}$ and $m^{\text{reco}}_{\ell_a\ell_b}$, are the reconstructed masses of the top quark candidate decaying through the FCNC decay, the top quark candidate with SM decay, the W boson candidate from the top quark with SM decay and of the Z boson candidate from the top quark FCNC decay, respectively. There the masses are $m_t = 172.5$ GeV, $m_W = 80.4$ GeV, and $m_Z = 91.2$ GeV, and the widths are $\sigma_t = 14$ GeV, $\sigma_W = 10$ GeV and $\sigma_Z = 3$ GeV. For each ID jet and lepton (the two ID leptons and the unique TL) combination, in which the Z-boson candidate is built from two leptons of the same flavor and opposite charges, the χ^2 minimization gives the value for p_z^{ν}. From all combinations, the one with the minimum χ^2 is chosen along with the corresponding p_z^{ν} value. Only the two leading ID jets are used in the reconstruction of the

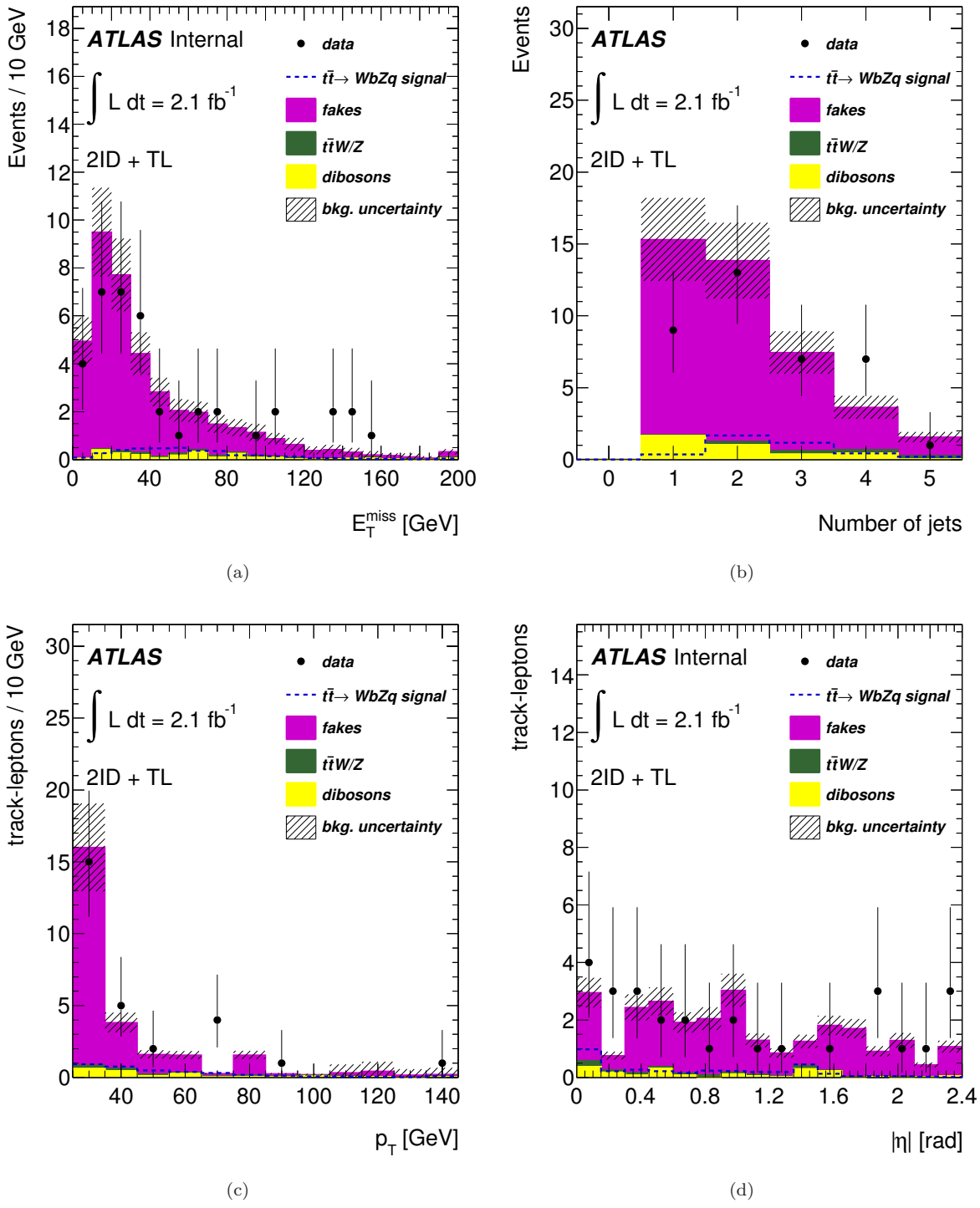

Figure 5.9: (a) E_T^{miss}, (b) number of ID jets, and (c) p_T and (d) η of the TL distributions for pre-selected b-tagged events. The dashed lines show the shapes of the signal distributions, normalized to the observed BR limit, at 95% CL. The uncertainties on the background are both statistical and systematic.

event kinematics, however no b-jet identification is used. The distributions of the reconstructed mass of the Z- and W-boson and the two top quarks, this is $m^{\text{reco}}_{\ell_a\ell_b}$, $m^{\text{reco}}_{\ell_c\nu}$, $m^{\text{reco}}_{j_b\ell_c\nu}$ and $m^{\text{reco}}_{j_a\ell_a\ell_b}$ respectively, are shown in Figure 5.10.

For the final selection, events are rejected unless the reconstructed masses of the two top quark candidates are within 40 GeV of m_t, the reconstructed W-boson candidate mass is within 30 GeV of m_W, and the reconstructed Z-boson candidate mass is within 15 GeV of m_Z. Of the 2ID+TL events in the data that pass the preselection, 71% are rejected by the χ^2 mass cuts. The efficiency of the FCNC MC events to pass the χ^2 selection is 66%, while background events pass at a 34% rate. After the application of the χ^2 minimization and invariant mass cuts there are a total of 8 events in the data and an expected background of 8.9 ± 2.3. The signal efficiency in the final selection is $\left(0.045 \pm 0.001^{+0.006}_{-0.007}\right)\%$. Table 5.5 gives a cut flow of the event selection in data. The signal efficiency determination is explained in what follows, and the backgrounds in Chapter 6. Figure 5.11 shows distributions of relevant variables at the final selection level. The mass distribution of the W- and Z-bosons and the two top quarks candidates after all mass cuts are shown in Figure 5.12.

Preselection	
Events with at least 2 ID leptons, passing event cleaning cuts	69883
Trigger	69853
Trigger Matching	69853
Exactly 2 ID leptons and one TL, from same primary vertex	320
Z-boson candidate	320
$E_T^{\text{miss}} > 20$ GeV	129
# jets ≥ 2	55
at least one b-tagged jet	28
Final Selection	
mass cuts after χ^2 minimization	8

Table 5.5: Data cutflow.

Acceptance

The signal acceptance is measured using the TopRex signal MC samples described in Section 4.2. These MC samples are divided according to the leptonic decays of the W- and Z-bosons in the final state. Table 5.6 shows the fraction of events accepted in each category. The final signal efficiency, accounting for the W- and Z-bosons decay BRs, is $\left(0.045 \pm 0.001^{+0.006}_{-0.007}\right)\%$. The increase in the acceptance, with respect to the 3ID

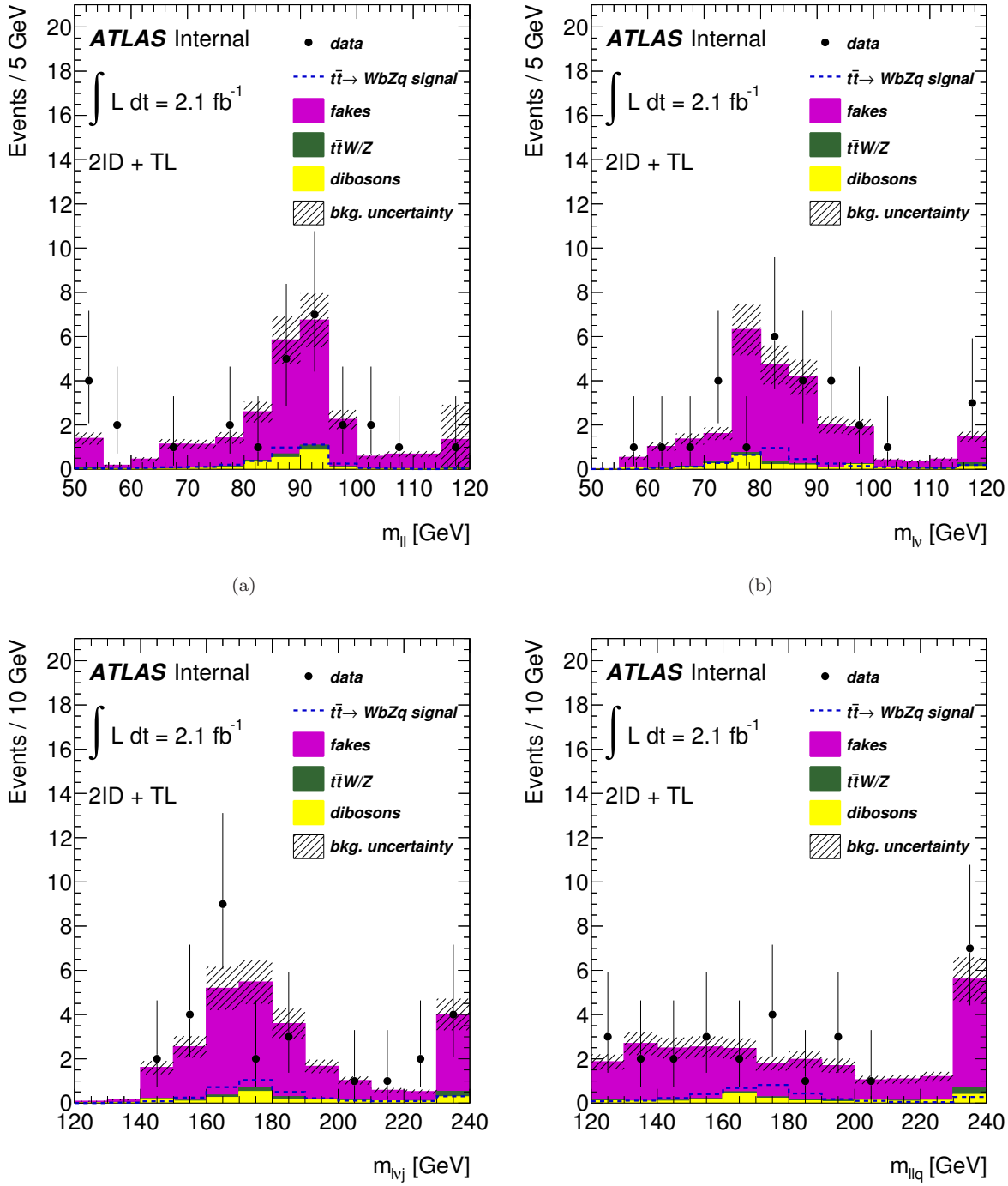

Figure 5.10: The reconstructed mass of the (a) two leptons assigned to the Z-boson decay, (a) the lepton and the neutrino assigned to the W-boson, (c) the lepton, neutrino and jet assigned to the top quark with the SM decay, and (d) the two leptons and jet assigned to the top quark with FCNC decay after the χ^2 minimization. The dashed lines show the shapes of the signal distributions (normalized to the observed BR, at 95% CL). The uncertainties on the background are both statistical and systematic.

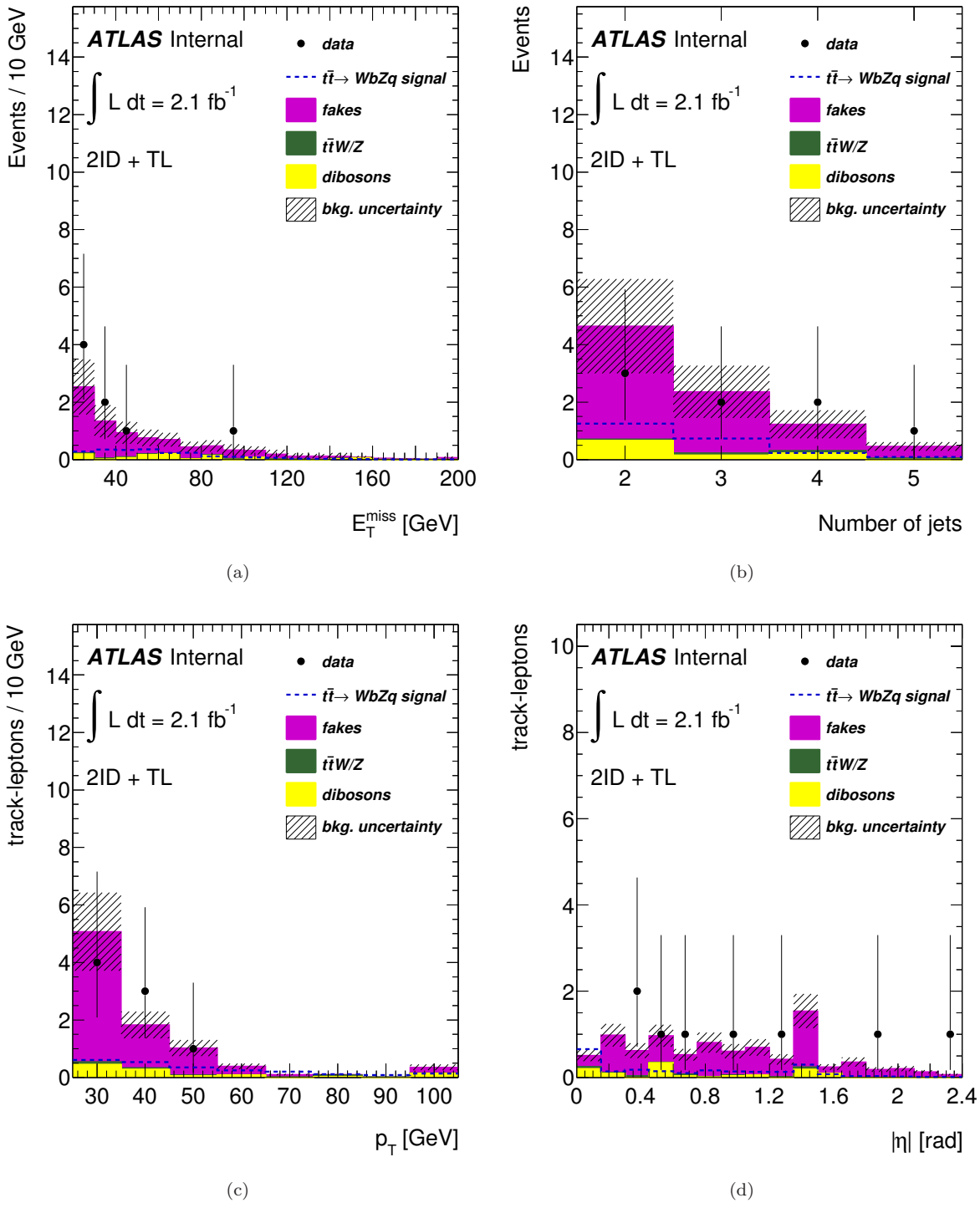

(a) (b)

(c) (d)

Figure 5.11: (a) E_T^{miss}, (b) number of jets, and (c) p_T and (d) η of the TL distributions for events after the final selection. The dashed lines show the shapes of the signal distributions, normalized to the observed BR limit, at 95% CL. The uncertainties on the background are both statistical and systematic.

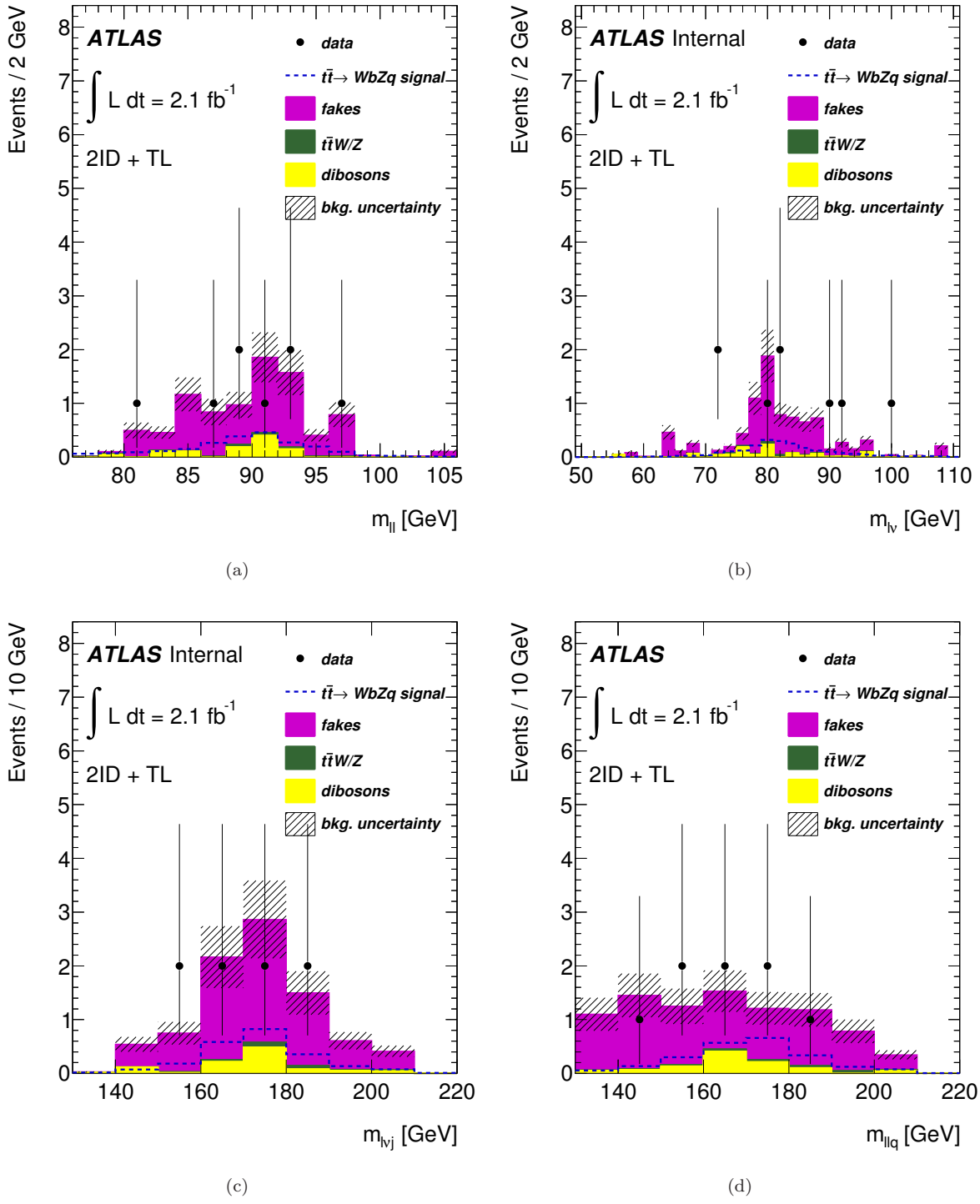

Figure 5.12: The reconstructed mass of the (a) two leptons assigned to the Z-boson decay, (a) the lepton and the neutrino assigned to the W-boson, (c) the lepton, neutrino and jet assigned to the top quark with the SM decay, and (d) the two leptons and jet assigned to the top quark with FCNC decay after the χ^2 minimization, and the corresponding cuts on the different masses. The dashed lines show the shapes of the signal distributions (normalized to the observed BR, at 95% CL). The uncertainties on the background are both statistical and systematic.

analysis, is 22%. Figure 5.13(a) shows the generator channel on these 2ID+TL events and Figure 5.13(b) shows the distribution in η of the TLs accepted by the analysis. The gain in acceptance comes partly from recovery of efficiency losses in the e and μ selection, partly from acceptance of hadronic τ decays, but primarily from electrons and muons in the transition regions and gaps in detector coverage. In Figure 5.13(b), the gap in muon coverage around $\eta \sim 0$, and between the A and C sides of the spectrometer is clearly seen, as well as other more subtle features of the detector.

decay	fraction of events accepted [%]
$t\bar{t} \to \ell\nu\ell\ell$	$2.60 \pm 0.05^{+0.32}_{-0.37}$
$t\bar{t} \to \ell\nu\tau\tau, \tau\nu\tau\tau$	$0.04 \pm 0.01^{+0.02}_{-0.02}$
$t\bar{t} \to \tau\nu\ell\ell$	$0.94 \pm 0.04^{+0.17}_{-0.18}$
signal efficiency	$\left(0.045 \pm 0.001^{+0.006}_{-0.007}\right)\%$

Table 5.6: $\ell = e, \mu$. Fraction of events accepted per signal MC sample. The listed uncertainties are statistical and systematic, respectively. The signal efficiency quoted at the bottom has been convoluted with the corresponding Z and W BRs.

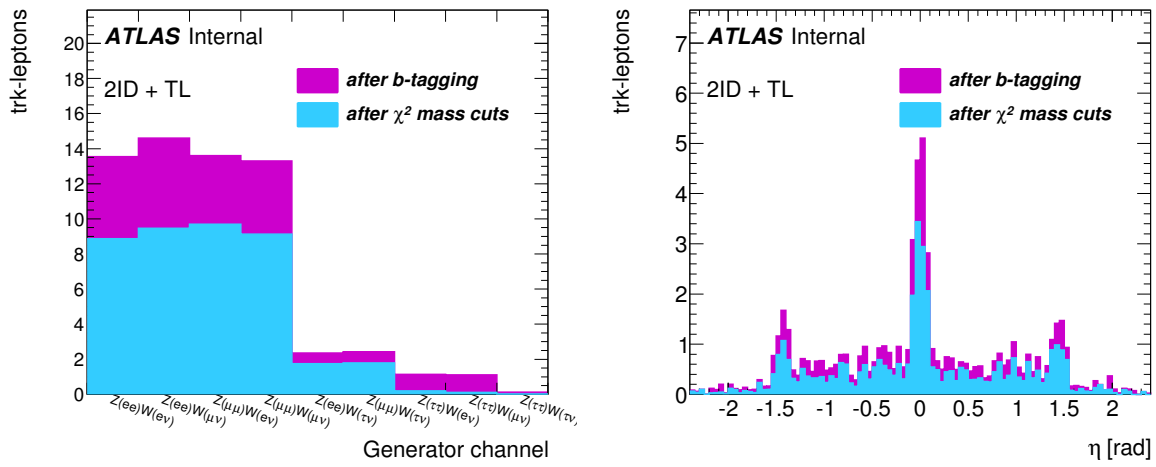

(a) (b)

Figure 5.13: (a) Generator channel of the 2ID+TL events selected before and after the χ^2 mass cuts and (b) η distribution of the TLs of these events. These TLs are exclusive of any electrons or muons. The units in the y-axis are arbitrary, but the corresponding BRs for the W- and the Z-boson decays have been taken into account.

To examine the effect of pile-up on the acceptance, the acceptance is measured as a function of the mean number of interactions per bunch crossing ($\langle\mu\rangle$). This is shown in Figure 5.14. There the black points are before, and the magenta stars after, pileup reweighting. While there is some scatter, it looks rather statistical in nature, and there is no dramatic dependence on $\langle\mu\rangle$. The points after pileup re-weighting are

compatible with a constant within the statistical uncertainty.

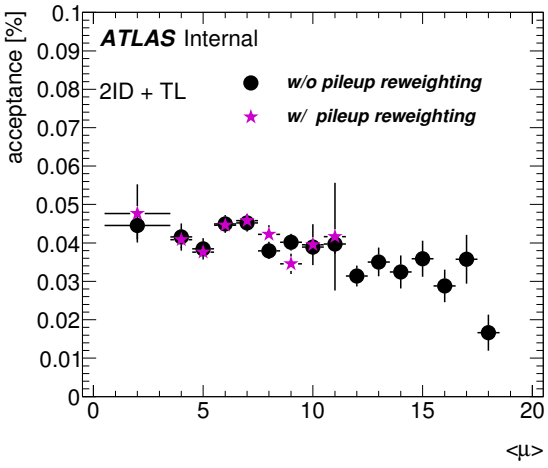

Figure 5.14: Acceptance as a function of the mean number of interactions per bunch crossing ($\langle\mu\rangle$). The black dots are raw MC events and the magenta stars are MC events after pile-up reweighting (they show the region of $\langle\mu\rangle$ relevant for the data used in this analysis).

5.6.2 3ID Analysis

The additional, orthogonal, channel used in the combined result to be presented in Chapter 8 corresponds to that where three fully reconstructed leptons (electron, muons) are selected. As mentioned above, this part of the analysis was performed by a different group in the collaboration. However it is explained here for completeness and clarity of the final result, which combines the two channels.

The 3ID selection is very similar to that of the 2ID+TL. The main difference, which ensures orthogonality, is that instead of requiring exactly two ID leptons and one TL, three ID leptons are required, with the leading lepton having $p_T > 25$ GeV. In the 2ID+TL selection this is automatically ensured by the $p_T > 25$ GeV cut used in the TL selection. Also, no b-tagging requirement is used in this analysis.

In the initial selection events are required to pass one of the single leptons triggers, and to include at least one good primary vertex. Events which contain any jet with $p_T > 20$ GeV that fails the jet cleaning requirements [102] are rejected. Events with noise bursts in the LAr calorimeter or with cosmic rays are discarded. Events with exactly three ID leptons are selected, provided the three leptons are matched to the same primary vertex. At least one of the reconstructed leptons has to match a trigger lepton. The

transverse momentum of the leading lepton and the other two leptons is required to be greater than 25 GeV and 20 GeV, respectively. Furthermore, events are required to contain at least two leptons of the same flavor and opposite charges. This initial selection is completed by requiring that the invariant mass of this lepton pair should be within 15 GeV of $m_Z = 91.2$ GeV. Figure 5.15 show distributions obtained with the 3ID analysis after the loose event selection just described. Details of the background evaluation for this channel will also be provided in Chapter 6.

The event selection is finalized by requiring at least two ID jets, and $E_T^{\text{miss}} > 20$ GeV. As in the 2ID+TL, following the initial selection, candidate events are required to be kinematically consistent with $t\bar{t}$ decay to Wb and Zq. This is done through the minimization of the χ^2 described in Equation 5.2. The final selection requires that the reconstructed W-boson candidate mass be within 30 GeV of m_W, the reconstructed Z-boson candidate mass within 15 GeV of m_Z, and the two top quark candidates within 40 GeV of m_t, where m_W, m_Z and m_t are the same values used in the 2ID+TL analysis and given following Equation 5.2 above. At this final selection level 8 data events survive the cuts. As in the 2ID+TL analysis, a signal efficiency is estimated combining the different TopRex MC samples, and measured to be $(0.205 \pm 0.003 \pm 0.022)\%$. Figure 5.16 show distributions obtained with the 3ID analysis at the final selection level.

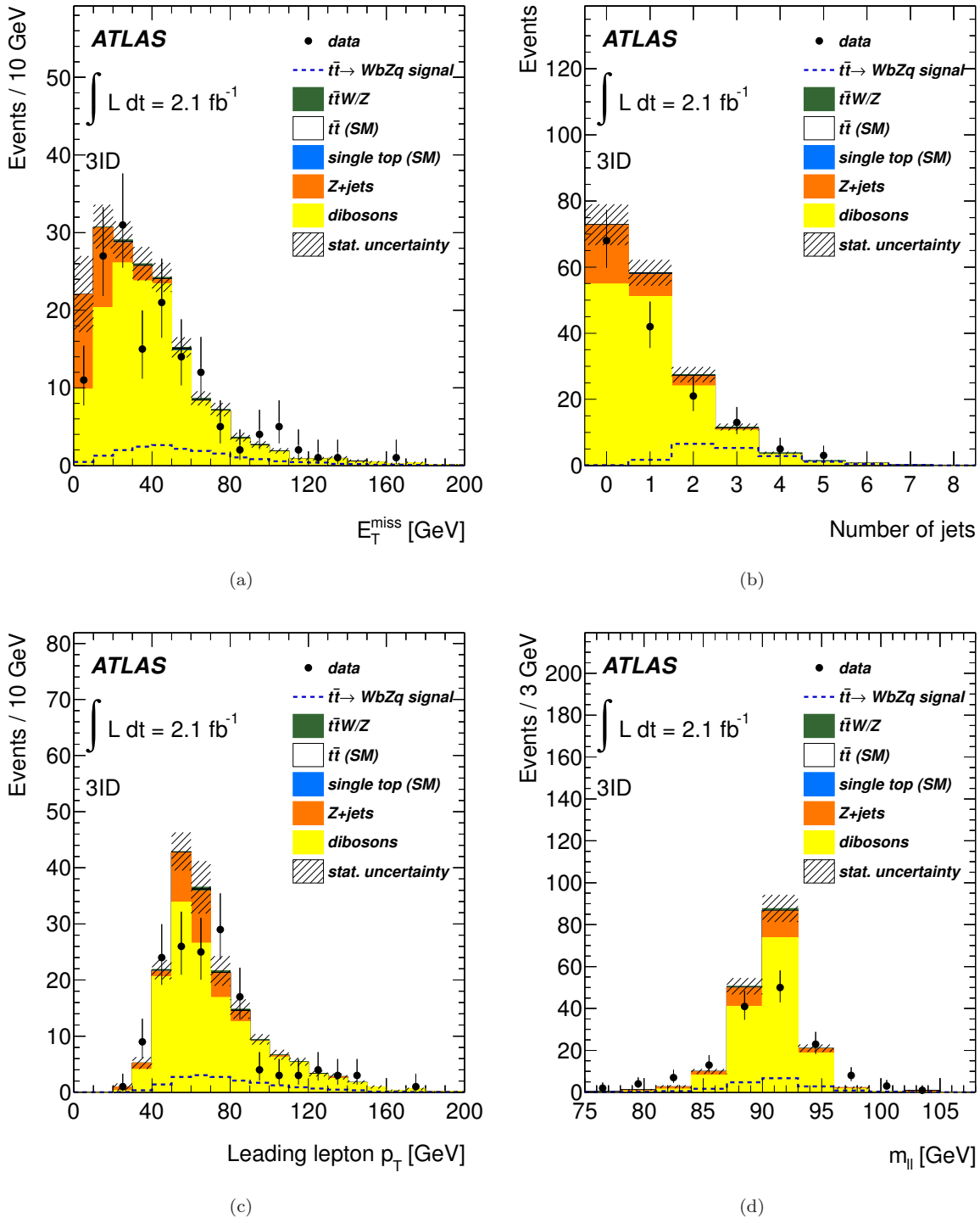

Figure 5.15: Distributions of the 3ID analysis after a loose event selection. (a) E_T^{miss}, (b) number of ID jets, (c) p_T of the leading lepton, and (d) reconstructed mass of the two leptons with same flavor and opposite charge. The uncertainties shown are both MC simulation statistical and the data-driven background estimation uncertainties. The signal distributions are normalized to the observed BR limit, at 95% CL.

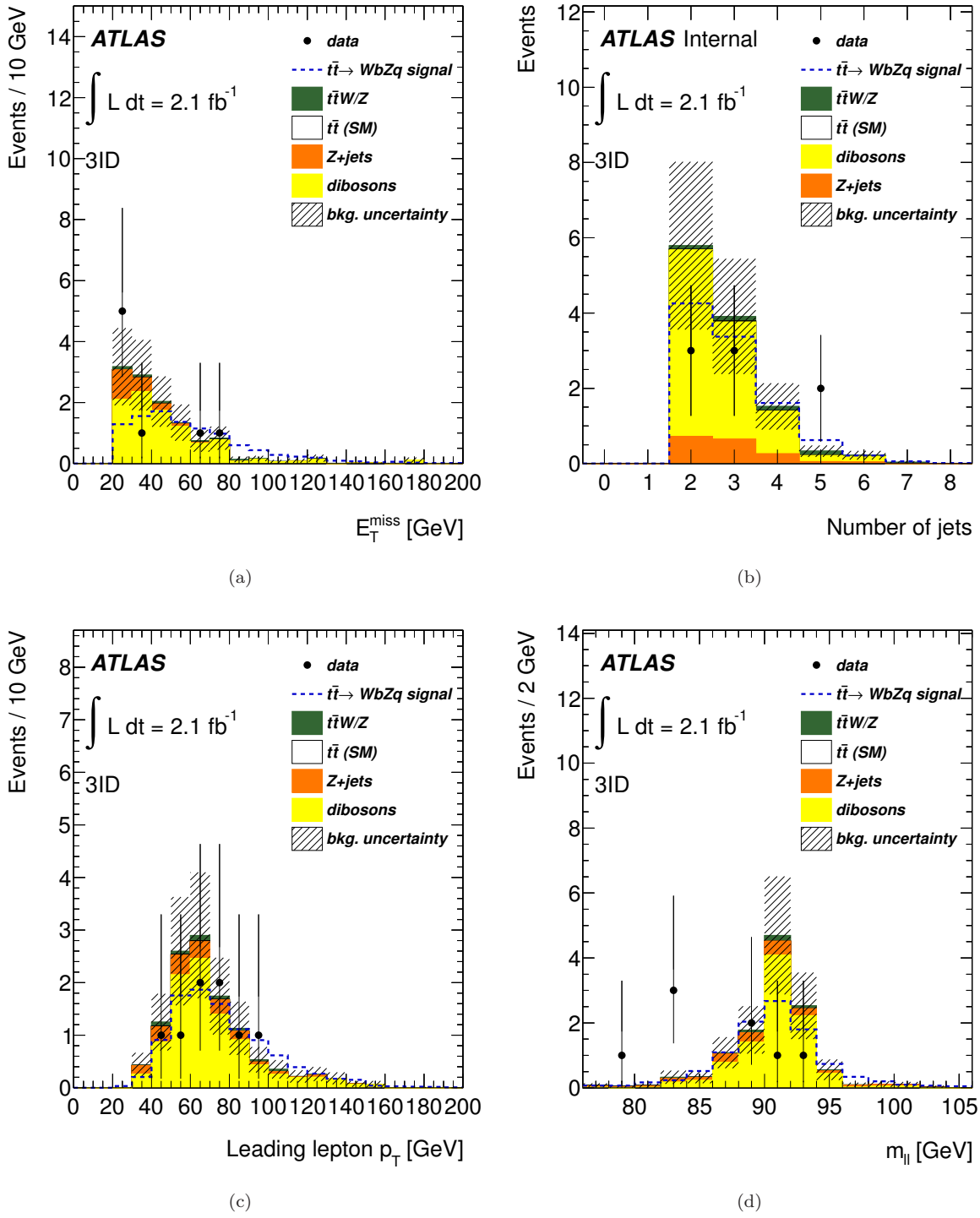

Figure 5.16: Distributions of the 3ID analysis after the final event selection. (a) E_T^{miss}, (b) number of ID jets, (c) p_T of the leading lepton, and (d) reconstructed mass of the two leptons with same flavor and opposite charge. The uncertainties shown are both MC simulation statistical and the data-driven background estimation uncertainties. The signal distributions are normalized to the observed BR limit, at 95% CL.

Chapter 6

Standard Model Background

6.1 Introduction

The background for this search comes from other SM processes that have final-state topologies similar to the signal. They can be placed in two categories: those with three real leptons and those with at least one fake lepton. In the case of the 2ID+TL selection, the former contributes about 15% of the total background, and is evaluated using the MC samples described in Chapter 4. The remaining 85% of the background consists of events with at least one 'fake' lepton, where a 'fake' lepton is any object identified as a lepton that does not arise from W- or Z-boson decay. This includes misidentified hadrons, decays in flight, photon conversions and heavy-flavor semileptonic decays. A data-driven (DD) technique has been developed to evaluate the contribution to 2ID+TL events from this background. For the 3ID selection the main background, 85% of the total, comes from events with three real leptons, and they are estimated from MC simulation as well. The remaining background is evaluated with DD methods.

6.2 Backgrounds to the 2ID + TL Analysis

6.2.1 Monte Carlo Background

Backgrounds with three real leptons arise from diboson (WZ and ZZ) production with additional jets and $t\bar{t}$ + W- or Z-boson. In the case of WZ production, the required E_T^{miss} comes from the neutrino from the leptonic W-boson decay. ZZ events can enter the signal region in several ways. The dominant modes are four-lepton decays, with one lepton not reconstructed, giving apparent E_T^{miss}, and events with one Z-boson decaying to a pair of electrons or muons, and the other to a pair of tau leptons (with one of the taus decaying to a e or μ and a pair of neutrinos). The dominant source of b-tags in diboson events comes from mis-tags of light-quark jets, with a secondary component of charm jets. In $t\bar{t} + W/Z$ events, the E_T^{miss} comes from the neutrinos from the leptonic decay of the W-bosons (including the W-bosons from the SM decays of the top-quark). In this case, the SM decays of the top-quarks provide a real b-jet. The contribution from these

two background sources, diboson and $t\bar{t}+W/Z$, is calculated applying the signal region event selection to the MC simulation, appropriate k-factors for the MC, and normalizing to the integrated luminosity of the data sample.

6.2.2 Fake Leptons Background

In the 2ID+TL selection the dominant background comes from events with at least one fake lepton. Moreover, the fake leptons are dominantly fake TLs. The contribution of fake TLs to the signal sample is predicted using a 'fake matrix' which is parameterized as a function of jet p_T and the number of good primary vertices in the event, N_{PVX}. The dependance on N_{PVX} accounts for the variable pile-up conditions along the different data periods used in this analysis. The fake matrix gives the probability that a jet will be reconstructed as a TL. This probability ('fake rate') is determined from a γ+jets data sample selected with photon triggers [1], and it is defined as follows:

$$\text{Fake Rate}\,(p_T, N_{\mathrm{PVX}}) \quad = \quad \frac{(p_T, N_{\mathrm{PVX}})\ \text{of all selected track leptons}}{(p_T, N_{\mathrm{PVX}})\ \text{of all ID jets \& jet} - \text{elements}} \tag{6.1}$$

where the TLs in the numerator pass all required cuts listed in Section 5.3.3. A fake TL can either be associated (within $\Delta R < 0.4$) with an ID-jet or not. If it is associated, and the TL p_T is larger than the associated ID-jet p_T, the TL p_T is used in its place. If it is not associated, we treat the TL as though it were a jet ("jet-element", with the same p_T as the TL) that fragmented to a single high p_T track, leaving no remnants that are reconstructed as a jet. The denominator includes both ID-jets and jet-elements. The fake rates for TLs vs. jet p_T and N_{PVX} are shown in Figure 6.1.

To predict the background from fake TLs, the fake matrix is then applied to a parent sample selected with all of the signal region requirements with the exception of the three leptons. Instead, two ID leptons are required. The model on which the fake matrix is predicated is that a jet in the parent sample is reconstructed as a TL with a probability given by the value in the fake matrix for a jet of given p_T in an event with a given N_{PVX}. A parent sample event with two ID leptons and N jets, satisfying all other signal region cuts described in Section 5.6.1, is used to predict the fake background in signal-region events with $N-1$ jets, as depicted in Figure 6.2. Note that even if the jet that is associated with the fake TL is separately reconstructed as a jet, it will be removed by the overlap removal criteria applied to jets within $\Delta R < 0.4$ of a TL. The fake prediction for a given event with N jets is given by the sum of the fake probabilities from

[1] More details of the γ+jets selection are given in Appendix A.

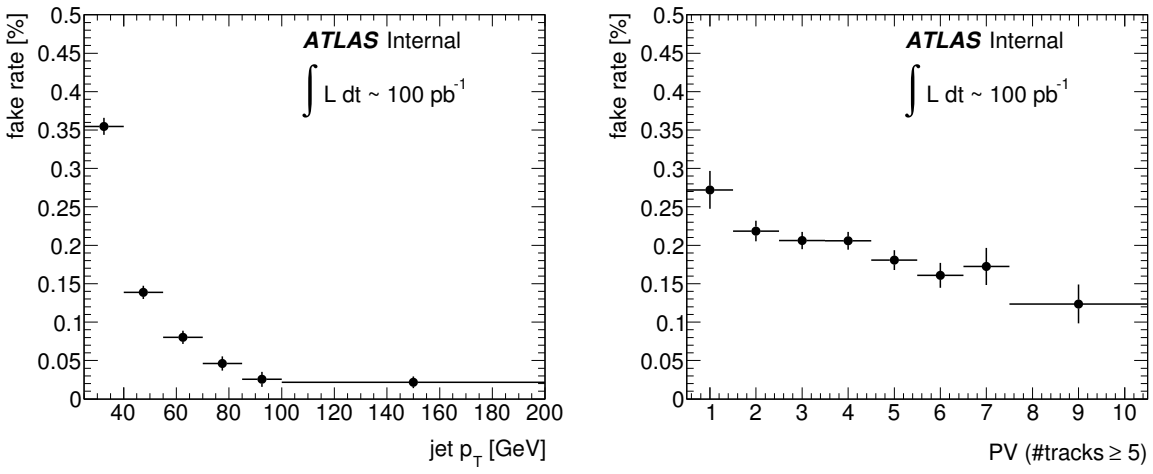

(a) (b)

Figure 6.1: TL fake rate measured from γ+jets events vs. (a) jet p_T and (b) number of primary vertices. The quoted integrated luminosity is a result of the photon trigger prescale.

the matrix of each of the jets. Note that this technique gives the number of fake leptons, not the number of events with at least one fake lepton.

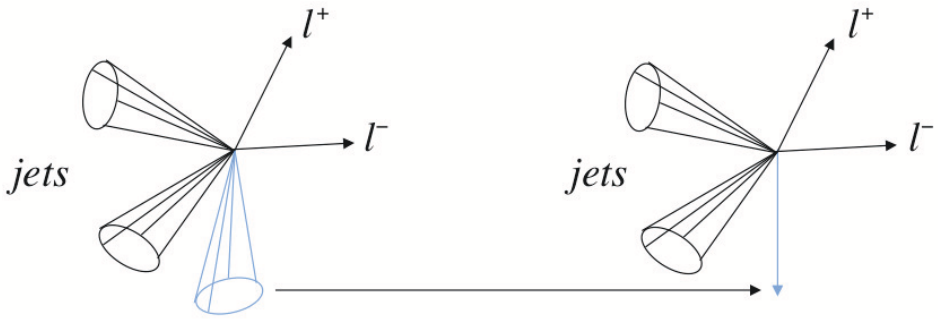

Figure 6.2: Illustration showing a dilepton + 3 jet event being reconstructed as a trilepton + 2 jet event with a fake lepton.

Because of the b-tag requirement in the event selection, only events with at least a b-tagged jet contribute to the fake prediction, and a b-tagged jet only contributes to that prediction if there is another jet in the event that is b-tagged. This accounts for the fact that if a fake TL emerges from a b-tagged jet, the jet itself will be removed by the overlap removal and can no longer provide a tag. The 2ID+TL selection requires a Z-boson candidate, i.e. an opposite-charge, same-flavor, lepton pair. Therefore the parent sample with two

ID leptons provides three different scenarios:

a. Opposite-charge ID leptons

b. Two positively-charged ID leptons

c. Two negatively-charged ID leptons

In case a., the fake TL can have either charge so no charge discrimination is used in the numerator of the fake matrix. In case b. the fake TL must be negatively charged, and a fake matrix with only negatively-charged TLs in the numerator is used. Similarly, case c. requires a positively-charged TL and a fake matrix with only positively-charged TLs in the numerator is used. Note that in all cases the same-flavor requirement is automatically satisfied because the TL is taken to have the same flavor as the ID lepton with which it is paired. The distributions shown in Figure 6.1 correspond to the full fake matrix used for case a. above.

To account for the reconstructed mass cuts done after the χ^2 minimization described in Section 5.6.1, a correction is made to the fakes prediction described above: the predicted fakes are multiplied by the fraction of 2ID+fake TLs that pass the χ^2 mass cuts. Because this technique does predict the 4-momenta vector of the fake TL, needed for the invariant mass calculations, this fraction is taken from a MC sample with the expected mixture of Z+jets, $t\bar{t}$, W+jets, and single top events, and found to be $(31.2 \pm 10.2)\%$.

The parent sample with two ID leptons contains all sources of background that can enter the signal region with a fake TL: Z+jets, dilepton decays of $t\bar{t}$, and single top. The two ID leptons selected in the parent sample include both real and fake ID leptons, so the multijet background is also included (although expected to be very small). Thus the procedure predicts the full background contribution with a fake TL. Furthermore, 2% of the total fake lepton background (at the final selection level) is added to account for events with one real ID lepton, one real TL, and one fake ID lepton. This is evaluated in MC by measuring the fraction of selected events with one fake ID lepton, over events with one fake TL. A conservative 100% systematic uncertainty has been set on this number.

The predicted number of events at the final selection level with two ID leptons plus a fake TL is given in Table 6.1. All corrections listed above are included. The quoted systematic uncertainty, 20%, is explained in Chapter 7.

6.2.3 Summary

The yields of the expected background and the data observation, as quoted in Section 5.6.1, for the preselection and the final selection are presented in Table 6.2 and Table 6.3, respectively. In both stages of the selection, the observed signal candidates are consistent with the number of background events expected.

6.3 Backgrounds to the 3ID Analysis

A complete description of the evaluation of backgrounds to the 3ID analysis is presented in Appendix B and in Reference [8].

# jets	2ID + fake TL prediction
2	$4.1 \pm 1.4 \pm 0.8$
3	$2.1 \pm 0.8 \pm 0.4$
4	$0.9 \pm 0.3 \pm 0.2$
≥ 5	$0.4 \pm 0.1 \pm 0.1$
≥ 2	$7.6 \pm 1.6 \pm 1.5$

Table 6.1: Predicted number of fake background events per jet multiplicity. The signal region background prediction corresponds to $\geq$2 jets. The listed uncertainties are statistical and systematic, respectively.

2ID+TL Preselection	
ZZ and WZ	$1.9\,^{+\,0.9}_{-\,1.0}$
$t\bar{t}W$ and $t\bar{t}Z$	0.9 ± 0.2
fakes	23.7 ± 4.8
expected background	26.5 ± 4.9
data	28

Table 6.2: Expected backgrounds in the 2ID+TL analysis and the number of events observed in the data at the pre-selection level. Both statistical and systematic uncertainties are included.

2ID + TL Final Selection	
ZZ and WZ	$1.0\,^{+\,0.5}_{-\,0.6}$
$t\bar{t}W$ and $t\bar{t}Z$	0.25 ± 0.05
fakes	7.6 ± 2.2
expected background	8.9 ± 2.3
data	8

Table 6.3: Expected backgrounds in the 2ID+TL analysis and the number of events observed in the data at the final selection level. Both statistical and systematic uncertainties are included.

3ID Final Selection	
ZZ and WZ	9.5 ± 4.4
$t\bar{t}W$ and $t\bar{t}Z$	0.51 ± 0.14
$t\bar{t}$, WW	0.07 ± 0.02
Z+jets	1.7 ± 0.7
Single-top	0.01 ± 0.01
2+3 fake leptons	$0.0\ ^{+\ 0.2}_{-\ 0.0}$
expected background	11.8 ± 4.4
data	8

Table 6.4: Number of selected data events, expected number of background events (ZZ, WZ and $t\bar{t}W/Z$ events estimated from Monte Carlo simulation samples and the DD estimations for 1 and 2+3 fake leptons) and the estimated signal efficiency (multiplied by the corresponding W and Z bosons' BRs), after the event final selection. The corresponding statistical uncertainties are also shown.

6.3.1 Summary

The yields of the expected background and the data observation for the final selection of the 3ID selection are presented in Table 6.4. The number of signal candidates in data are consistent with the expected background within one sigma.

Chapter 7

Systematic Uncertainties

7.1 Introduction

Several systematic uncertainties can influence the number of expected signal and/or background events. To study the effect of the different sources of systematic uncertainty, the corresponding central value is independently varied by the estimated uncertainty. For each variation the expected number of background events and signal efficiencies are compared with the nominal values. The different sources of uncertainties are presented below in a loose classification.

7.2 Object Specific Systematic Uncertainties

Muons

The uncertainty on the muon efficiency scale factors are used to estimate the systematic uncertainty due to MC modelling of the muon reconstruction, identification and trigger. This is done, separately for each systematic shift, by recomputing the background yields and signal acceptance using the shifted scale factors. The bias on the different scale factors is taken from different sources: di-muon invariant mass cut around the Z-boson mass, trigger matching cuts, and the effect of the isolation in the muon selection. Similarly, the p_T scale and resolution corrections are varied by their uncertainty to measure the net systematic uncertainty due to these corrections.

Electrons

In a similar fashion as done for muons, the systematic uncertainty due to modelling of the electron trigger, reconstruction and selection efficiencies is evaluated by varying the corresponding scale factors by their uncertainties, and re-computing the yields and acceptance from MC. The electron energy scale, corrected in

data, has systematic uncertainties within ±1-1.5% for the η range of interest, dominated by uncertainties from the detector material and the presampler energy scale, but also include the event selection, pile-up, and hardware modelling. This uncertainty, along with the uncertainty due to the energy smearing, is measured in MC, by shifting the correction up or down by one standard deviation.

Track-Leptons

The uncertainty on the TL scale factors, as quoted in Section 5.3.3, 0.997 ± 0.002 and 1.047 ± 0.005, for $Z \to ee$ and $Z \to \mu\mu$, respectively, is used as a measure of the systematic uncertainty due to the use of these scale factors. For this, the central value of the scale factors is varied with the corresponding systematic shift, and the background expectation and signal efficiencies are re-computed. In addition, a systematic uncertainty due to the TL p_T scale and resolution is also included. To compute this, the resolution and energy/momentum scale of the TLs are compared in data and MC in $Z \to ee$ and $Z \to \mu\mu$ events. Figure 7.1 shows the distributions in each case. For the case of muons, the distributions are fit to a Breit-Wigner convoluted with a Gaussian. For the electrons, the distributions are fit to a pair of Crystal Ball (CB) functions. Figure 7.1 shows these fits in blue, and the fit parameters are displayed in each case. The main difference between electrons and muons, evident in the lower mass tail, is the fact that electrons reconstructed as TLs do not have a correction for the energy lost due to radiation in the inner detector. The MC momentum scale and resolution uncertainties are extracted from these distributions. The systematic uncertainty on the p_T scale is taken to be half the difference in the peak of these fits (to account for the two leptons), whereas the systematic uncertainty on the p_T resolution is the quadrature difference in the widths divided by $\sqrt{2}$. The MC modelling is quite good, and so the differences in the scale and resolution are small. For the muons (reconstructed as TLs), the MC Z-boson peak is at 90.9013 GeV and in data is at 90.8006 GeV, resulting in a systematic uncertainty on the p_T scale of 0.06%. The resolution uncertainty in this case is extracted from the quadrature difference in the fit Gaussian width of 4.54 GeV in the data vs. 3.93 GeV in the MC. Using a mean p_T of 40 GeV, measured in MC, the systematic uncertainty on the TL resolution is $\sqrt{4.54^2 - 3.93^2}/(\sqrt{2} \cdot 40) = 4.0\%$. The use of a double CB for the electron channel distributions, makes the interpretation of the fit parameters less straightforward. In this case, the CB function determines the approximately Gaussian falling edge in the ee events, to give a p_T scale systematic uncertainty of 0.04% (the data-MC difference in the peak position is 0.075 GeV) and a p_T resolution uncertainty of 5.4%.

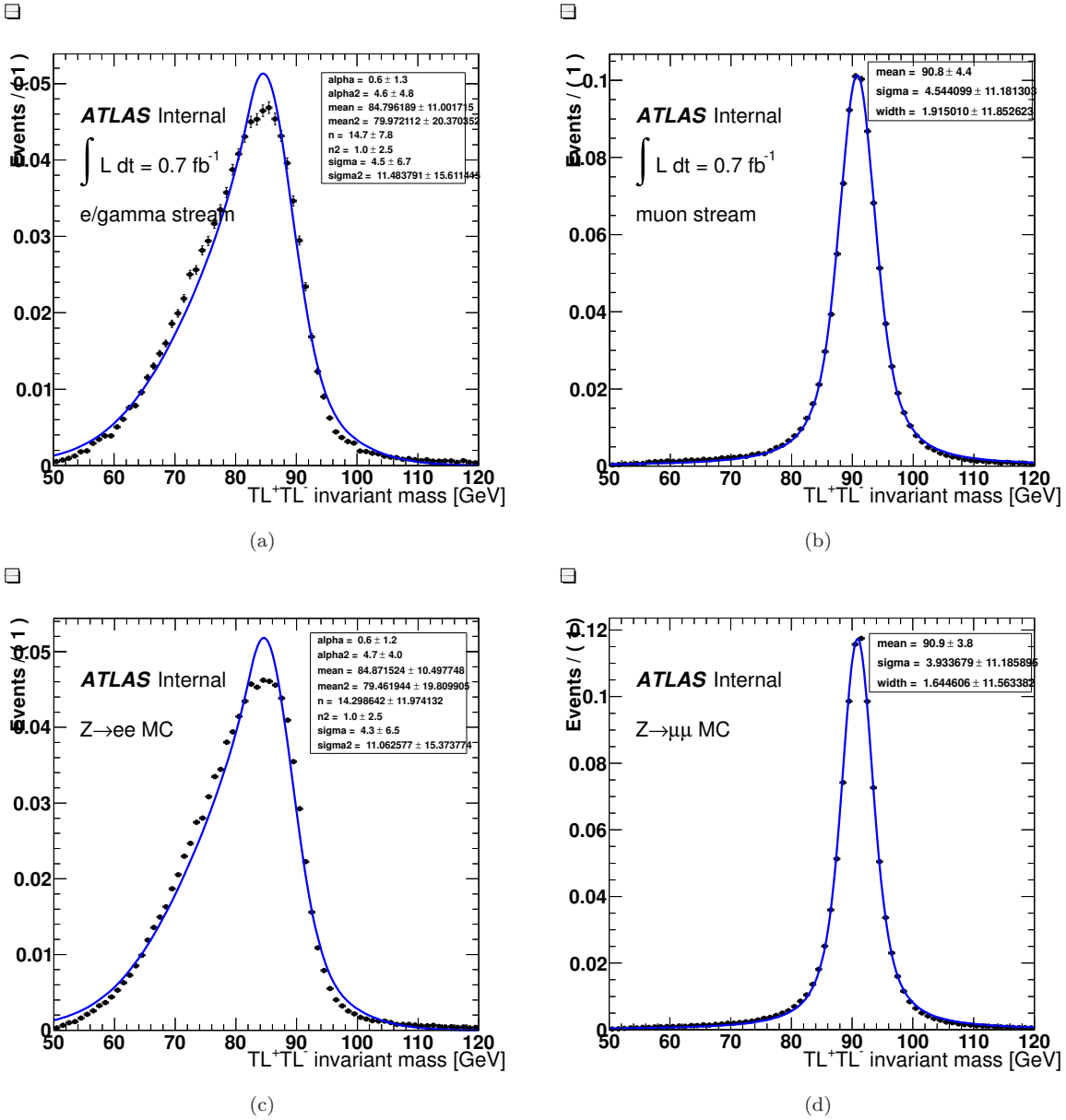

Figure 7.1: Opposite charge TLs invariant mass distributions for collisions data (top) and MC (bottom). All distributions are normalized to unity. The fit for each case is shown in blue.

Jets

The jet energy scale (JES) and its uncertainty are derived by combining information from test-beam data, LHC collision data and simulation. Uncertainties associated with the energy scale of light-quark jets and b-jets are studied as a function of the jet transverse momentum and η. For jets within the acceptance, the JES uncertainty varies in the range 4-8% as a function of jet p_T and η. This uncertainty has a contribution from pile-up. This pile-up uncertainty, in the central region is 5% for jets with $20 < p_T < 50$ GeV and 2% for jets with $50 < p_T < 100$ GeV. For forward jets, the pile-up uncertainty is 7% and 3%, in the respective p_T ranges. Additional contributions are considered to account for the flavor composition and the presence of nearby jets uncertainties. The former gives an additional uncertainty of 1.1-2.5% to b-jets with $p_T > 25$ GeV. This uncertainty increases with decreasing momentum. The effect of the jet reconstruction efficiency uncertainty is studied by randomly removing 2% of the jets from the events. The effect of potential jet resolution mis-modelling in the MC is evaluated by additional smearing of the reconstructed jet energies within the uncertainties. In each case, the difference with respect to the nominal is taken as the systematic uncertainty.

Missing Transverse Energy

The most relevant sources of systematic uncertainties in the E_T^{miss} measurement come from the scale and resolution of the objects, the description of the pile-up events, and the impact of hardware failures. All changes applied to electrons, muons and jets are propagated to the E_T^{miss} measurement. The uncertainties on the scale and resolution of the objects is propagated into E_T^{miss}, assuming a 100% correlation between the uncertainty of the objects and the E_T^{miss}. Uncertainties related to the E_T^{miss} itself are also studied. In particular, the effect of the remaining energy in the calorimeter, not associated with any reconstruction objects (Cell Out), and of low momenta (7 GeV $< p_T <$ 20 GeV) jets (Soft-Jet) is studied, as well as the uncertainty due to pile-up. Soft-Jet and Cell Out terms are scaled by their total uncertainty assuming a 100% correlation. A flat 10% uncertainty, correlated with Cell Out and Soft-Jets, is applied to account for the uncertainty due to pile-up. To account for the effects of the dead FEBs in the EM calorimeter, affecting about 42% of the total data used in the analysis, an additional systematic uncertainty, denoted LAr readout problem, is considered. It is evaluated by varying by 20% the thresholds used for removing events with the jets directed at the dead region.

7.3 WZ and ZZ Background Systematic Uncertainties

The dominant source of systematic uncertainty in the diboson background (WZ and ZZ) evaluation is due to simulation modelling. Because this is the main background in the 3ID analysis, it is correspondingly the dominant source of uncertainty there. This systematic uncertainty related to the WZ and ZZ simulation modelling was estimated using the same procedure used on W+jets MC re-weighting, based on the Berends-Giele scaling [103, 104] uncertainty of $\pm 24\%$ per jet bin, added in quadrature. These uncertainties are derived from the separate contributions to the total cross section of the subprocesses according to the number of partons. An uncertainty of $\pm 4\%$ is used for the 0-jet bin. The WZ and ZZ cross sections were varied by their theoretical uncertainty of $\pm 5\%$ [105]. In the 2ID+TL, where b-tagging was used, a systematic uncertainty associated with the heavy-flavor (HF) content of the WZ+jets and ZZ+jets is included. This is evaluated by comparing `ALPGEN` and `MC@NLO`, and is small because, as mentioned before, the main source of b-tags in these events comes from mis-tags and light-quark jets, which are well modelled in MC.

7.4 Systematic Uncertainty Evaluation for Fake TL Prediction

The systematic uncertainty on the fake lepton prediction is determined using control regions (CR) enriched in fake leptons. There, the uncertainty is set by the comparison between predicted and observed fake TLs, using the same procedure as for the fake prediction in the signal region (SR). Two different sets of CRs are used to estimate this uncertainty: lepton+jets events (denoted as W+jets in the following) with an additional fake TL, and events with two ID leptons with an additional fake TL. The former was done in the context of the dilepton $t\bar{t}$ cross section measurement [7], with a subset of the data used in this analysis, the latter is done in the context of the selection used for the 2ID+TL analysis, with the 2.05 fb^{-1} of 2011 data.

The W+jets selection was performed in 0.7 fb^{-1} of 2011 ATLAS data for the $t\bar{t}$ cross section measurement in the dilepton channel. W+jets events were selected with exactly one ID lepton (e or μ), exactly zero exclusive TLs, at least one ID jet, and $E_T^{\text{miss}} > 45$ GeV. In the signal region of ≥ 2 ID jets, the sum of transverse momenta of all ID jets and leptons in the event, H_T, had to be > 150 GeV. This sample included W+jets, single-lepton decays of $t\bar{t}$ and single top events. The sample was sub-divided according to the number of jets and, for each jet multiplicity, the fake probability was summed over all events and all ID jets. The sum of the fake probabilities for events with N jets is the predicted number of fake leptons in events with $N-1$ jets (as described in Chapter 6). In the selection performed for the cross section,

the fake prediction was scaled down by opposite-charge fractions extracted from MC, to account for the opposite-charge requirement in the signal selection. Thus, these CRs are separated into those looking at fake TLs of charge opposite to that of the ID lepton (OS), and fake TLs of same charge of the ID lepton (SS). The check for OS fake TLs was done in the ≤ 1 ID jet bins, whereas the check for SS fake TLs was done in the ≥ 2 ID jets bins. This way, the CRs remain orthogonal to the SR, and both the effect of the H_T cut (in SS events) and the OS fractions extracted from MC (in both SS and OS events) are tested. Table 7.1 shows the results of these checks. There, the column labeled 'B' shows the net background expectation, including the fake TL prediction explicitly displayed under column 'P'. This sample contained other background sources with two real leptons, like Drell-Yan, and testing the predictive power of the fake matrix required a subtraction. The other background expectation was done based on a DD normalization between MC and data expectations for the Z+jets, and using MC predictions for the rest (single top and diboson events). The last column normalizes the difference between the data observation and the net background prediction by the fake prediction only, and it was used as a measure of the fake matrix performance. The overall agreement is excellent. A conservative 20% systematic uncertainty was set on the prediction of fake TLs in the signal region, which is roughly one standard deviation above the measured deviation between the predicted and observed fakes. This 20% systematic uncertainty is inherited for the 2ID+TL analysis.

	e+fake TL				μ+fake TL			
# jets	O	B	P	(B-O)/P	O	B	P	(B-O)/P
0 (OS)	411	$436.3^{+38.4}_{-36.8}$	199.1 ± 9.3		460	$441.1^{+52.9}_{-52.0}$	321.9 ± 48.4	
1 (OS)	201	$207.1^{+16.9}_{-27.3}$	99.0 ± 4.2		247	$270.5^{+17.2}_{-16.5}$	142.5 ± 6.0	
2 (SS)	10	10.7 ± 0.8	7.6 ± 0.7		14	13.9 ± 1.0	11.1 ± 0.9	
3 (SS)	7	6.2 ± 0.5	5.4 ± 0.5		9	8.3 ± 0.7	7.0 ± 0.6	
4 (SS)	4	4.1 ± 0.4	3.8 ± 0.4		1	3.2 ± 0.4	3.1 ± 0.4	
≥ 5 (SS)	2	1.9 ± 0.1	1.8 ± 0.1		0	1.5 ± 0.2	1.4 ± 0.2	
all	635	$666.4^{+41.9}_{-45.8}$	316.6 ± 10.3	$(9.9^{+15.6}_{-16.5})\%$	731	$738.5^{+55.6}_{-54.6}$	487.0 ± 48.8	$(1.5^{+12.7}_{-12.5})\%$

Table 7.1: Comparison of predicted and observed fake TL in W+jets events. The columns labeled 'O' are the observed events in data, 'B' is the total background including non-fake backgrounds, such as Drell-Yan. and 'P' is the predicted fake TL contribution to 'B'. The last column is the total background prediction, minus the data observation, divided by the fake prediction. The uncertainties on the fakes are statistical only, whereas the uncertainties in the other background are statistical and systematic.

In the full 2.05 fb^{-1} of data, a check is made in different CRs selecting two ID leptons and one TL, but inverting or removing one or more of the other selection cuts used in the SR. The first check is done by looking at the E_T^{miss} distribution for events with three leptons (2ID+TL), exactly one jet, without b-tagging (to enhance the statistics of the sample) and with no χ^2 minimization or associated invariant mass cuts. In

the low E_T^{miss} region, 139 events are observed, compared to $147.6^{+3.5}_{-3.6}$ events predicted by the fake matrix, plus the other background sources from MC. In the high E_T^{miss} region, 74 events are observed, and $88.2^{+5.5}_{-6.0}$ predicted. The results are summarized in Table 7.2. Both of these regions are dominated by events with a fake TL and the agreement between data and expectations is good, and well within the 20% previously quoted. Figure 7.2 shows the entire E_T^{miss} distribution in this one-jet selection.

E_T^{miss} Control Region						
E_T^{miss}	ZZ and WZ	$t\bar{t}W$ and $t\bar{t}Z$	fake TL Prediction	B	O	$(B-O)/P$
≤ 20 GeV	$4.0^{+2.0}_{-2.2}$	0.01 ± 0	143.5 ± 2.8	$147.6^{+3.5}_{-3.6}$	139	$\left(\ 6.0^{+\ 8.3}_{-\ 8.4}\right)\%$
> 20 GeV	$10.8^{+5.3}_{-5.8}$	0.05 ± 0.01	77.4 ± 1.4	$88.2^{+5.5}_{-6.0}$	74	$\left(18.4^{+13.1}_{-13.4}\right)\%$

Table 7.2: The prediction and observed fake TLs in two regions of E_T^{miss} for events with exactly one jet, and without b-tagging. The last column is the total background predictions, minus the data observation, divided by the fake prediction. The uncertainties on the fakes are statistical only, whereas the uncertainties on the other background are statistical and systematic.

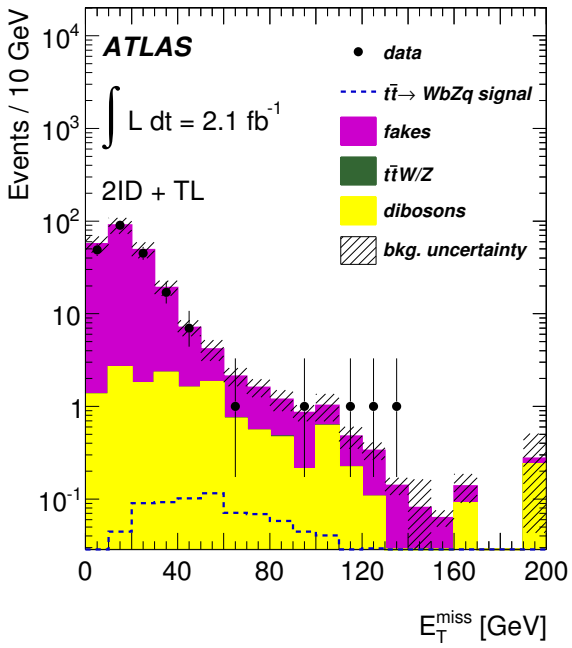

Figure 7.2: E_T^{miss} distribution in data and simulation in events with 2ID leptons, one TL and exactly one jet. The dashed line shows the shape of the signal distribution, normalized to the observed BR limit, at 95% CL. The uncertainties on the background are both statistical and systematic.

As a further cross check, other CRs are used. Events satisfying all but one of the SR selections, with that one selection inverted to provide an orthogonal CR are used. The χ^2 minimization and mass cuts are also dropped in these CRs. Events satisfying all of the event selections but with exactly one jet instead of

two or more, and events with $E_T^{\text{miss}} < 20$ GeV, are used. In events with $E_T^{\text{miss}} < 20$ GeV, 11 2ID+TL events are observed and 14.4 ± 0.4 predicted by the fake matrix, plus the other backgrounds. In one-jet events, 9 2ID+TL events are observed and $15.3^{+0.9}_{-1.0}$ predicted. The results are shown in Table 7.3, and Table 7.4 respectively. These numbers are also plotted in the first two bins of Figure 5.9(a), and the one-jet bin of Figure 5.9(b), respectively. The final column is the fractional difference between the total background prediction (including WZ, ZZ and $t\bar{t}+W/Z$ events) and the observation, normalized to the fake TL prediction.

Low E_T^{miss} Control Region						
E_T^{miss}	ZZ and WZ	$t\bar{t}W$ and $t\bar{t}Z$	fake TL Prediction	B	O	$(B-O)/P$
0-10 GeV	0.04 ± 0.02	0.01^{+0}_{-0}	4.9 ± 0.1	4.9 ± 0.1	4	
10-20 GeV	0.4 ± 0.2	$0.04^{+0.01}_{-0.01}$	9.1 ± 0.2	9.5 ± 0.3	7	
≤ 20 GeV	0.4 ± 0.2	$0.06^{+0.01}_{-0.01}$	13.9 ± 0.3	14.4 ± 0.4	11	$\left(24.7^{+23.8}_{-23.9}\right)\%$

Table 7.3: The predicted and observed fake TLs in two bins of E_T^{miss}. The last column is the total background prediction, minus the data observation, divided by the fake prediction. The uncertainties on the fakes are statistical only, whereas the uncertainties in the other background are statistical and systematic.

1 jet Control Region						
	ZZ and WZ	$t\bar{t}W$ and $t\bar{t}Z$	fake TL Prediction	B	O	$(B-O)/P$
1 jet	$1.7^{+0.8}_{-0.9}$	0.04 ± 0.01	13.6 ± 0.4	$15.3^{+0.9}_{-1.0}$	9	$\left(46.4^{+22.9}_{-23.0}\right)\%$

Table 7.4: The predicted and observed fake TLs in events with exactly one b-tagged jet. The last column is the total background prediction, minus the data observation, divided by the fake prediction. The uncertainties on the fakes are statistical only, whereas the uncertainties in the other background are statistical and systematic.

Althought the predicted minus observed is somewhat larger than the 20% uncertainty derived in the W+jets CR and the results shown in Table 7.2, it is not inconsistent given the total of only 20 events observed in this case. Thus, a 20% systematic uncertainty on the fakes prediction is used in this analysis. An additional check for TLs coming from conversions is done on MC, and it is estimated to be less than 3%. This effect should be covered by the systematic uncertainty just quoted. No additional systematic uncertainty is taken for the possible effect of b-tagging on the fake TL prediction, which might be expected due to the enhanced heavy-flavor fraction of b-tagged events. No need for this is seen in the low E_T^{miss} and one-jet CRs, and moreover consistent fake rates between data and MC for both heavy- and light-flavor jets are observed.

7.5 Other Systematic Uncertainties

The measurement of the integrated luminosity has a total uncertainty of 3.7% [72]. This uncertainty is implemented in the analysis by changing the normalization of the MC-driven SM backgrounds and signal. The uncertainties on the b-tagging efficiencies scale factors used in MC are taken into account by recomputing the predicted event yields and signal acceptance using the corresponding systematic shift. In both cases, background and signal, this is found to be 5-6%. The effect of ISR and FSR and top quark mass uncertainties are evaluated using the MC samples described in Section 4.2. For ISR and FSR, different samples are used, where each one is varied individually. Half of the maximum deviation between the different samples is taken as a systematic uncertainty. The same is done for the top mass systematic uncertainty, using the lower and higher mass samples. The effect of uncertainties in the PDF used for signal generation was evaluated by comparing the signal acceptance using `MSTW2008LO` with that from `MRST2007 LO*` PDFs.

7.6 Summary

The dominant uncertainty for the 2ID+TL analysis is the systematic uncertainty on the fake-TL prediction, because 85% of the expected background arises from this source. As explained above, this was determined to be 20% by comparing predicted and observed events with TLs in control regions dominated by fake TL. Table 7.5 shows the contribution of the different systematic uncertainty sources to the MC-based background, this is WZ, ZZ, $t\bar{t}W$ and $t\bar{t}Z$. Table 7.6 presents a summary of each uncertainty and its contribution to the net background yields and signal acceptance in the 2ID+TL analysis. Notice that most of the MC-related uncertainties are highly suppressed when normalizing to the net background, since they only contribute by 15% to it. From those systematic uncertainties, the WZ and ZZ modelling uncertainty is the most significant. A similar table for the 3ID analysis can be found in Appendix C. The 2ID+TL background evaluation has a smaller relative background systematic uncertainties in most categories, compared to the 3ID analysis, given that almost 90% of the 2ID+TL background evaluation is data-driven.

Source	MC Background
Luminosity	$\pm$ 3.7 %
Electron trigger	$\pm$ 0.3 %
Electron reconstruction	$\pm$ 0.6 %
Electron identification	$\pm$ 2.1 %
Electron energy scale	$^{+\ 0.05}_{-\ 0.01}$ %
Electron energy resolution	$^{+\ 5.5}_{-\ 0.2}$ %
Muon trigger	$\pm$ 1.1 %
Muon reconstruction	$\pm$ 0.4 %
Muon identification	$\pm$ 0.05%
Muon momentum scale	$<$ 0.01%
Muon momentum resolution	$<$ 0.01%
TL reconstruction	$\pm$ 0.2 %
TL momentum scale	$<$ 0.01%
TL momentum resolution	$\pm$10.4 %
Jet energy scale	$^{+\ 2.3}_{-18.3}$ %
Jet reconstruction	$<$ 0.01%
Jet energy resolution	$\pm$11.0 %
Cell Out and Soft-Jet	$^{+\ 0.3}_{-\ 6.8}$ %
LAr readout problem	$<$ 0.01%
Pile-up	$^{+\ 0.3}_{-\ 6.8}$ %
b-tagging	$^{+\ 4.5}_{-\ 4.6}$ %
WZ and ZZ modelling	$\pm$36.3 %
WZ and ZZ cross section	$\pm$ 4.0 %
WZ and ZZ HF content	$\pm$ 1.6 %
Total	$^{+39.1}_{-43.8}$ %

Table 7.5: Relative changes to the expected number of MC-based background events for different sources of systematic uncertainties for the 2ID+TL analysis. The contributions from the WZ and ZZ generator apply only to the simulated background samples. In cases where the quoted uncertainty is $< 0.01\%$, no change is observed in the MC samples when applying the corresponding systematic shift. In this case, the contribution to the net systematic uncertainty is taken to be zero. The $\pm$ values refer to the upper and lower systematic shifts respectively.

Source	Background	Signal
Luminosity	$\pm$ 0.5 %	$\pm$ 3.7 %
Electron trigger	$\pm$ 0.05%	$\pm$ 0.02%
Electron reconstruction	$\pm$ 0.08%	$\pm$ 0.6 %
Electron identification	$\pm$ 0.3 %	2.3 %
Electron energy scale	$^{+\ 0.01}_{-\ 0.0}$ %	$^{+\ 0.1}_{-\ 0.7}$ %
Electron energy resolution	$^{+\ 0.8}_{-\ 0.03}$ %	0.6 %
Muon trigger	$\pm$ 0.2 %	$^{+\ 0.2}_{-\ 0.3}$ %
Muon reconstruction	$\pm$ 0.05%	$\pm$ 0.4 %
Muon identification	$\pm$ 0.01%	$\pm$ 0.04%
Muon momentum scale	$<$ 0.01%	$^{+\ 0.0}_{-\ 0.01}$ %
Muon momentum resolution	$<$ 0.01%	$\pm$ 0.08%
TL reconstruction	$\pm$ 0.03%	$\pm$ 0.02%
TL momentum scale	$<$ 0.01%	$^{+\ 0.2}_{-\ 0.3}$ %
TL momentum resolution	1.5 %	$\pm$ 1.2 %
Jet energy scale	$^{+\ 0.3}_{-\ 2.6}$ %	$^{+\ 0.8}_{-\ 1.5}$ %
Jet reconstruction	$<$ 0.01%	$\pm$ 0.2 %
Jet energy resolution	1.6 %	$\pm$ 3.7 %
Cell Out and Soft-Jet	$^{+\ 0.04}_{-\ 1.0}$ %	$^{+\ 0.04}_{-\ 0.07}$ %
LAr readout problem	$<$ 0.01%	$^{+\ 0.05}_{-\ 1.0}$ %
Pile-up	$^{+\ 0.04}_{-\ 1.0}$ %	$^{+\ 0.04}_{-\ 0.0}$ %
b-tagging	$\pm$ 0.7 %	$^{+\ 5.7}_{-\ 5.9}$ %
Top quark mass	—	$\pm$ 2.8 %
$\sigma_{t\bar{t}}$	—	$^{+\ 6.7}_{-\ 9.7}$ %
ISR/FSR	—	$\pm$ 6.7 %
PDFs	—	$\pm$ 2.9 %
WZ and ZZ modelling	$\pm$ 5.3 %	—
WZ and ZZ cross section	$\pm$ 0.6 %	—
WZ and ZZ HF content	$\pm$ 0.2 %	—
Fake leptons	$\pm$17.0 %	—
Total	$^{+17.7}_{-17.9}$ %	$^{+13.6}_{-15.4}$ %

Table 7.6: Relative changes to the expected number of background events and signal yields for different sources of systematic uncertainties for the 2ID+TL analysis. The contributions from the WZ and ZZ generator apply only to the simulated background samples. In cases where the quoted uncertainty is $< 0.01\%$, no change is observed in the MC samples when applying the corresponding systematic shift. In this case, the contribution to the net systematic uncertainty is taken to be zero. The $\pm$ values refer to the upper and lower systematic shifts respectively.

Chapter 8

Limit Evaluation

8.1 Introduction

As observed in Table 6.3 and Table 6.4, for the 2ID+TL and the 3ID channel, respectively, good agreement between data and expected background is observed. No evidence for the $t \to Zq$ decay mode is found and 95% confidence level upper limits on the number of signal events are derived using the modified frequentist (CL_s) likelihood method [106]. The following description is taken from Reference [106].

8.2 The CL_s method

For searches as the one discussed in this document, where small signal rates are expected, the loss of sensitivity becomes a major issue in the interpretation of results. The CL_s method aims to avoid excluding or discovering signals which the search is in fact not sensitive to. This could be, avoiding exclusion in cases where there should be a discovery ('false exclusion'). The search results are formulated in terms of a hypothesis test. A background-only and a signal+background hypotheses are considered. Thus the result quantifies the degree to which the hypotheses are favored or excluded by the experimental observation.

In general, for the analysis of search results, a *test-statistic*, or function of the observable number of candidate events, should be defined. This serves to characterize the data with background and hypothetical signal. The ranges of values of the test-statistic in which observations will lead to an exclusion or discovery conclusion should also be defined. This is done by establishing a *confidence level* (a measure of the significance) for the exclusion or discovery to be quoted.

This test-statistic, Q, is constructed so it increases monotonically for increasingly signal-like experiments. The confidence in the signal+background hypothesis is given by the probability that the test-statistic is less

than or equal to the value observed, $Q_{\rm obs}$:

$$\mathrm{CL}_{s+b} = P_{s+b}(Q \leq Q_{\rm obs}), \tag{8.1}$$

where $P_{s+b}(Q \leq Q_{\rm obs})$ can be expressed in terms of the probability distribution function of the test-statistic, to be described below, for signal+background experiments. Small values of CL_{s+b} indicate poor compatibility with the signal+background hypothesis and favor the background-only hypothesis. In a similar way, the confidence in the background-only hypothesis is given by the probability that the test-statistic is less than or equal to the value observed:

$$\mathrm{CL}_{b} = P_{b}(Q \leq Q_{\rm obs}), \tag{8.2}$$

where $P_b(Q \leq Q_{\rm obs})$ is expressed in terms of the probability distribution of the test-statistic for background-only experiments.

The technique used by the $\mathrm{CL_s}$ method, to avoid results that are more sensitive to fluctuations of the known background than to the hypothetical signal, is to normalize the confidence level observed for the signal+background hypothesis, CL_{s+b}, to the confidence level observed in the background-only hypothesis, CL_b. This makes it possible to obtain sensible exclusion limits on the signal even if the observed rate is very low. In addition, the limits on the signal hypothesis obtained by this results will be conservative. The normalization just described is then:

$$\mathrm{CL_s} \equiv \mathrm{CL}_{s+b}/\mathrm{CL}_{b}. \tag{8.3}$$

The signal hypothesis will be then considered excluded at the confidence level CL when:

$$1 - \mathrm{CL_s} = \mathrm{CL}. \tag{8.4}$$

The consequence of $\mathrm{CL_s}$ not being a confidence, rather a ratio of confidences, is that the difference between $\mathrm{CL_s}$ and the actual false exclusion rate will increase as the probability density functions of the signal+background and background-only hypotheses become more similar. This means, the use of $\mathrm{CL_s}$ reduces the range of model parameters for which an exclusion result is possible [106, 107].

For this case, the $\mathrm{CL_s}$ method is used with a likelihood ratio as a test-statistic. The likelihood ratio, $Q(\vec{X})$, is the ratio of the probability densities for a given experimental result $\vec{X}$ for two hypothesis. This

means:

$$Q = \frac{\mathcal{L}(\vec{X}, s+b)}{\mathcal{L}(\vec{X}, b)}, \tag{8.5}$$

the ratio of probability density for the signal+background and the background-only hypotheses. The likelihood ratio for a combination of two independent channels, like the 2ID+TL and 3ID, is simply the product of the likelihood ratios of the individual channels, so the combination is straightforward. The likelihood ratio Q for an experiment with N_{channels} independent channels and measurements of a discriminating variable (number of observed events in this case) is:

$$Q = e^{-s_{\text{tot}}} \prod_{i=1}^{N_{\text{channels}}} \left(1 + \frac{s_i}{b_i}\right)^{n_i}, \tag{8.6}$$

where n_i is the number of observed candidates in each channel, and s_i and b_i are the integrated signal and background rates per channel, s_{tot} is the total signal events for all channels. Equation 8.6 follows from Poisson statistics. This can be further simplified to a form of "counting weighted events" by a simple derivation. Since $P(Q \leq Q_{\text{obs}}) = P(\ln(Q) \leq \ln(Q_{\text{obs}}))$, given that $Q \geq 0$, Equation 8.6 can ve written as:

$$\ln(Q) = -s_{\text{tot}} + \sum_{i=1}^{N_{\text{channels}}} n_i w_i \tag{8.7}$$

where n is the total number of events observed in all channels and the weight for each channel i is:

$$w_i = \ln\left(1 + \frac{s_i}{b_i}\right). \tag{8.8}$$

Since the constant s_{tot} appears in both side of the expression $\ln(Q) \leq \ln(Q_{\text{obs}})$, the final test-statistic consists basically of comparing the observed number of weighted events with the distribution expected for the signal+background and the background-only hypotheses. This is:

$$X_d = \sum_{i=1}^{N_{\text{channels}}} n_i \ln\left(1 + \frac{s_i}{b_i}\right). \tag{8.9}$$

When data events are more similar to the signal events, the X_d variable takes higher values. The X_d test-statistic is then compared to 10^5 pseudo-experiments of the hypotheses of signal+background, X_{s+b} and

background-only, X_b:

$$X_{s+b} = \sum_{i=1}^{N_{\text{channels}}} n_i^{(s+b)} \ln\left(1 + \frac{s_i}{b_i}\right), \tag{8.10}$$

$$X_b = \sum_{i=1}^{N_{\text{channels}}} n_i^{(b)} \ln\left(1 + \frac{s_i}{b_i}\right), \tag{8.11}$$

where $n_i^{(s+b)}$ and $n_i^{(b)}$ are the signal+background and background-only distributions for the expected background and signal efficiency. The resulting distributions of $-2\ln Q$ are shown in Figure 8.1.

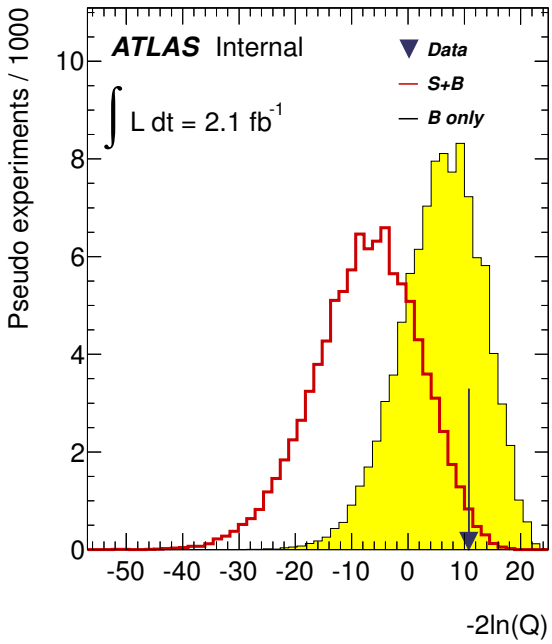

Figure 8.1: Distributions of $-2\ln Q$ obtained with 10^5 pseudo-experiments for the signal plus background hypothesis and background only hypothesis, taking into account the systematic uncertainties. The value obtained for the data sample is also indicated.

Equation 8.3 and Equation 8.4 can now be used to write the confidence level CL as:

$$1 - \text{CL} = \frac{\int_0^{X_d} P_{s+b}(X)\mathrm{d}X}{\int_0^{X_d} P_b(X)\mathrm{d}X}, \tag{8.12}$$

where P_{s+b} and P_b are the X_{s+b} and X_b distributions, respectively. The 95% CL observed limit on the number of signal events is obtained when Equation 8.12 equals 0.05. The expected limit is the one which would be obtained if the data events were perfectly described by the expected background. This expected limit is

computed from Equation 8.12 replacing X_d with the median statistical test for the background hypothesis, X_b.

8.2.1 Uncertainties

The confidence level is by itself an expression of uncertainty. Thus, instead of quoting an uncertainty on the confidence limit, the confidence limit is modified to allow for the experimental uncertainties. The approach is to create a new set of "smeared" background rates and signal efficiencies, and from these, background and signal events are generated to form the input to the likelihood ratio for each pseudo-experiment. The consequence of this smearing procedure is that the likelihood ratio distributions get widened. In particular, the background tail under the signal+background distribution and the signal+background tail under the background are enhanced. This means the overlap of the distributions is increased, reducing both the exclusion and the discovery potential of the search, and weakening both the discovery-like and exclusion-like observations [106]. In this analysis, both statistical and experimental uncertainties of the signal efficiency and expected background are taken into account, and are implemented assuming Gaussian distributions, with the lower tail cut off at zero, so that negative signal or background are not allowed. In addition, the statistical fluctuations of the pseudo-experiments are performed using Poisson distributions. Poisson statistics are required given that expected signal and background levels are small. For the combination of the 2ID+TL and 3ID channels the systematic uncertainty of the MC-based backgrounds (WZ, ZZ and $t\bar{t}+W/Z$) and signal acceptance are considered to be fully correlated, while other sources of uncertainties (statistical or systematic) are considered uncorrelated.

8.3 Results

The limits on number of signal events expected are then converted into upper limit on the corresponding BRs using the approximate NNLO calculation, and its uncertainty, for the $t\bar{t}$ cross section ($\sigma_{t\bar{t}} = 165^{+11}_{-16}$ pb) [108]. This is simply achieved with the use of the cross section definition:

$$\sigma_{t\bar{t}} = \frac{N_{t\bar{t}}}{\int L\mathrm{d}t}, \tag{8.13}$$

where $N_{t\bar{t}}$ is the number of collision events that produce $t\bar{t}$ events, and constraining $\mathrm{BR}(t \to Zq)$ by:

$$\mathrm{BR}(t \to Zq) + \mathrm{BR}(t \to Wq) = 1. \tag{8.14}$$

channel	observed	(-1σ)	expected	$(+1\sigma)$
3ID	0.81%	0.63%	0.95%	1.42%
2ID+TL	3.18%	2.15%	3.31%	4.86%
Combination	0.73%	0.61%	0.93%	1.36%

Table 8.1: The observed 95% CL upper limits on the FCNC top quark decay $t \to Zq$ branching fraction are shown. The $\pm 1\sigma$ expected limits, which include both the statistical and the systematic uncertainties, are also presented.

The observed 95% CL limit on the FCNC $t \to Zq$ BR is 3.2% (0.8%) taking the 2ID+TL (3ID) events and background evaluation alone, and 0.7% when the 2ID+TL and 3ID results are combined. The observed and expected limits in the absence of signal are shown in Table 8.1, along with the $\pm 1\sigma$ expected limits.

Chapter 9

Conclusions

A search for flavor changing neutral currents in top quark decay has been presented. 2.1 fb^{-1} of 2011 pp collision data at a center-of-mass energy of $\sqrt{s} = 7$ TeV collected by the ATLAS experiment have been used for this analysis. The $t \to Zq$ decay mode was searched for on events with top quarks produced in pairs, $t\bar{t}$, with one top quark decaying according to the SM and the other according to the FCNC ($t\bar{t} \to WbZq$). Two orthogonal channels were introduced, 2ID+TL and 3ID, and the individual results presented. The final result, combining both channels, has been presented. No evidence for FCNC signal in top quark decays has been found, and an upper limit on the $t \to Zq$ branching ratio of BR($t \to Zq$) $< 0.73\%$ is set at the 95% CL, assuming BR($t \to Wb$)+BR($t \to Zq$) = 1. This observed limit is in agreement with the expected sensitivity, assuming that the data are described correctly by the SM, of BR($t \to Zq$) $< 0.93\%$.

This search was performed in subset of the available 2011 $\sqrt{s} = 7$ TeV pp collisions data collected in 2011. Moreover, in 2012, more than 5 fb^{-1} of $\sqrt{s} = 8$ TeV pp collision data have been collected by now. The analysis can greatly benefit from the addition of these data. A future expansion of this analysis can be done not only by adding more data, but also by including other decay channels. This is, either including other FCNC top quark decays, presented in Figure 2.6, or including non-leptonic decays of the W- and/or the Z-boson. The latter, compared to the three-lepton channel, requires a better understanding of the background, given that the processes where hadronic decays of the bosons are involved introduce a much larger multijet background. In such case the selection would need to be modified and optimized for that. However, in the case when the W-boson only is allowed to decay hadronically, the two charged leptons from the Z-boson would provide a relatively clean sample, and since there is no neutrino in the final state, the W-boson should be, in principle, directly reconstructed within the analysis.

With the current result, no conclusions can be drawn on any of the physics models presented in Chapter 2. If, with the addition of more data or the inclusion of other channels, significant evidence for a FCNC signal was found, a statement on those models, and on the coupling constants introduced along, can be done.

Appendix A

γ+jets Event Selection

The γ+jets data sample used for the fake matrix construction covers the same data periods as the dataset used for the rest of the analysis. Because of the photon trigger prescales these data comprise only about 0.10 fb^{-1}, after implementing the e-gamma performance group good run list selection. Events are selected from the e-gamma data stream using (an OR logic of) the following triggers: `EF_g20_loose` and `EF_g40_loose`. Events satisfying the trigger requirement were further selected by requiring a photon with:

- $p_T(\gamma) > 25$ GeV,
- Quality: tight photon,
- Fiducial region: $|\eta| < 2.37$, and exclude the crack region: $1.37 < |\eta| < 1.52$,
- Calorimeter isolation: sum E_T in a cone of $\Delta R < 0.4$ must be < 2.5 GeV [1],
- One jet ($p_T > 25$ GeV, $|\eta| < 2.5$) within $\Delta R < 0.1$, with high EM fraction [2],
- Object-quality[3] check for photons.
- Z-boson veto.

Once the photon (exactly one per event) has been identified, all objects (jets and leptons) within $\Delta R < 0.2$ are removed, and not used in the fake rate matrix construction. The Z-boson veto is needed to suppress contamination from $Z \to e^+e^-$ events, where the track associated with one electron has not been attached to the electromagnetic cluster. We therefore removed events if the putative photon and an ID electron have an invariant mass between 81 and 101 GeV, or the photon and a TL have an invariant mass between 78 and 98 GeV. The lower window for the photon-TL pair results from the unaccounted for radiation from the track.

[1] After corrections for leakage, and pile-up.
[2] This is the ratio of energy deposited in the EM calorimeter, over the energy deposited in both EM and hadronic calorimeters.
[3] As described for electrons in Section 5.3.2, quality requirements on the conditions of the EM calorimeter at the time of data taking are applied. In this case, the requirements are optimized for photon selection.

There are a total of 666236 γ+jets events with 701589 jets used in the fake matrix denominator, and a total of 1409 TLs in the numerator, as shown in Table A.1 and Table A.2 respectively. Figure A.1 shows the η distribution of the photon in the events selected, and the ΔR between the photon and the jets used in the fake rate matrix denominator.

ID jets, and jet-elements					
1	18241	12151	6734	3462	64302
2	48857	32799	18569	9372	
3	67159	44579	25380	126895	
4	62529	41088	23290	11679	
5	44505	28619	16436	8322	
6	25755	16383	9264	4750	
7	12522	7649	4460	2265	
≥ 8	17779				
(p_T, N_{PVX})	[25 - 40] GeV	[40 - 55] GeV	[55 - 70] GeV	[70 - 85] GeV	$\geq$85 GeV

Table A.1: Fake matrix denominator.

fakes					
1	85	23	12	2	15
2	189	60	11	3	
3	242	64	24	5	
4	237	50	17	6	
5	138	39	12	4	
6	76	11	7	2	
7	39	9	1	2	
≥ 8	24				
(p_T, N_{PVX})	[25 - 40] GeV	[40 - 55] GeV	[55 - 70] GeV	[70 - 85] GeV	$\geq$85 GeV

Table A.2: Fake matrix numerator.

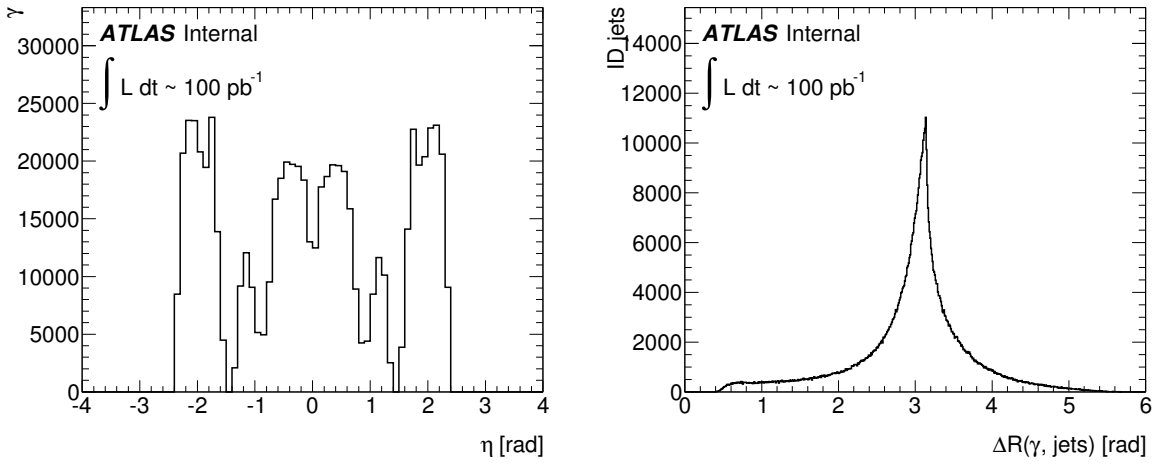

(a) (b)

Figure A.1: (a) η distribution of photons selected from data, (b) ΔR distribution between the photon and the jets ($p_T > 25$ GeV, $|\eta| < 2.5$) used in the fake rate matrix construction.

Appendix B

Backgrounds to the 3ID analysis

B.1 Monte Carlo Background

Similarly to what is done for the 2ID+TL analysis, the background coming from diboson (WW and ZZ) plus jets and $t\bar{t} + W/Z$ are estimated from MC simulation.

B.2 Fake Leptons Background

Background to the 3ID candidate events in which at least one jet is reconstructed as a lepton is separated in two categories: background events with one fake lepton, and background events with two or three fake leptons. Background events with one fake lepton are evaluated using a combination of data and MC samples. The Z+jets background is estimated using a DD normalization to the MC estimate. Z+jets, along with other sources of one fake lepton background, are evaluated at the final selection level using a loose lepton reconstruction selection and a multiplicative factor to scale to the final selection. This loose selection is achieved by relaxing the leptons requirements. Loose muons are defined as in Section 5.3.1, but without the isolation requirement. Loose electrons are obtained with the selection described in Section 5.3.2, but relaxing the isolation requirement to < 6 GeV. Events with two fake leptons (such as W+jets and single lepton $t\bar{t}$ events) or three fake leptons (such as multijet and hadronic $t\bar{t}$ events) are estimated with DD methods.

To enhance the statistical power of the MC samples, the background with one fake lepton is estimated with the loose lepton selection described above. A multiplicative factor of 0.063 ± 0.013, corresponding to the MC probability for events with loose leptons to pass the signal region (SR) lepton criteria, is applied to the final results in each of the background sources.

The dominant contribution to events with one fake lepton comes from Z+jets events, with a leptonic

Z-boson decay, in which one of the jets is misidentified as the third lepton. To evaluate this background a DD method was developed. This method uses a control region (CR) in the $(E_T^{\text{miss}}, m_{\ell\ell})$ plane by selecting events with two opposite-charge electrons or muons with invariant mass satisfying $|91.19\text{ GeV} - m_{\ell\ell}^{\text{reco}}| < 15$ GeV. This is done in six different regions of E_T^{miss}, from 0 GeV to $\geq$50 GeV. The Z+jets estimate in the SR, in each E_T^{miss} bin, is simply given by:

$$\left[N_{Z+\text{jets}}^{\text{data}}\right]_{\text{SR}} = \left[\frac{N^{\text{data}} - N_{\text{other bkg.}}^{\text{MC}}}{N_{Z+\text{jets}}^{\text{MC}}}\right]_{\text{CR}} \cdot \left[N_{Z+\text{jets}}^{\text{MC}}\right]_{\text{SR}}. \tag{B.1}$$

For each E_T^{miss} bin considered, the corresponding normalization factor (background-subtracted data to simulation ratio in the CR) is obtained and applied to the simulated Z+jets background in the SR. Applying the multiplicative factor quoted above, this gives the expected number of Z+jets events in the data. The contribution of the remaining processes to the one fake lepton background (dileptonic $t\bar{t}$, Wt-channel single top, WW production) is evaluated using MC simulation samples with the loose lepton selection and the scale factor from above.

A DD method was developed to evaluate the contribution from multijet, W+jets, single top and $t\bar{t}$ single lepton decay events, in which two or three jets are reconstructed as leptons (2+3 fake leptons). Due to the requirements that two leptons should have the same flavor and opposite charges, the yield from these background sources can be extrapolated from the number of observed data events with three leptons of any flavor (e and μ), but with the same charge. Taking into account the possible charge and flavor combinations, there are 36 combinations of three leptons, in which two have the same flavor and opposite charges, and 16 combinations of three leptons with the same charge. The extrapolation factor is thus $f = 36/16 = 2.25$. No data events passed the selection after requiring three leptons with the same charge. The uncertainties in the DD backgrounds are determined using the Feldman-Cousins upper interval for a 68% CL [109] with no observed events (with the uncertainties multiplied by 2.25 for the 2+3 fake leptons sample). Since no events with three leptons of the same charge are selected, a multiplicative factor of 0.07 ± 0.018, to account for the final requirements of at least two ID jets and $E_T^{\text{miss}} > 20$ GeV, is evaluated using MC and applied to the uncertainty estimate.

The yields of the expected background and the data observation for the final selection of the 3ID selection were presented in Chapter 6.

Appendix C

Systematic Uncertainties in the 3ID analysis

For the 3ID channel the dominant source of systematic uncertainty is the ZZ and WZ simulation modelling. Other sources have effects at most of the same magnitude as the statistical uncertainty. Table C.1 shows a summary of the different uncertainties and their contribution to the net background yields and signal acceptance in the 3ID analysis.

Source	Background	Signal
Luminosity	$\pm 4\%$	$\pm 4\%$
Electron trigger	$^{+5}_{-3}\%$	$\pm 1\%$
Electron reconstruction	$^{+1}_{-2}\%$	$\pm 1\%$
Electron identification	$^{+4}_{-6}\%$	$^{+1}_{-2}\%$
Electron energy scale	$^{+3}_{-6}\%$	$\pm 1\%$
Electron energy resolution	$\pm 7\%$	$\pm 1\%$
Muon trigger	$\pm 3\%$	$\pm 1\%$
Muon reconstruction	$^{+1}_{-4}\%$	$< 1\%$
Muon identification	$\pm 1\%$	$< 1\%$
Muon energy scale	$^{+5}_{-3}\%$	$\pm 1\%$
Muon energy resolution	$\pm 5\%$	$< 1\%$
Jet energy scale	$^{+\ 9}_{-12}\%$	$\pm 2\%$
Jet reconstruction	$\pm 5\%$	$\pm 2\%$
Jet energy resolution	$\pm 1\%$	$\pm 3\%$
Cell-Out and Soft-Jet	$\pm 4\%$	$\pm 1\%$
LAr readout problem	$^{+2}_{-4}\%$	$\pm 1\%$
Pile-up	$^{+5}_{-2}\%$	$< 1\%$
Top quark mass	$< 1\%$	$^{+1}_{-2}\%$
$\sigma_{t\bar{t}}$	$< 1\%$	$^{+\ 7}_{-10}\%$
ISR/FSR	$< 1\%$	$\pm 3\%$
PDFs	—	$\pm 3\%$
WZ and ZZ modelling	$\pm 33\%$	—
WZ and ZZ cross section	$\pm 4\%$	—
Total	$\pm 38\%$	$\pm 12\%$

Table C.1: Absolute values of the relative changes o the expected number of background events and signal yields for different sources of systematic uncertainties for the 3ID analysis. The contributions from the WZ and ZZ generator apply only to the simulated background samples. The $\pm$ values refer to the upper and lower systematic shifts respectively.

References

[1] J. L. Borges, *Tres versiones de Judas (Three versions of Judas)*, Ficciones (1994).

[2] **CDF** and **D0** Collaboration, *Combination of CDF and D0 results on the mass of the top quark using up to 5.8 fb^{-1} of data*, FERMILAB-TM-2504-E, [arXiv:1107.5255].

[3] F. del Aguila, J. A. Aguilar-Saavedra and R. Miquel, *Constraints on top couplings in models with exotic quarks*, Phys. Rev. Lett. **82** (1999) 1628, [hep-ph/9808400].

[4] **D0** Collaboration, *Search for flavor changing neutral currents in decays of top quarks*, Phys. Lett. B **701** (2011) 313-320, [arXiv:1103.4574].

[5] **CDF** Collaboration, *A Measurement of the $t\bar{t}$ Cross Section in $p\bar{p}$ Collisions at $\sqrt{s} = 1.96$ TeV using Dilepton Events with a Lepton plus Track Selection*, Phys. Rev. D **79** (2009) 112007, [arXiv:0903.5263].

[6] **ATLAS** Collaboration, *Measurement of the top quark pair production cross section in pp collisions at $\sqrt{(s)} = 7$ TeV in dilepton final states with ATLAS*, Phys. Lett. B **707** (2012) 459-477, [arXiv:1108.3699].

[7] **ATLAS** Collaboration, *Measurement of the cross section for top-quark pair production in pp collisions at $\sqrt{s} = 7$ TeV with the ATLAS detector using final states with two high-p_T leptons*, JHEP **1205** (2012) 059, [arXiv:1202.4892].

[8] **ATLAS** Collaboration, *A search for flavour changing neutral currents in top-quark decays in pp collision data collected with the ATLAS detector at $\sqrt{s} = 7$ TeV*, Submitted to JHEP (2012), [arXiv:1206.0257].

[9] **CDF** Collaboration, *Evidence for Top Quark Production in $\bar{p}p$ Collisions at $\sqrt{s} = 1.8$ TeV*, Phys. Rev. Lett. **73** (1994) 225-231, [hep-ex/9405005]. Phys. Rev. **D50**, 2966-3026 (1994).

[10] **CDF** Collaboration, *Observation of Top Quark Production in $\bar{p}p$ Collisions*, Phys. Rev. Lett. **74** (1995) 2626-2631, [hep-ex/9503002].

[11] **D0** Collaboration, *Observation of Top Quark*, Phys. Rev. Lett. **74** (1995) 2632-2637, [hep-ex/9503003].

[12] S. L. Glashow, *Partial Symmetries of Weak Interactions*, Nucl. Phys. **22** (1961) 579-588.

[13] A. Salam and J. C. Ward, *Electromagnetic and Weak Interaction*, Phys. Lett. **13** (1964) 168.

[14] A. Salam, *Weak and electromagnetic interactions*, in "Elementary Particle Theory", ed N. Svartholm, Stockholm (1968).

[15] S. Weinberg, *A model of Leptons*, Phys. Rev. Lett. **19** (1967) 1264-1266.

[16] F. Halzen and A. D. Martin, *Quarks and Leptons : An Introductory Course in Modern Particle Physics*, New York, NY, Wiley (1984).

[17] D. H. Perkins, *Introduction to High Energy Physics*, 4th Edition. Cambridge Univ. Press (2000).

[18] C. Quigg, *Gauge theories of the strong, weak, and electromagnetic interactions*, Reading, MA, Addison-Wesley (1983).

[19] A. Straessner, *Electroweak Physics at LEP and LHC*, Berlin, Springer (2010).

[20] **Particle Data Group** Collaboration, *Review of Particle Physics*, Phys. Rev. **D86** (2012) 010001.

[21] **ATLAS** Collaboration, *Statistical combination of top quark pair pair production cross-section measurements using dilepton, single-lepton, and all-hadronic final states at* $\sqrt{s} = 7$ *TeV with the ATLAS detector*, `ATLAS-CONF-2012-024`. http://cdsweb.cern.ch/record/1430733.

[22] **CMS** Collaboration, *Combination of top pair production cross section measurements*, `CMS-PAS-TOP-11-024`. http://cdsweb.cern.ch/record/1401250.

[23] S. L. Glashow, J. Iliopoulos and L. Maiani, *Weak Interactions with lepton-hadron symmetry*, Phys. Rev. **D2** (1970) 1285.

[24] J. A. Aguilar-Saavedra and B. M. Nobre, *Rare Top Decays* $t \to c\gamma, t \to cg$ *and CKM Unitarity*, Phys. Lett. B **553** (2003) 251-260, [hep-ph/0210360].

[25] J. A. Aguilar-Saavedra, *Effects of mixing with quark singlets*, Phys. Rev. **D67** (2003) 035003, [hep-ph/0210112]. Erratum-ibid. **D35** (1987) 3484.

[26] T. P. Cheng and M. Sher, *Mass Matrix Ansatz and Flavor Nonconservation in Models with Multiple Higgs Doublets*, Phys. Rev. **D35** (1987) 3484.

[27] B. Grzadkowski, J. F. Gunion and P. Krawczyk, *Neutral current flavor changing decays for the Z boson and the top quark in two Higgs doublet models*, Phys. Lett. **B268** (1991) 106.

[28] M. E. Luke and M. J. Savage, *Flavor changing neutral currents, weak-scale scalars and rare top decays*, Phys. Lett. **B307** (1993) 387, [hep-ph/9303249].

[29] D. Atwood, L. Reina and A. Soni, *Probing flavor changing top-charm-scalar interactions in* e^+e^- *collisions*, Phys. Rev. **D53** (1996) 1199, [hep-ph/9506243].

[30] D. Atwood, L. Reina and A. Soni, *Phenomenology of two Higgs doublet models with flavor changing neutral currents*, Phys. Rev. **D55** (1997) 3156, [hep-ph/9609279].

[31] S. Bejar, J. Guasch and J. Sola, *Loop induced flavor changing neutral decays of the top quark in a general two-Higgs-doublet model*, Nucl. Phys. **B600** (2001) 21, [hep-ph/0011091].

[32] C. S. Li, R. J. Oakes and J. M. Yang, *Rare decays of the top quark in the minimal supersmmetric model*, Phys. Rev. **D49** (1994) 293. Erratum-ibid. **D56** (1997) 3156.

[33] G. M. de Divitiis, R. Petronzio and L. Silvestrini, *Flavor changing top decays in supersymmetric extensions of the standard model*, Nucl. Phys. **B504** (1997) 45, [hep-ph/9704244].

[34] J. L. Lopez, D. V. Nanopoulos and R. Rangarajan, *New supersymmetric contributions to* $t \to cV$, Phys. Rev. **D56** (1997) 3100, [hep-ph/9702350].

[35] J. Guasch and J. Sola, *FCNC top quark decays: A door to SUSY physics in high luminosity colliders?*, Nucl. Phys. **B562** (1999) 3, [hep-ph/9906268].

[36] D. Delepine and S. Khalil, *Top flavor violating decays in general supersymmetric models*, Phys. Lett. **B599** (2004) 62, [hep-ph/0406264].

[37] J. J. Liu, C. S. Li, L. L. Yang, $t \to cV$ *via SUSY FCNC coupling in the unconstraint MSSM*, Phys. Lett. **B599** (2004) 92, [hep-ph/0406155].

[38] J. J. Cao et al., *SUSY induced FCNC top-quark processes at the Large Hadron Collider*, Phys. Rev. **D75** (2007) 075021, [hep-ph/0702264].

[39] J. M. Yang, B. L. Young and X. Zhang, *Flavor-changing top quark decays in R-parity violating SUSY*, Phys. Rev. **D58** (1998) 055001, [hep-ph/9705341].

[40] G. Lu, F. Yin, X. Wang and L. Wan, *The rare top quark decays $t \to cV$ in the topcolor-assisted technicolor model*, Phys. Rev. **D68** (2007) 015002, [hep-ph/0303122].

[41] G. P. L. Agashe and A. Soni, *Flavor structure of warped extra dimension models*, Phys. Rev. **D71** (2005) 016002, [hep-ph/0408134].

[42] G. P. L. Agashe and A. Soni, *Collider Signals of Top Quark Flavor Violation from a Warped Extra Dimension*, Phys. Rev. **D75** (2007) 015002, [hep-ph/0606293].

[43] J. A. Aguilar-Saavedra, *Top flavour-changing neutral interactions: theoretical expectations and experimental detection*, Acta Phys. Polon. **B35** (2004) 2695-2710, [hep-ph/0409342].

[44] M. Beneke et al., *Top Quark Physics, in: Proceedings of the "1999 CERN Workshop on SM Physics (and More) at the LHC"*, (2000), [hep-ph/0003033].

[45] **ALEPH** Collaboration, *Search for Single Top Production in e^+e^- Collisions at $\sqrt{s}$ up to 209 GeV*, Phys. Lett. B **543** (2002) 173-182, [hep-ex/0206070].

[46] **DELPHI** Collaboration, *Search for single top production via FCNC at LEP at $\sqrt{s} = 189 - 208$ GeV*, Phys. Lett. B **590** (2004) 21-34, [hep-ex/0404014].

[47] **OPAL** Collaboration, *Search for single top quark production at LEP2*, Phys. Lett. B **521** (2001) 181-194, [hep-ex/0110009].

[48] **L3** Collaboration, *Search for single top production at LEP*, Phys. Lett. B **549** (2002) 290-300, [hep-ex/0210041].

[49] The LEP Exotica WG, *Search for single top production via flavour changing neutral currents: Preliminary Combined Results of the LEP Experiments*, (2001) `LEP Exotica WG WG 2001-01`.

[50] **H1** Collaboration, *Search for Single Top Quark Production at HERA*, Phys. Lett. B **678** (2009) 450-458, [arXiv:0904.3876].

[51] **ZEUS** Collaboration, *Search for single-top production in ep collisions at HERA*, Phys. Lett. B **559** (2003) 153-170, [hep-ph/0302010].

[52] A. A. Ashimova and S. R. Slabospitsky, *The constraint on FCNC coupling of the top quark with a gluon from ep collisions*, Phys. Lett. B **668** (2008) 282-285, [hep-ph/0604119].

[53] **H1** Collaboration, *Search for single top quark production in ep collisions at HERA*, Eur. Phys. J. C **33** (2004) 9-22, [hep-ph/0310032].

[54] **CDF** Collaboration, *Search for flavor-changing neutral currents decays of the top quark in $p\bar{p}$ collisions at $\sqrt{s} = 1.8$ TeV*, Phys. Rev. Lett. **80** (1998) 2525-2530.

[55] **D0** Collaboration, *Search for flavor changing neutral currents via quark-gluon couplings in single top quark production using 2.3 fb^{-1} of $p\bar{p}$ collisions*, Phys. Lett. B **693** (2010) 81-87, [arXiv:1006.3575].

[56] **ATLAS** Collaboration, *Search for FCNC single top-quark production at $\sqrt{s} = 7$ TeV with the ATLAS detector*, Phys. Lett. B **712** (2012) 351-369, [arXiv:1203.0529].

[57] **CDF** Collaboration, *Search for the Flavor Changing Neutral Current Decay $t \to Zq$ in $p\bar{p}$ collisions at $\sqrt{s} = 1.96$ TeV*, Phys. Rev. Lett. **101** (2008) 192002, [arXiv:0805.2109].

[58] R. Guedes, R. Santos and M. Won, *top FCNC physics at a Linear Collider after the LHC*, `SHEP-10-21`, [arXiv:1007.2992].

[59] **ATLAS** Collaboration, *Observation of an Excess of Events in the Search for the Standard Model Higgs boson with the ATLAS detector at the LHC*, `ATLAS-CONF-2012-093` (2012).

[60] Lyndon Eans, Philip Bryant, *LHC Machine*, JINST 3 (2008) S08001.

[61] **ATLAS** Collaboration, *LHC Design Report*, Volume **I**: The LHC Main Ring, CERN/2004/003/V-1, (2004).

[62] **ATLAS** Collaboration, *LHC Design Report*, Volume **II**: The LHC Infrastructure and General Services, CERN/2004/003/V-2, (2004).

[63] **ATLAS** Collaboration, *LHC Design Report*, Volume **II**: The LHC Injection Chain, CERN/2004/003/V-3, (2004).

[64] **ATLAS** Collaboration, *The ATLAS Experiment at the CERN Large Hadron Collider*, JINST 3 (2008) S08003.

[65] **ATLAS** Collaboration, *ATLAS Detector and Physics Performance Technical Design Report*, Volume **I**, CERN/LHCC/99-14, ATLAS TDR 14, (1999).

[66] **ATLAS** Collaboration, *ATLAS Magnet System Technical Design Report*, CERN/LHCC/97-18, ATLAS TDR 6, (1997).

[67] **ATLAS** Collaboration, *ATLAS Inner Detector Technical Design Report*, Volume **I**, CERN/LHCC/97-16, ATLAS TDR 4, (1997).

[68] **ATLAS** Collaboration, *ATLAS Calorimeter Performance Technical Design Report*, CERN/LHCC/96-40, ATLAS TDR 1, (1996).

[69] **ATLAS** Collaboration, *ATLAS Muon Spectrometer Technical Design Report*, CERN/LHCC/97-22, ATLAS TDR 10, (1997).

[70] **ATLAS** Collaboration, *Luminosity Determination in pp Collisions at* $\sqrt{s} = 7$ *TeV Using the ATLAS Detector at the LHC*, [arXiv:1101.2185].

[71] S. van der Meer, *Calibration of the effective beam height in the ISR*, CERN-ISR-PO-68-31 (1968).

[72] **ATLAS** Collaboration, *Updated Luminosity Determination in pp Collisions at* $\sqrt{s} = 7$ *TeV using the ATLAS Detector*, ATLAS-CONF-2011-011 (2011).

[73] **ATLAS** Collaboration, *First Level Trigger Technical Design Report*, CERN/LHCC/98-014, Atlas TDR 12, (1998).

[74] **ATLAS** Collaboration, *ATLAS DAQ, EF, LVL2 and DCS: Technical progress report*, CERN/LHCC/98-016, (1998).

[75] **ATLAS** Collaboration, *The ATLAS simulation infrastructure*, Eur. Phys. J. **C70** (2010) 823, [arXiv:1005.4568].

[76] T. Sjostrand, S. Mrenna and PSkands, *PYTHIA 6.4 physics and manual*, JHEP **05** (2006) 026, [hep-ph/0603175].

[77] S. Agostinelli et al., *GEANT4-a simulation toolkit*, Nucl. Instr. Meth. **A506** (2003) 250.

[78] S. R. Slabospitsky and L. Sonnenschein, *TopRex generator (version 3.25): Short manual*, Comput. Phys. Commun. **148** (2002) 87-102, [hep-ph/0201292].

[79] A. Sherstnev and R. Thorne, *Parton Distributions for LO Generator*, Eur. Phys. J. **C55** (2008) 553, [arXiv:0711.2473].

[80] B. P. Kersevan and E. Richter-Was, *The Monte Carlo event generator AcerMC version 2.0 with interfaces to PYTHIA 6.2 and HERWIG 6.5*, [hep-ph/0405247].

[81] P. Skands, *Tuning Monte Carlo Generators: The Perugia Tunes*, Phys. Rev. **D32** (2010) 0074018.

[82] **ATLAS** Collaboration, *Expected Performance of the ATLAS Experiment - Detector, Trigger and Physics*, CERN-OPEN-2008-020 (2008).

[83] M. L. Mangano, M. Moretti, F. Piccinni, R. Pittau and A. D. Polosa, *ALPGEN, a generator for hard multiparton processes in hadronic collisions*, JHEP **07** (2003) 001.

[84] J. Pumplin et al., *New generation of parton distributions with uncertainties from global QCD analysis*, JHEP **07** (2002) 012.

[85] G. Corcella et al., *HERWIG 6.5: an event generator for Hadron Emission Reactions With Interfering Gluons (including supersymmetric processes)*, JHEP **01** (2001) 010.

[86] G. Corcella et al., *HERWIG 6.5 release note*, [hep-ph/0210213].

[87] J. M. Butterworth, J. R. Forshaw and M. H. Seymour, *Multiparton interactions in photoproduction at HERA*, Z. Phys. **C72** (1996) 637, [hep-ph/9601371].

[88] **ATLAS** Collaboration, *First tuning of HERWIG/JIMMY to ATLAS data*, `ATLAS-PHYS-PUB-2010-014`. http://cdsweb.cern.ch/record/1303025.

[89] J. Alwall et al., *Comparative study of various algorithms for the merging of parton showers and matrix elements in hadronic collisions*, Eur. Phys. J. **C53** (2008) 473-500, [arXiv:0706.2569].

[90] S. Frixione and B. R. Webber, *Matching NLO QCD computations and parton shower simulations*, JHEP **06** (2002) 029, [hep-ph/0204244].

[91] S. Frixione, P. Nason and B. R. Webber, *Matching NLO QCD and parton showers in heavy flavour production*, JHEP **08** (2003) 007, [hep-ph/0305252].

[92] S. Frixione, E. Laenen, P. Motylinski and B. R. Webber, *Single-top production in MCNLO*, JHEP **03** (2006) 092, [hep-ph/0512250].

[93] P. M. Nadolsky et al., *Implications of CTEQ global analysis for collider observables*, Phys. Rev. **D78** (2008) 013004, [arXiv:0802.0007].

[94] M. Aliev et al., *HATHOR - HAdronic Top and Heavy quarks crOss section calculatoR*, Comput. Phys. Commun. **182** (2011) 1034.

[95] N. Kidonakis, *Net-to-next-to-leading-order collinear and soft gluon corrections for t-channel single top quark production*, Phys. Rev. **D83** (2011) 091503, [arXiv:1103.2792].

[96] N. Kidonakis, *NNLL resummation for s-channel single top quark production*, Phys. Rev. **D81** (2010) 054028, [arXiv:1001.5034].

[97] N. Kidonakis, *Two-loop soft anomalous dimensions for single top quark associated production with a W- or H-*, Phys. Rev. **D82** (2010) 054018, [arXiv:1005.4451].

[98] J. Alwall at al., *MadGraph/MadEvent v4: The New Web Generation*, JHEP **0709** (2007) 028, [arXiv:0706.2334].

[99] M. Cacciari, G. P. Salam and G. Soyez, *The anti-kt jet clustering algorithm*, JHEP **0804** (2008) 063.

[100] **ATLAS** Collaboration, *Jet energy measurement with the ATLAS detector in proton-proton collisions at $\sqrt{s} = 7$ TeV*, Submitted to Eur. Phys. J, [arXiv:1112.6426].

[101] **ATLAS** Collaboration, *Commissioning of the ATLAS high-performance b-tagging algorithms in the 7 TeV collision data*, `ATLAS-CONF-2011-102`. http://cdsweb.cern.ch/record/1369219.

[102] **ATLAS** Collaboration, *Data-Quality Requirements and Event Cleaning for Jets and Missing Transverse Energy Reconstruction with the ATLAS Detector in Proton-Proton Collisions at a Center-of-Mass Energy of $\sqrt{s} = 7$ TeV*, `ATLAS-CONF-2010-038`. https://cdsweb.cern.ch/record/1277678.

[103] F. A. Berends, H. Kuijf, B. Tausk and W. T. Giele, *On the Production of a W and Jets at Hadron Colliders*, Nucl. Phys. B **357** (1991) 32-64.

[104] S. D. Ellis, R. Kleiss and W. J. Stirling, *W's, Z's and Jets*, Phys. lett. B **154** (1985) 435.

[105] J. M. Campbell and R. K. Ellis, *MCFM for the Tevatron and the LHC*, Nucl. Phys. Proc. Suppl. **205** (2010) 10.

[106] A. L. Read, *Modified frequentist analysis of search results (The CL(s) method)*, CERN-OPEN-2000-205. Prepared for Workshop on Confidence Limits, Geneva, Switzerland, 17-18 Jan 2000.

[107] T. Junk, *Confidence Level Computation for Combining Searches with Small Statistics*, Nucl. Instrum. Meth. **A434** (1999) 435, [hep-ex/9902006].

[108] U. Langenfeld, S. Moch and P. Uwer, *New results for $t\bar{t}$ Production at Hadron Colliders, in XVLL International Workshop on Deep-Inelastic Scattering and Related Topics Madrid, Spain*, April, 2009.

[109] G. J. Feldman and R. Cousins, *A unified approach to the classical statistical analysis of small signals*, Phys. Rev. **D57** (1998) 3873, [physics/9711021].